NASA CR-72227

FINAL REPORT

MICROWAVE DRIVEN MAGNETIC PLASMA ACCELERATOR STUDIES

(CYCLOPS)

G. F. Crimi, A. C. Eckert, D. B. Miller

prepared for

'ONAL AERONAUTICS AND SPACE ADMINISTRATION

SPACE SCIENCES LABORATORY
GENERAL ELECTRIC
MISSILE AND SPACE DIVISION

NASA CR-72227

FINAL REPORT

MICROWAVE DRIVEN MAGNETIC PLASMA ACCELERATOR STUDIES

(CYCLOPS)

by

G. F. Crimi, A. C. Eckert, D. B. Miller

prepared for

NATIONAL AERONAUTICS AND SPACE ADMINISTRATION

March 24, 1967

CONTRACT NAS 3-8903

Technical Management
NASA Lewis Research Center
Cleveland, Ohio
Spacecraft Technology Division
Dr. H. G. Kosmahl

GENERAL ELECTRIC COMPANY
SPACE SCIENCES LABORATORY
MISSILE AND SPACE DIVISION
P.O. Box 8555
Philadelphia, Pennsylvania 19101

ABSTRACT

A microwave-driven cyclotron resonance plasma acceleration device was investigated using argon, krypton, xenon, and mercury as propellants. Limited ranges of propellant flow rate, input power, and magnetic field strength were used. Over-all efficiencies (including the 65% efficiency of the input polarizer) less than 10% were obtained for specific impulse values between 500 and 1500 sec. Power transfer efficiencies, however, approached 100% of the input power available in the right-hand component of the incident circularly polarized radiation. Beam diagnostics using Langmuir probes, cold gas mapping, r-f mapping and ion energy analyses were performed in conjunction with an engine operating in a pulsed mode. Measurements of transverse electron energies at the position of cyclotron resonant absorption yielded energy values more than an order of magnitude lower than anticipated. The measured electron energies were, however, consistent with the low values of average ion energy measured by retarding potential techniques. The low values of average ion energy were also consistent with the measured thrust values. It is hypothesized that ionization and radiation limit the electron kinetic energy to low-values thus limiting the energy which is finally transferred to the ion. Thermalization by electron-electron collision was also identified as an additional loss mechanism. The use of light alkali metals, which have relatively few low lying energy levels to excite, with the input power to mass ratio selected so as to limit the electron energies to less than the second ionization potential, is suggested. It is concluded, however, that the over-all efficiency for such propellants would be less than 40 per cent.

TABLE OF CONTENTS

Section			Page
ABSTRACT			i
1.	INTRODUCTION		1-1
2.	EXPERIMENTAL EQUIPMENT		2-1
	2.1	C. W. Program	2-1
		2.1.1 Vacuum System	2-1
		2.1.2 R-F System	2-1
		2.1.3 Thrusters	2-1
		2.1.4 Magnet Field Coils	2-7
		2.1.5 Totally Absorbing Mercury Beam Catcher	2-12
		2.1.6 Feed Systems & Flow Meters	2-12
	2.2	Pulsed Program	2-20
		2.2.1 Vacuum System	2-20
		2.2.2 R-F System	2-22
		2.2.3 Magnetic Field	2-22
		2.2.4 Pulsed Gas Valve	2-22
		2.2.5 Thruster	2-26
3.	DIAGNOSTIC INSTRUMENTATION		3-1
	3.1	C. W. Program	3-1
		3.1.1 Ion Energy Analyzer	3-1
		3.1.2 Potential Probe	3-4
		3.1.3 Calorimeter	
		3.1.4 Thrust Stand	
	3.2	Pulsed Program	3-14
		3.2.1 (R, θ, Z) Probe Positioner	3-14
		3.2.2 Data Recording Techniques	3-14
		3.2.3 Gas Pressure Probe	3-14
		3.2.4 R-F Probes	3-16
		3.2.5 Magnetic Probe	3-16
		3.2.6 Langmuir Probes	3-20
		3.2.7 Ion Energy Analyzer Probe	3-20
4.	EXPERIMENTAL RESULTS		4-1
	4.1	C. W. Program	4-1
		4.1.1 Beam Power Measurements	4-1

4.1.2 Thrust Measurements - Ar, Kr, Xe - Internally Mounted Thrust Stand 4-1
4.1.3 Simultaneous Thrust and Ion Energy Measurements 4-9
4.1.4 Thrust Measurements - Ar, Kr - Externally Mounted Thrust Stand 4-13
4.1.5 Potential Measurements 4-19
4.1.6 Thrust Measurements - Mercury 4-19

4.2 Pulsed Program 4-25
4.2.1 R-F Mapping 4-25
4.2.2 Cold Gas Pressure Mapping and Flow Rate 4-34
4.2.3 Electron Energy Profiles 4-41
4.2.4 Ion Energy Analysis 4-45
4.2.5 Measurement of Diamagnetism at Resonance 4-53

5. SUMMARY AND CONCLUSIONS 5-1

6. REFERENCES 6-1

APPENDIXES

A. DETECTION OF THE DIAMAGNETIC EFFECT A-1

B. R-F WAVE PROPAGATION IN CYCLOPS B-1

C. LANGMUIR PROBE IN A MAGNETIC FIELD C-1

D. ION ENERGY ANALYSIS D-1

E. RADIATION E-1

LIST OF FIGURES

Figure Number		Page
2.1.1	Vacuum Facility.	2-2
2.1.2	Vacuum Facility.	2-2
2.1.3	Vacuum System - Schematic.	2-3
2.1.4	R-F System, Microwave Magnetic Accelerator, 8.35 kmc/sec.	2-4
2.1.5	View of R-F System, 8.35 kmc/sec.	2-6
2.1.6	X-Band Longitudinal-Interaction Accelerator; Peripheral Injection; short version (Mark V-S).	2-7
2.1.7	Mark VA-S Engine.	2-8
2.1.8	Exploded View of Mark VA-S Engine.	2-9
2.1.9	The Mark VA-S Engine Assembled and Mounted on Eddy Current Suppressing Port Cover.	2-9
2.1.10	Magnion coil mounted on thrust stand (thrust stand cover removed).	2-10
2.1.11	Magnetic Field Distribution on Axis; Magnion "Plasma Flux" Coil, Type PF3-285-175.	2-11
2.1.12	New Coil.	2-13
2.1.13	On Axis Field Plot of New 5 Inch I. D. Coil.	2-14
2.1.14	Can Outline Assembly - Mercury Beam Catcher.	2-15
2.1.15	Honey Comb Assembly - Mercury Beam Catcher.	2-16
2.1.16	Assembled Mercury Beam Catcher.	2-17
2.1.17	Mercury Feed System.	2-18
2.1.18	Mercury Feed System.	2-18
2.1.19	Mercury Feed System - Overall view.	2-19

2.1.20	Mercury Feed System.	2-19
2.2.1	Vacuum Facility for Pulsed Program - Back View.	2-21
2.2.2	Vacuum Facility for Pulsed Program - Front View.	2-21
2.2.3	R-F System Schematic, Pulsed Program, 8.35 kmc/sec.	2-23
2.2.4	R-F System, Pulsed Program, 8.35 kmc/sec.	2-24
2.2.5	Shielded Pulsed Gas Valve in Position.	2-24
2.2.6	Pulsed Valve for Propellant Feed.	2-25
2.2.7	Pulsed X-Band Longitudinal-Interaction Accelerator; Peripheral Injection (Mark IX-L).	2-27
3.1.1	Ion Energy Analysing Probe.	3-2
3.1.2	Retarded Potential Probe Circuit.	3-2
3.1.3	Typical Scope trace recording showing I-V trace and Langmuir probe trace.	3-3
3.1.4	Langmuir Probe Biasing Circuit.	3-3
3.1.5	Emitting Probe structure Details.	3-5
3.1.6	Emitting Probe Circuit.	3-6
3.1.7	10" Diameter by 20" Long Steady State Calorimeter, Mounted on Support Shaft.	3-7
3.1.8	Thrust Stand Assembly Drawing.	3-9
3.1.9	Thrust Stand, Side and Face Views.	3-10
3.1.10	Thrust Stand with Cover Removed.	3-11
3.1.11	Thrust Stand with Waveguide Attached.	3-11
3.1.12	Externally mounted thrust stand with coil suspended on thrust stand and engine mounted on port cover.	3-13
3.2.1	Probe carriage, gas pressure probe installed.	3-15

3.2.2	Probe carriage, gas pressure probe end view.	3-15
3.2.3	Circuit for the Gas Pressure Probe.	3-17
3.2.4	Movable R-F Probes.	3-18
3.2.5	Probe for Detection of Diamagnetic Effect.	3-19
3.2.6	Transverse Probe for $Te_{//}$.	3-21
3.2.7	Longitudinal Probe for $Te_{\perp}$.	3-21
3.2.8	Langmuir Probe Voltage Sweep Circuit.	3-22
3.2.9	Synchronizations for Langmuir Probe Data and Resultant Trace.	3-22
3.2.10	Ion Energy Analysing Probe.	3-23
3.2.11	Retarding Potential (Ion Energy) Probe Circuit.	3-23
3.2.12	Instrumentation for Ion Energy Analysis	3-25
4.1.1	Mark V-S Accelerator Mounted on Thrust Stand in Vacuum Tank.	4-2
4.1.2	Calorimeter Temperature Record.	4-4
4.1.3	Typical Thrust Measurement Data Record, Mark V-S Accelerator.	4-5
4.1.4	Thrust-Mass Flow Plot, Mark V-S Thruster, Argon.	4-6
4.1.5	Thrust Mass Flow Plot from Thrust Data; Mark V-S Thruster, Krypton.	4-7
4.1.6	Thrust Mass Flow Plot from Thrust Data; Mark V-S Thruster, Xenon.	4-8
4.1.7	I-V Curve Obtained from Trace of Figure 3.1.3.	4-11
4.1.8	Energy Distribution Function Obtained by Differentiating the I-V Curve of Figure 3.1.3.	4-12
4.1.9	Comparison of Thrust Determined and Retarding Potential Determined Values of Specific Impulse.	4-15

4.1.10	Thrust Mass Flow Plot, Mark VA-S Thruster, Argon.	4-17
4.1.11	Thrust Mass Flow Plot, Mark VA-S Thruster, Krypton.	4-18
4.1.12	Axial Plasma Potential vs. Distance from Window, Imag = 250 amp, $\dot{m}$ = 0.7 mg/sec Argon.	4-20
4.1.13	Axial Plasma Potential vs. Distance from Window, Imag = 210 amp, $\dot{m}$ = 0.7 mg/sec Argon.	4-21
4.1.14	Axial Plasma Potential vs. Distance from Window, Imag = 210 amp, $\dot{m}$ = 0.53 mg/sec, argon.	4-22
4.1.15	Thrust vs. mass flow, Mercury.	4-23
4.1.16	Total efficiency vs. mass flow, Mercury.	4-24
4.2.1	Typical X-Y Plot.	4-26
4.2.2	Diagrammed Probe Traversals of the Engine.	4-26
4.2.3	Radial Component of the Electric Field in the Engine.	4-28
4.2.4	Output of Circular Polarizer Preceding Engine.	4-29
4.2.5	Low Flow R-F Field Mapping.	4-30/31
4.2.6	Axial Position of Resonant Field Strength (cm) vs. Radius From Coil Center (cm).	4-33
4.2.7	Upper Trace - Valve Triggering Pulse, 500 volts/cm. Lower Trace - Pressure profile, 50 mv/cm - sweep 5 msec/cm.	4-35
4.2.8	Upper Trace - Valve Triggering Pulse, 500 volts/cm. Lower Trace - Pressure Profile on Engine Exit Plane X-Axis Radial Position, .38 cm/cm.	4-35
4.2.9	Pressure and Density vs. Axial Position Normalized to: 9.3 microns Hg and 2.01×10^{-8} gm/cm^3 or 3.04×10^{14} particles/cm^3.	4-36
4.2.10	Pressure vs. Time Profile.	4-38
4.2.11	Pressure vs. Time Profile.	4-39

4.2.12	Pressure vs. Time Profile.	4-40
4.2.13	Mass Flow Rate (μg/millisec) vs. Pressure - mm Hg.	4-42
4.2.14	Summary Mapping of on Axis Langmuir Probe and R-F Results.	4-44
4.2.15	Langmuir Probe Trace for Data Set for $Te_{//}$.	4-46
4.2.16	The Ideal Cylindrical Langmuir Probe Trace.	4-46
4.2.17	Front Edge Synchronization.	4-49
4.2.18	6 Millisecond Synchronization.	4-49
4.2.19	I-V Trace for Front Edge Synchronization.	4-50
4.2.20	I-V Trace for 6 millisecond Synchronization.	4-50
4.2.21	Thrust vs. input r-f power.	4-52

ACKNOWLEDGMENT

The authors wish to acknowledge the contributions to this work by Dr. C. S. Cook in the design and use of probes and Mr. A. D. Ruess in the assembly and testing of the vacuum facility and the pulsed gas valve and engine for the Pulsed Program.

1. INTRODUCTION

This report covers the work performed during the period from February 28, 1966 to February 27, 1967 under NASA Contract NAS 3-8903 which is the most recent phase of a NASA sponsored program (earlier Contract Nos. NAS 5-1046, NAS 3-3567, NAS 3-6266) to develop a microwave driven electron-cyclotron resonance plasma accelerator for space propulsion applications.

Previous to this program the measured accelerator characteristics were:

1. Power transfer efficiencies using argon, krypton and xenon, up to the limiting value imposed by the circular polarizer characteristics in the microwave system.

2. Over-all efficiencies based on the input mass flow rate and thrust measurements using argon and xenon which varied from 6% up to 46% with 60% of the reported efficiency values falling between 6 and 16 per cent and the remaining values falling between 28 and 46 per cent. The corresponding range of specific impulse based on measured thrust and input mass flow runs from 600 to 6800 seconds.

3. Operating time limited because of inadequate engine cooling; i.e., from 2 to 10 minutes operation depending on the power level.

The general objectives of this program were the following:

1. To study the mechanisms involved in the coupling of microwaves to plasmas in inhomogeneous, static magnetic fields which are necessary for the improvement and better understanding of this accelerator as a space thruster as well as to study processes incidental to the device which are of importance to the general field of r-f plasma confinement and diffusion across magnetic fields and to the propagation of microwaves through plasmas.

2. To further improve the actual performance of the experimental accelerator developed under the previous contract.

3. To obtain over-all efficiencies ($\eta = T^2/2\dot{m}P$) of 50% or more in order to demonstrate the potential of the device as a space thruster.

In order to most effectively meet the general objectives described above, two experimental programs were established. One was designated the C.W. Program. It was in this program that the device was evaluated as a space thruster by measuring the developed thrust for different input

powers, input propellant feed rates, and magnetic field strengths. In addition, measurements of beam potential distribution and final ion energy were made. The C. W. Program was conducted in a 4 ft. diameter, 6 ft. long stainless steel vacuum chamber with a total pumping capacity of 9000 liters/sec. The thruster was driven by an r-f system capable of generating 5000 watts of power at 8. 35 gc.

The second program, designated the Pulsed Program, was established in order to allow operation at lower background pressure and lower average power density than was possible in the C. W. Program. Beam diagnostics near and inside the engine were therefore possible. In addition by adjusting the relative timing of the r-f pulse and the gas pulse the effects of entrainment were observed. Essential to the Pulsed Program was a valve which pulsed the propellant input. This permitted maintaining a low time average propellant flow rate while approximating the value occurring for cw operation during the pulse. Spatial distribution measurements of neutral gas, r-f power, electron number density and transverse and parallel electron energy were made in and near the engine. Ion energy analyses using the retarding potential technique were made at a distance of one meter from the engine. The experimentation was conducted in a 1. 5 ft. diameter by 3. 5 ft. long vacuum chamber connected to a 10 in. diameter diffusion pump. The power source for this system was capable of delivering 5000 watts of r-f power at 8. 35 gc at various pulse widths.

The results of this program infer that poor engine performance should be expected for propellants having many low lying levels for excitation and ionization such as argon, krypton, xenon, and mercury, since multiple ionization and excitation limit the energy to which the electrons may be driven. Measurement of high power transfer efficiencies have been repeated and explained in terms of recovery of excitation energy and recombination. The earlier low over-all efficiencies based on thrust measurements using inert gases have been corroborated for operation when no outgassing effects had occurred. Low over-all efficiencies were also obtained using mercury. For mercury operation neither outgassing or entrainment effects were believed to be present.

The goal for the attainment of 50% over-all efficiency was not realized for the propellants used in this program. However, it is concluded that, by using light-weight alkali metals at relatively low power input, 40% over-all efficiency may be approached. This conclusion is found to be in agreement with the results of others[20].

2. EXPERIMENTAL EQUIPMENT

2.1 C. W. PROGRAM

2.1.1 Vacuum System

The experimental work for this contract was carried out in a test facility financed by General Electric facility funds. This facility, shown in Figures 2.1.1, 2.1.2 and 2.1.3 has the following specifications:

vacuum tank: 4' diameter, 6' long, full-sized hinged doors each end stainless steel.

pumping system: (2) oil diffusion pumps, each rated at 18,000 liters per second; estimated total pumping capacity (taking into account flow resistance due to right angle valves and baffles) is 9000 liters per second (20,000 liters per second without the baffles).

ultimate attained pressure: 1.6×10^{-7} mm Hg (without liquid nitrogen in baffles).

2.1.2 R-F System

The r-f system used to generate the microwave power is shown in Figure 2.1.4. Note that the input r-f power to the accelerator was continuously monitored by a calorimetric power meter. To effect calibration of the system the engine was replaced by a calibrated water load/calorimeter (Varian, Model V-4045F, Ser. #19), and the two absolute power meters were compared up to 5 kw. Using the measured value for the DBH631 30 db directional coupler (29.6 db at 8.35 gc), the HP434A calorimetric power meter was found to read accurately within 5% up to 5000 watts. The polarizer was a special unit built by DeMornay-Bonardi Company, designed for 8.35 gc. The radiation pattern was measured to have an ellipticity of approximately 4:1, thus, approximately 65% of the input power is carried by the right hand circularly polarized component of the output wave. A photographic view of the overall system is shown in Figure 2.1.5.

2.1.3 Thrusters

Continuing the accelerator designation begun for X-band accelerators during previous contracts, the engine design referred to as the Mark V-S design was used during this report period. This engine, shown in Figure 2.1.6 has an ionization chamber 1.152 inches in diameter by 1.00 inches long. Other features of the design are the beryllium oxide half-wave window

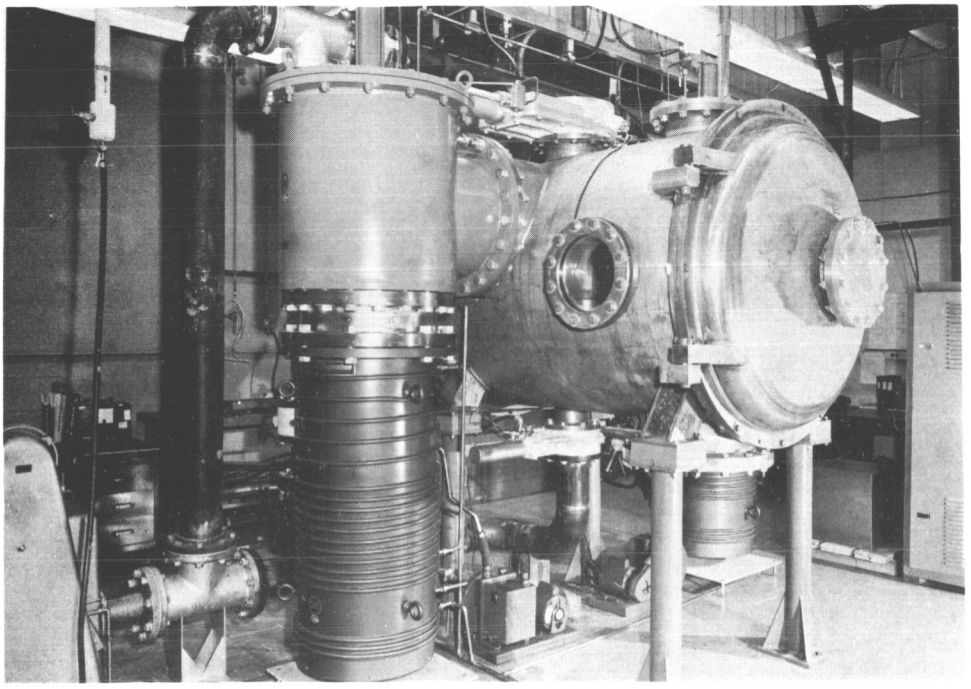

Figure 2.1.1 Vacuum Facility

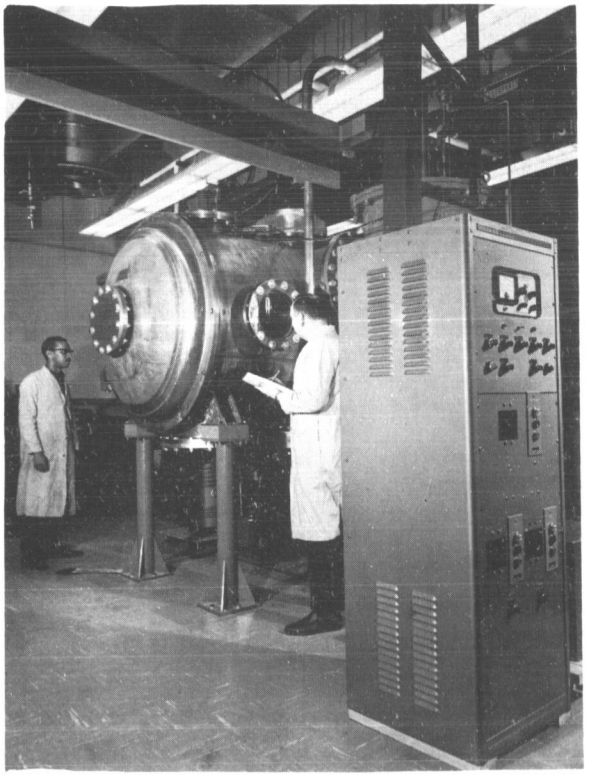

Figure 2.1.2 Vacuum Facility

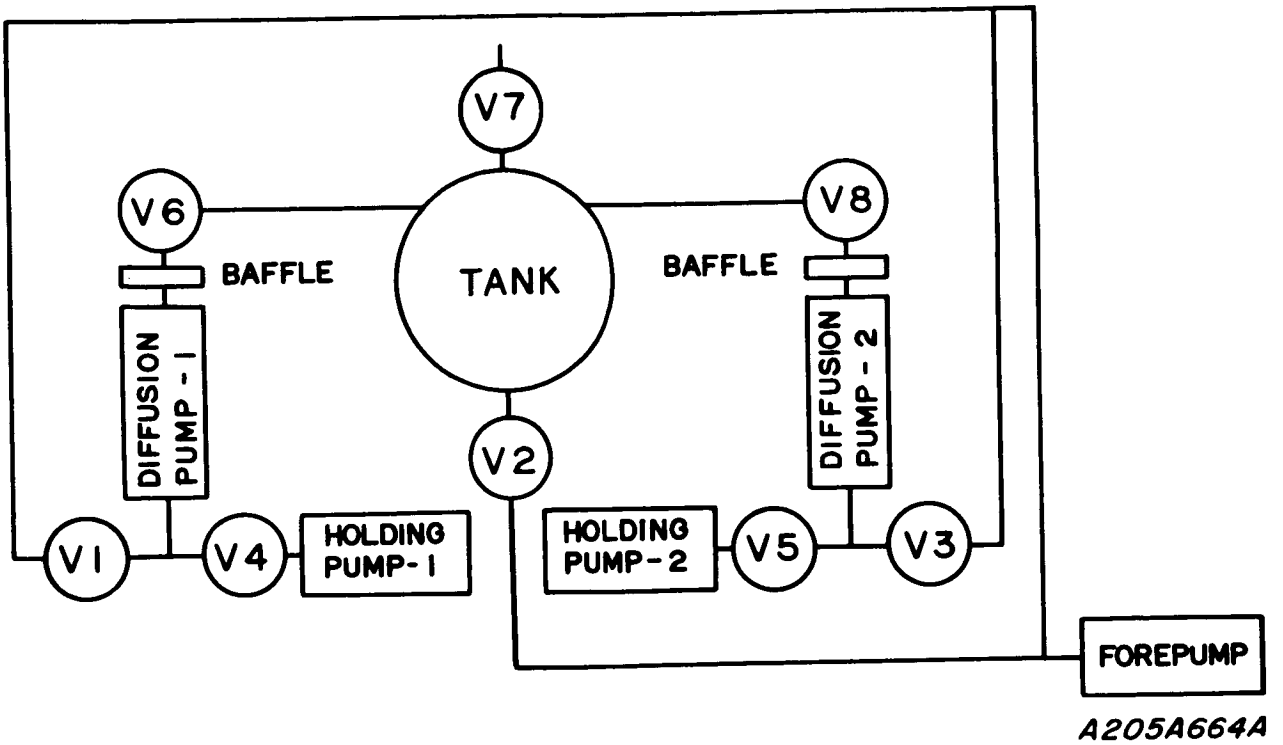

Tank: 4' Dia x 6' Long

Baffles: CVC BC210

Pumps:

Diffusion: CVC PMC 18000
Fore: Stokes 212H
Holding: Welch 1403B

Valves:

V1, V2, V3: 6" Gate, CVC VST 63M2
V4, V5: 2" Gate, CVC VST 23M2
V6, V8: 20" Rt. Angle, CVC VRA 216
V7: 10" Gate, CVC VST 103M2

Figure 2.1.3 Vacuum System - Schematic

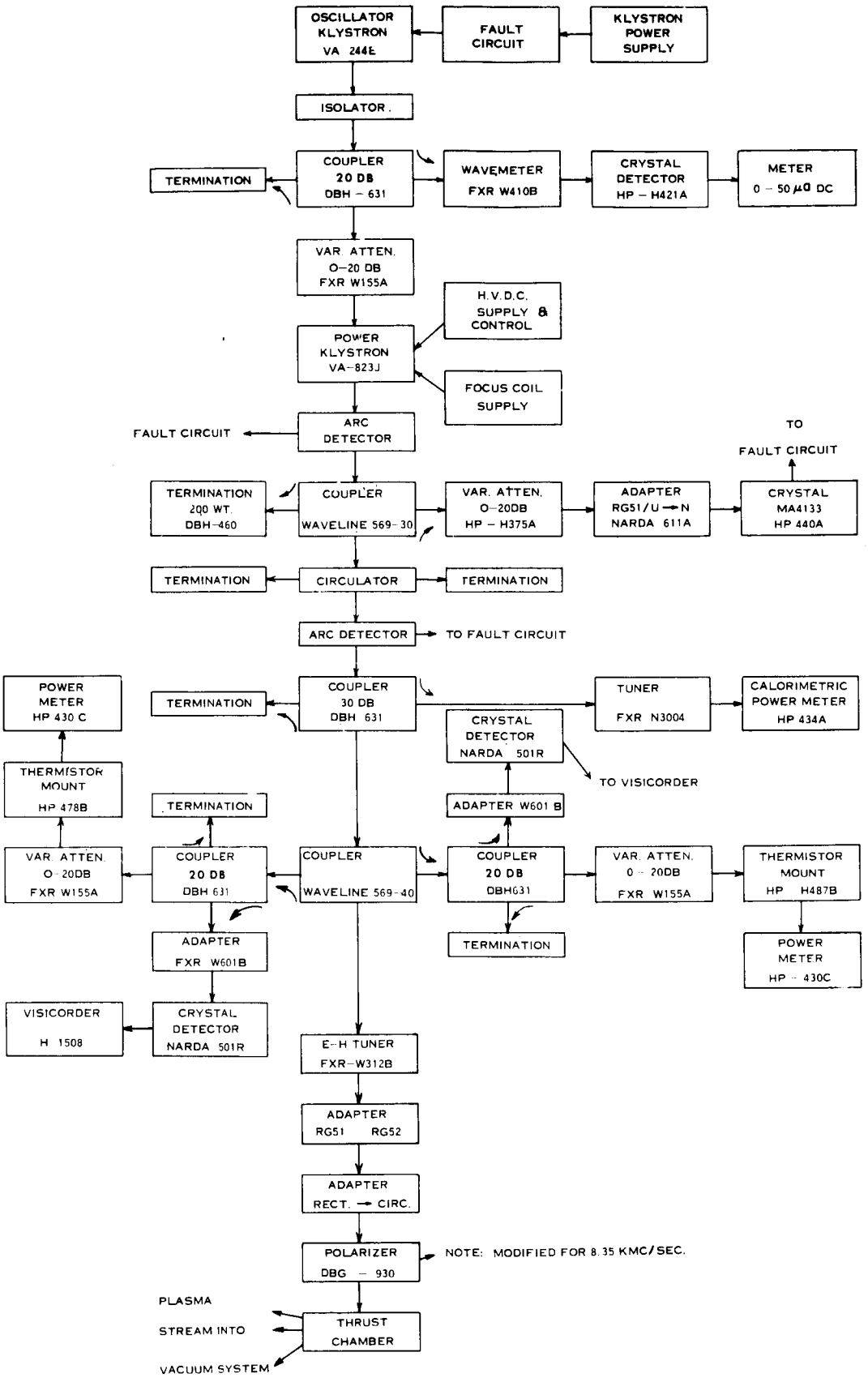

Figure 2.1.4 R-f System, Microwave Magnetic Accelerator, 8.35 kmc/sec.

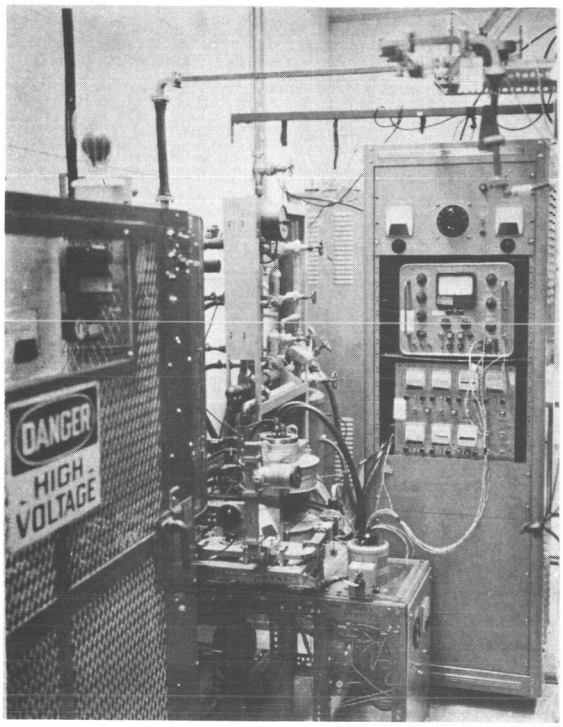

Figure 2.1.5 View of R-F System, 8.35 Kmc/sec.

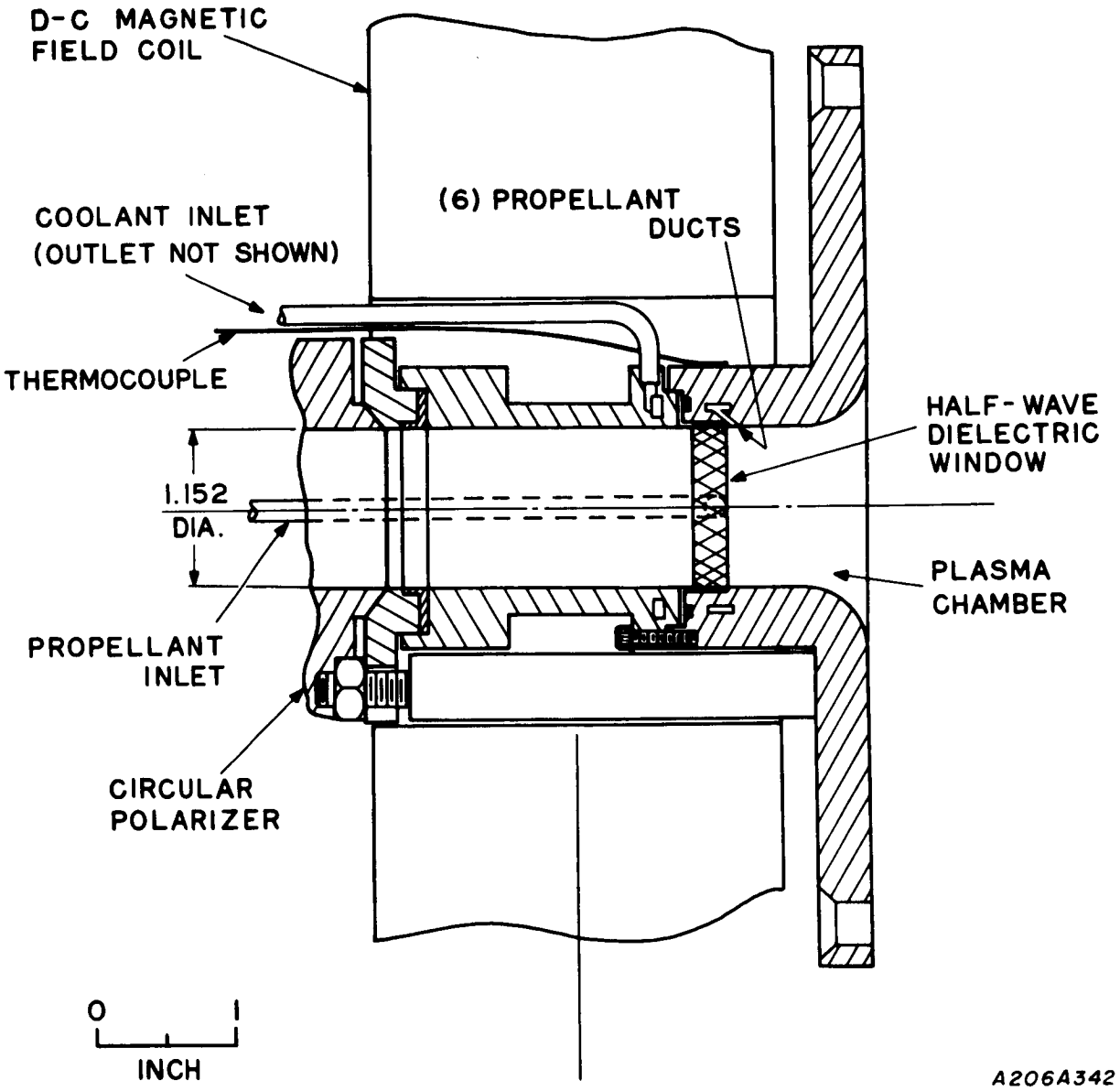

Figure 2.1.6 X-Band Longitudinal-Interaction Accelerator; Peripheral Injection; short version (Mark V-S)

and the peripheral gas injection through ducts which are cut at a slant angle to the axial direction in order to impart a component of axial velocity to the gas.

The engine was cooled by flowing water through a ring-shaped duct adjacent to the window flange. The flow rate was approximately 15 cc/sec, corresponding to 63 watt/c^{o}. The fact that, after running, the engine cooled much more rapidly with the water flowing then with the water turned off indicates that the water flow is the major means by which heat was taken from the accelerator. The ability of the dielectric windows to remain intact was apparently quite sensitive to accelerator temperature, since most beryllium oxide window failures can be traced to situations in which the accelerator temperature was allowed to reach levels near 200^{o}C. During testing of this engine, 125^{o}C was adopted as the maximum allowable temperature. This temperature limit imposed a limitation on the operating time, especially when the input power was above 1000 watts. At 2000 watts, the engine on-time was typically 5 minutes depending on the mass flow rate and magnetic field. In order to increase the allowable operating time, a new engine designated the Mark VA-S was designed and fabricated. This engine was the same as the Mark V-S except that the cooling capacity was increased by providing water cooling to the ionization chamber wall in addition to the existing water cooling loop near the mounting flange of the dielectric window. The Mark VA-S engine, shown in Figure 2.1.7 was designed for noble gas operation and for compatibility with the structures necessary for measuring thrust. The thrust balance was mounted either internal or external to the vacuum chamber. Figure 2.1.8 shows a photograph of the disassembled Mark VA-S engine. Figure 2.1.9 shows the engine mounted to a non-magnetic stainless steel port cover containing slots for eddy current suppression. Also shown in Figure 2.1.9 is the nylon ring necessary for making an electrically insulated vacuum seal.

For mercury operation, the mainfold section of Figure 2.1.8 was modified to provide six gas inlets of 3/16 in. I.D., each fed by six vapor inlet lines. This increased cross-sectional area was necessary in order to prevent condensation at the engine temperature of nominally 100^{o}C.

2.1.4 Magnet Field Coils

The Mark V-S engine was operated in conjunction with a Magnion "plasma flux" coil, type PF 3-285-175, for providing the necessary magnetic field. A three-phase bridge rectifier circuit had been built to supply the current for this coil (290 amp at 88 volts). A photograph of the Magnion coil mounted on the thrust stand and located inside the vacuum chamber is shown in Figure 2.1.10. The on-axis magnetic field distribution produced by the coil is shown in Figure 2.1.11.

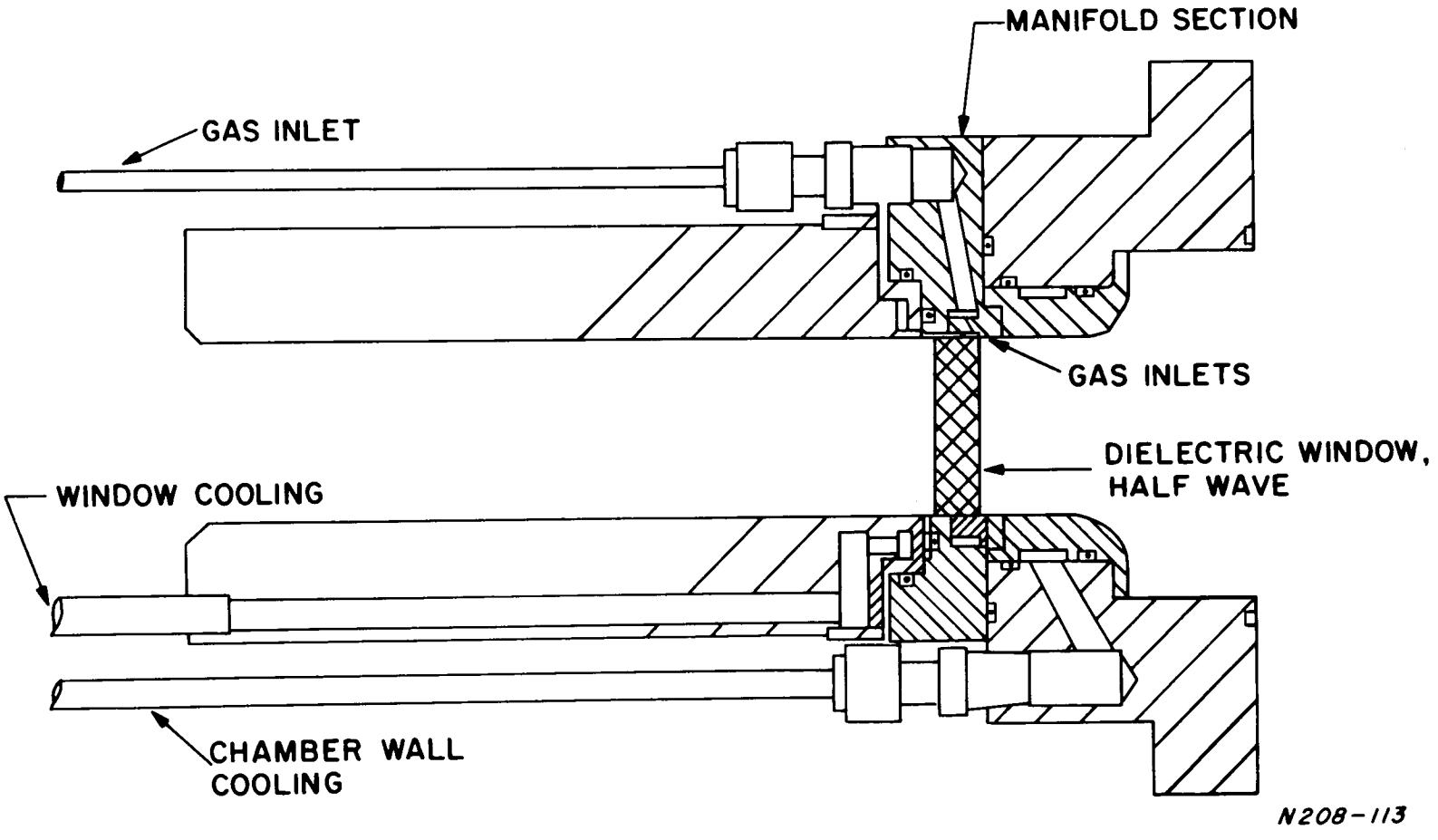

Figure 2.1.7 Mark VA-S Engine.

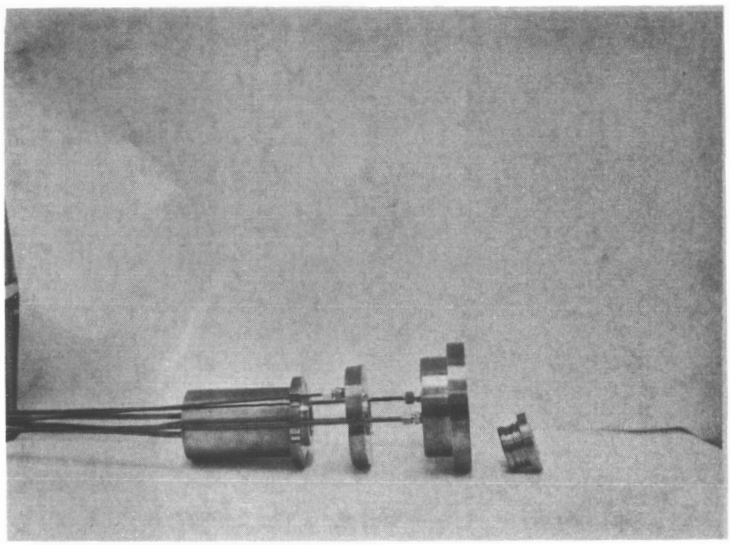

Figure 2.1.8 Exploded View of Mark VA-S Engine.

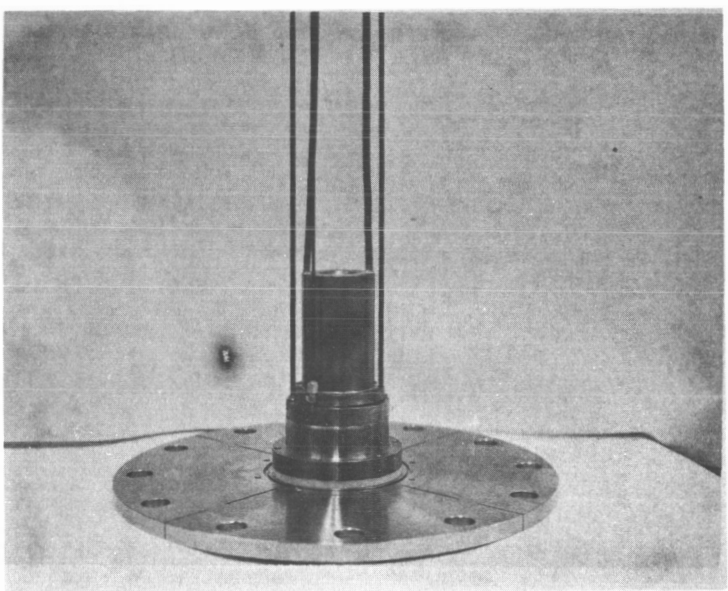

Figure 2.1.9 The Mark VA-S Engine Assembled and Mounted on Eddy Current Suppressing Port Cover.

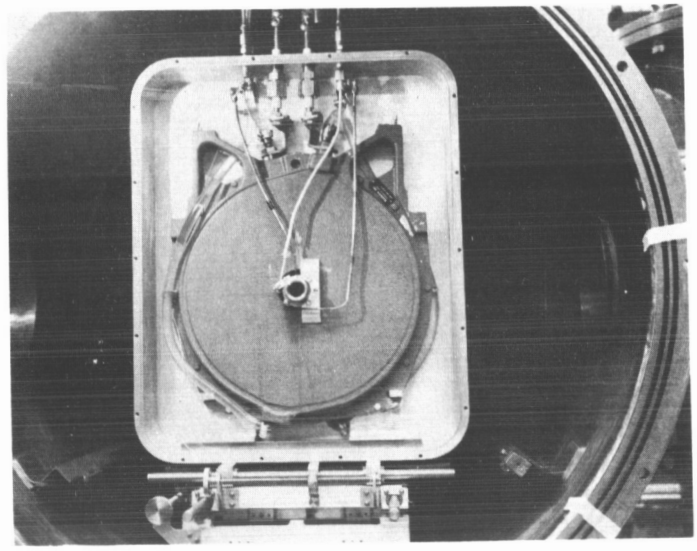

Figure 2.1.10 Magnion coil mounted on thrust stand (thrust stand cover removed).

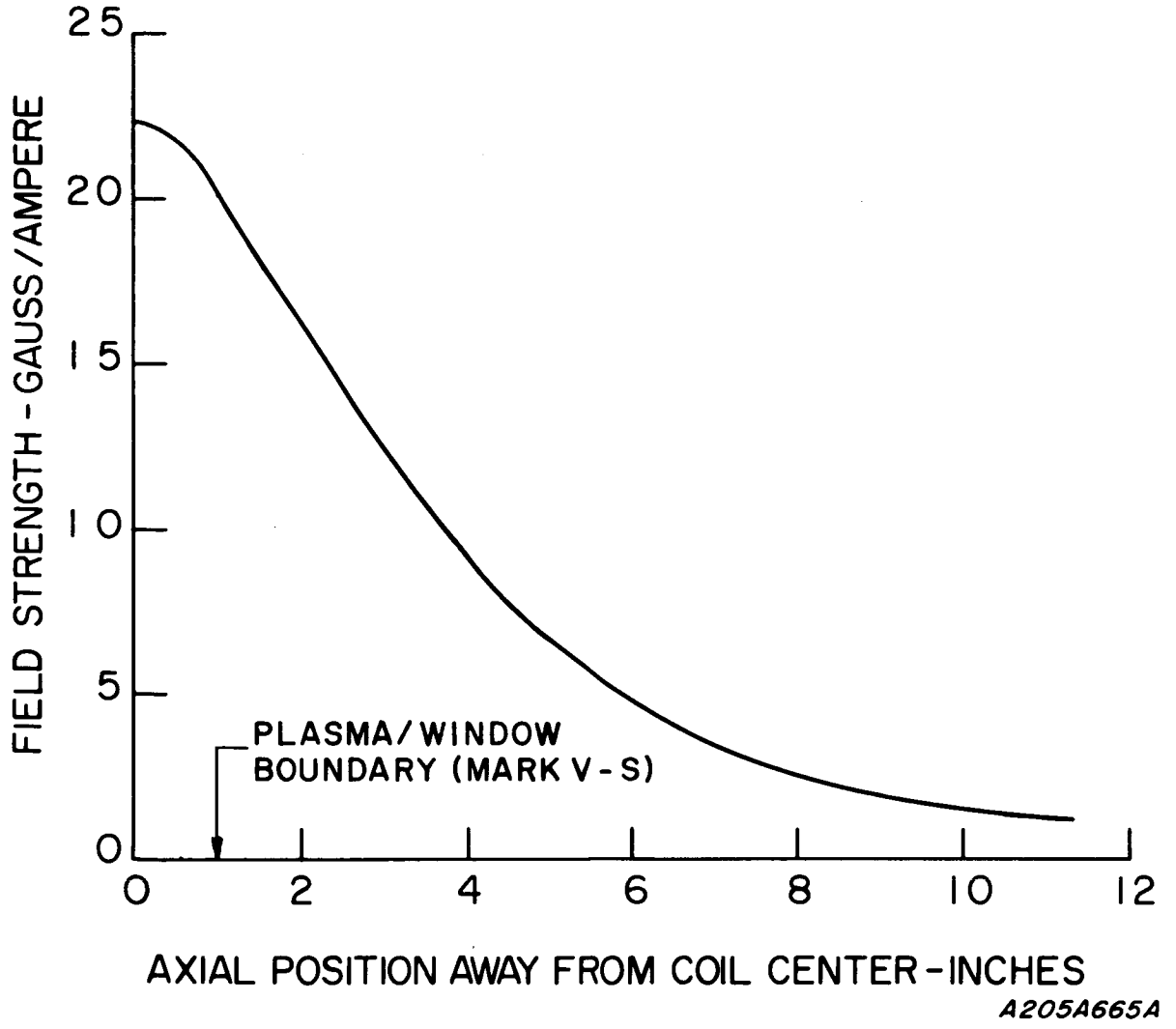

Figure 2.1.11 Magnetic Field Distribution on Axis; Magnion "Plasma Flux" Coil, Type PF3-285-175.

In order to accommodate the larger size of the Mark VA-S engine, a coil of larger I. D. was designed and fabricated by General Electric. This coil required modification of the power supply capability to 600 amps, 38 volts. A photograph of the 5 inch I. D. coil mounted on the thrust stand external to the vacuum chamber is shown in Figure 2. 1. 12. The Mark VA-S engine mounted on the vacuum chamber port is also visible in the figure. Figure 2. 1. 13 shows the on-axis field plot associated with the coil.

2. 1. 5 Totally Absorbing Mercury Beam Catcher

A totally absorbing mercury beam catcher was designed and fabricated. The details of the outer can are shown in Figure 2. 1. 14 while Figure 2. 1. 15 shows the details of mounting the cooled honeycomb structure inside the can. The honeycomb material is aluminum with a 1/8 in. cell size, and 6 inches deep. All other components are made from a 300 series stainless steel. Thermal contact between the honeycomb and the concentric cylinders was accomplished by using a copper powder-filled silicon grease which was found to be satisfactory at liquid nitrogen temperatures. A photograph of the assembled beam catcher is shown in Figure 2. 1. 16. The system was designed to be cooled by liquid nitrogen.

2. 1. 6 Feed Systems & Flow Meters

A mercury feed system was fabricated. The design was based on the positive displacement of liquid mercury out of a precision bore glass tube using a mechanical drive of continuously variable speed. The liquid mercury was displaced into a 1/8 inch stainless steel tubing which contained a vaporizer at the engine end. The vaporizer was simply a continuation of the 1/8 inch diameter tubing located between a cooling block and a heating block. The blocks established a temperature gradient along the tube between the two blocks. The liquid-vapor interface was maintained at the position in the vaporizer where the temperature was such that the evaporization rate was equal to the displacement rate from the precision bore glass tubing. The vapor was then conducted to the engine through heated tubing. Figures 2. 1. 17 through 2. 1. 20 show several views of the mercury feed system.

For flow rate measurement of the noble gas propellants several meters based on different physical principles were used. Early measurements were made using a Brooks Instrument Co. rotameter, type 1A-15-1, equipped with a glass tube and stainless steel and aluminum floats. The initial calibration of the rotameter was performed in a cursory manner by inserting it in series with the bleed line from a reservoir of known volume. By observing the time rate of change of the pressure, the flow rate could be calculated and compared with the observed rotameter reading. Satisfactory agreement was initially obtained.

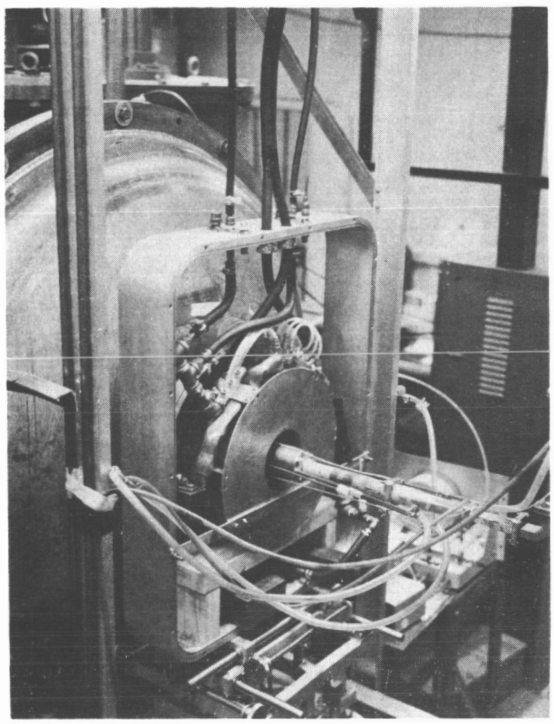

Figure 2.1.12 New Coil.

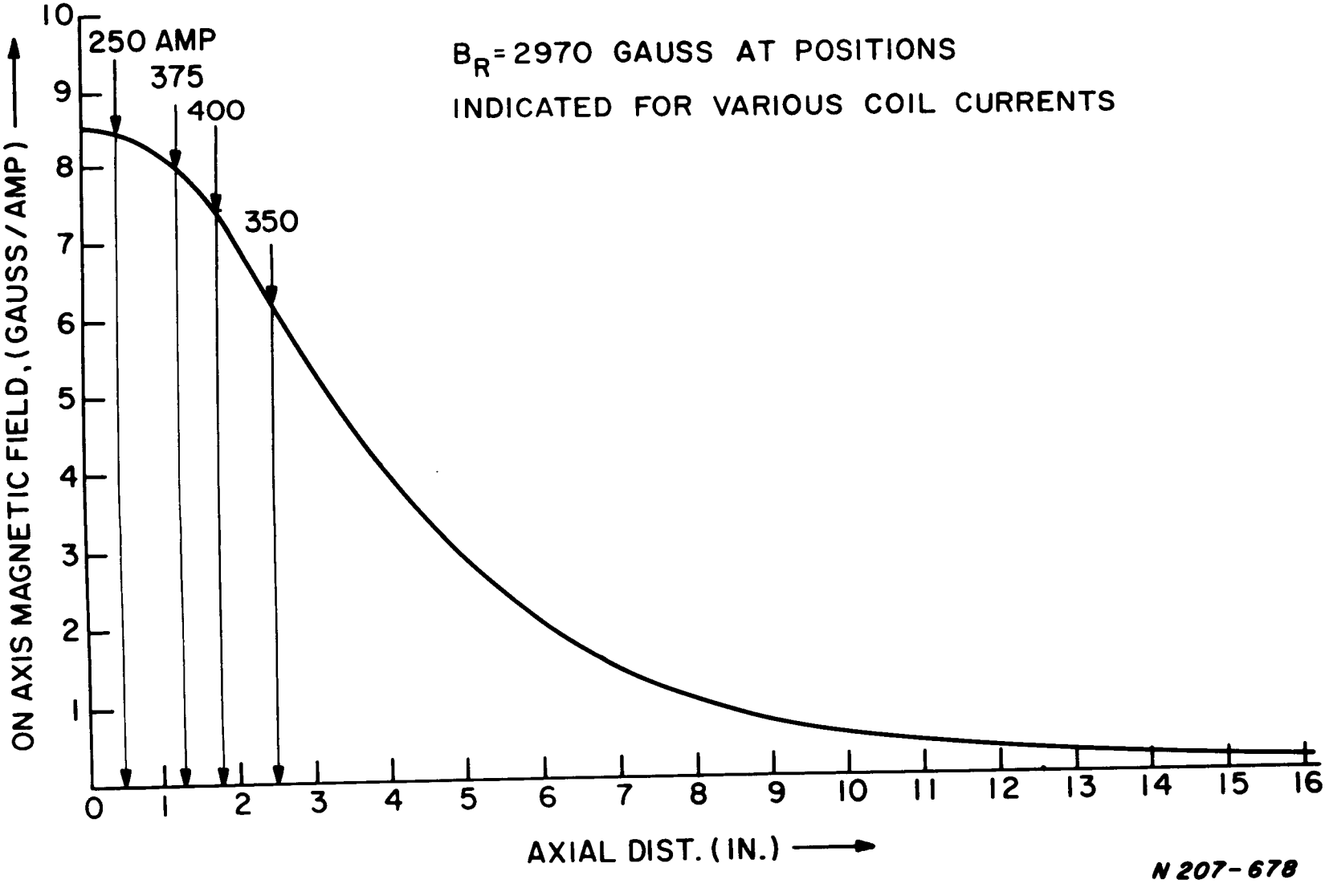

Figure 2.1.13 On Axis Field Plot of New 5 inch I. D. Coil.

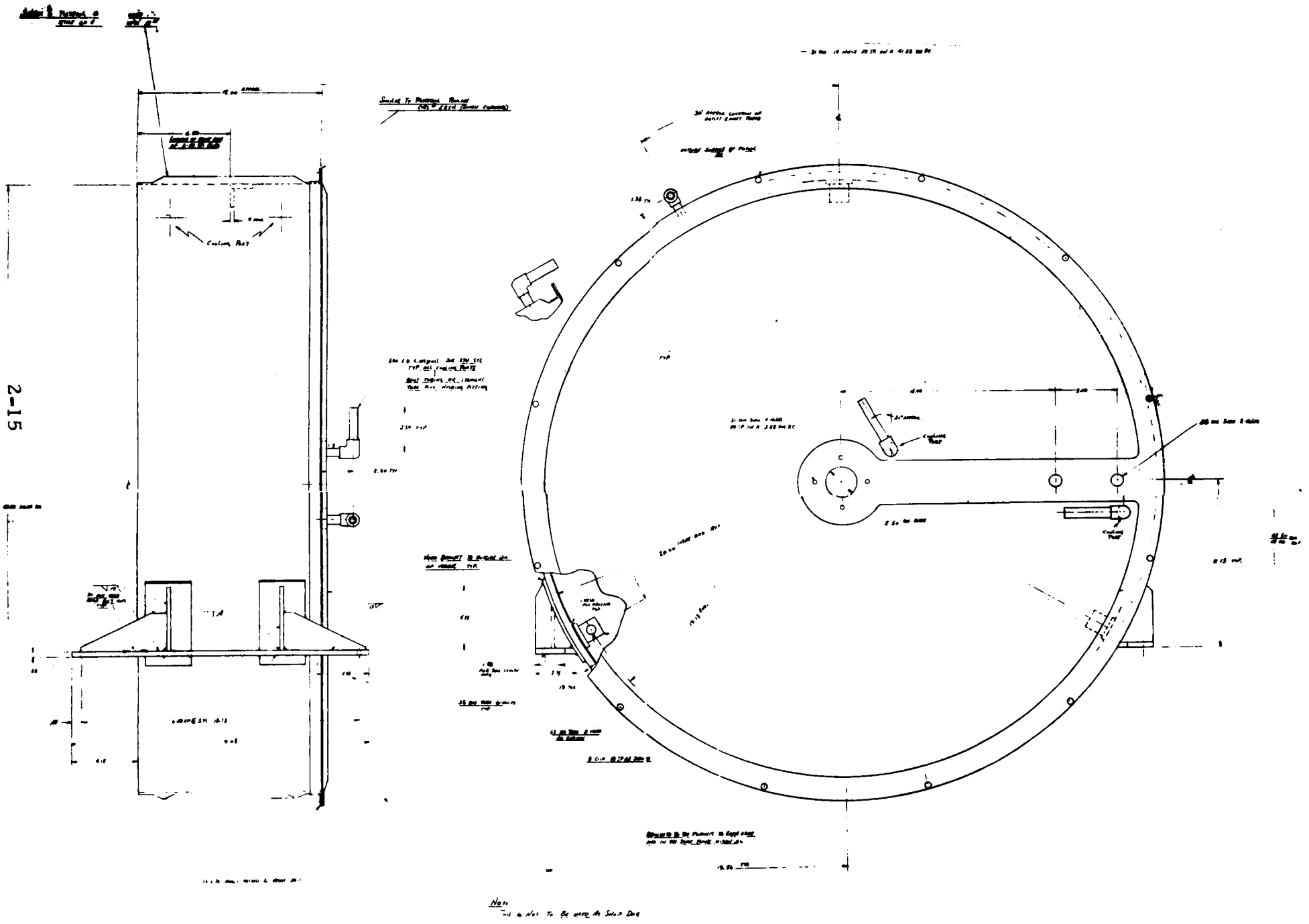

Figure 2.1.14 Can Outline Assembly - Mercury Beam Catcher

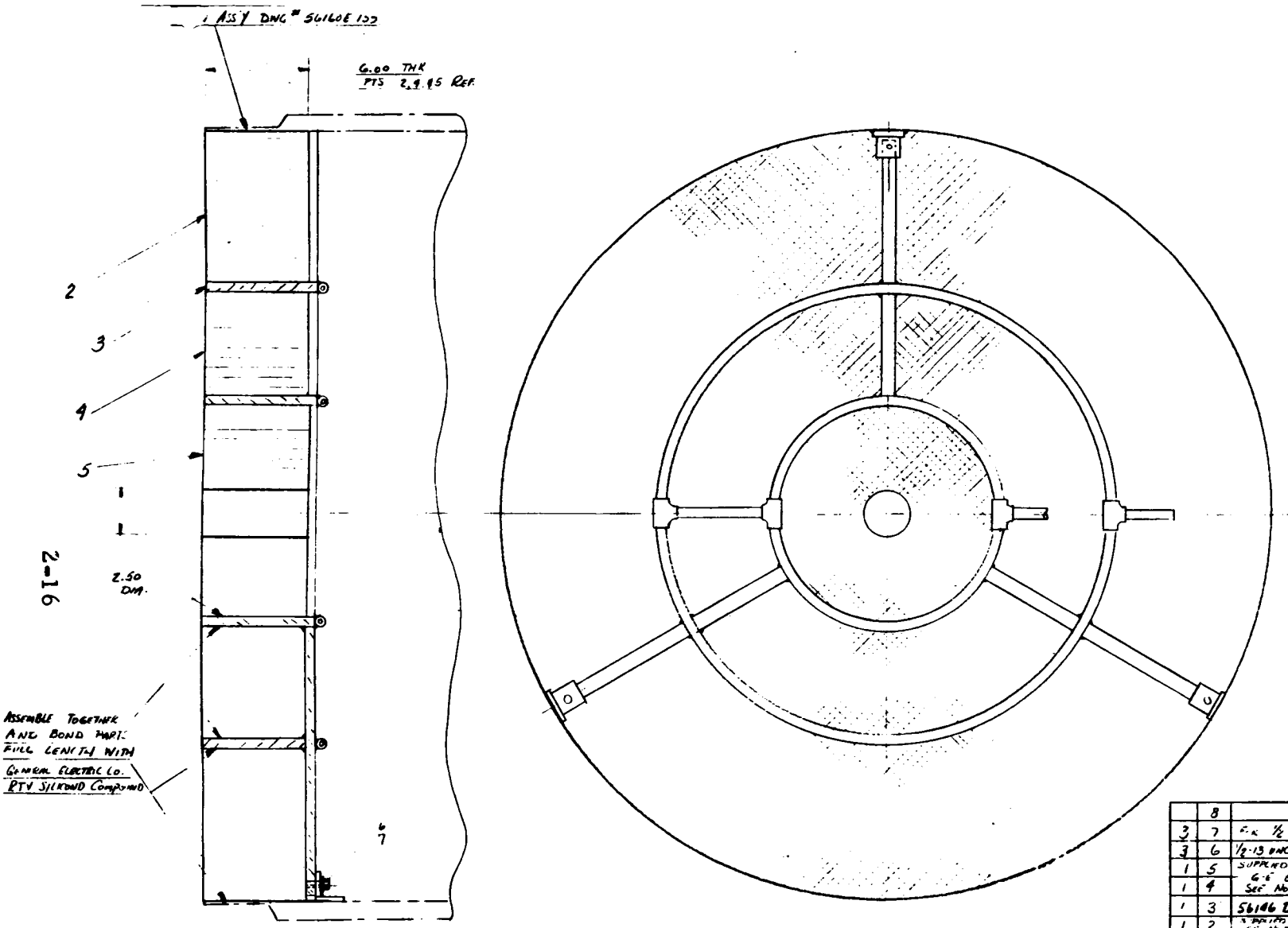

2-16

	8		
3	7	¼ SLR.	WASHER - PLAIN (NOM. MAT'L SAME AS ITEM 6)
3	6	½-13 UNC-2 X .63 LG.	SCREW SOC HD CAP
1	5	SUPPLIED BY G.E. ENGR. SEE NOTE 1	HONEY COMB (INNER)
1	4		HONEY COMB (INTERMEDIATE)
1	3	56L46 D154 G1	OUTER SHELL
1	2	SUPPLIED BY G.E. ENGR. SEE NOTE 1	HONEY COMB (OUTER)
X	1		ASSEMBLY
1	ITEM	IDENTIFYING DRAWING NO.	NAME OR DESC.

NOTE

1- OUTSIDE & INSIDE DIA'S OF PTS 2,4,5 TO BE CUT WITH SNUG FIT TO MATING DIA'S

(1)

UNLESS OTHERWISE SPECIFIED DIMENSIONS ARE IN INCHES— TOLERANCES ON:		SIGNATURES	DAY	MO	YR
2-PLACE DECIMALS ± .01	ALL SURF	DRAWN L. Letts	1	9	66
3-PLACE DECIMALS ±		CHECKED			
ANGLES ±		ISSUED			
FRACTIONS ±	✓	ENGR'G			
MATERIAL— NOTED		MFG			
		MATL'S			

GENERAL ELECTRIC
NSD-SSL DEPT LOC VALLEY FORGE PA

HONEY COMB ASSEMBLY
MERCURY BEAM CATCHER

SIZE	CODE IDENT NO.	
C		56160C156
SCALE HALF		SHEET

Figure 2.1.15 Honey Comb Assembly - Mercury Beam Catcher

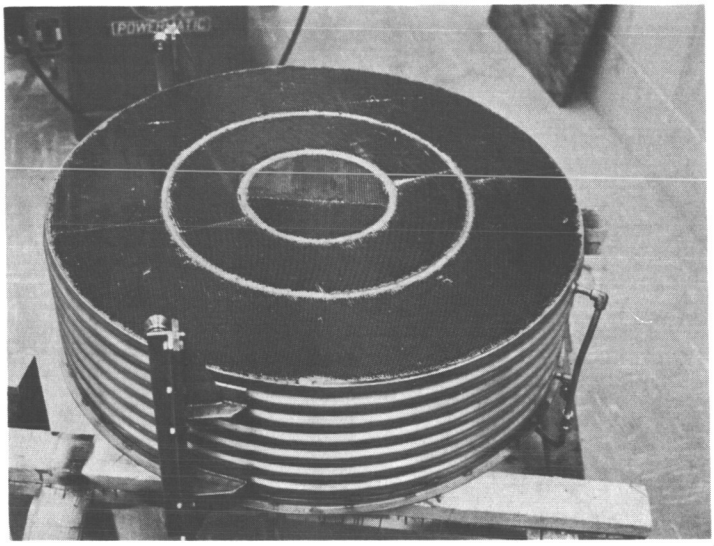

Figure 2.1.16 Assembled mercury beam catcher.

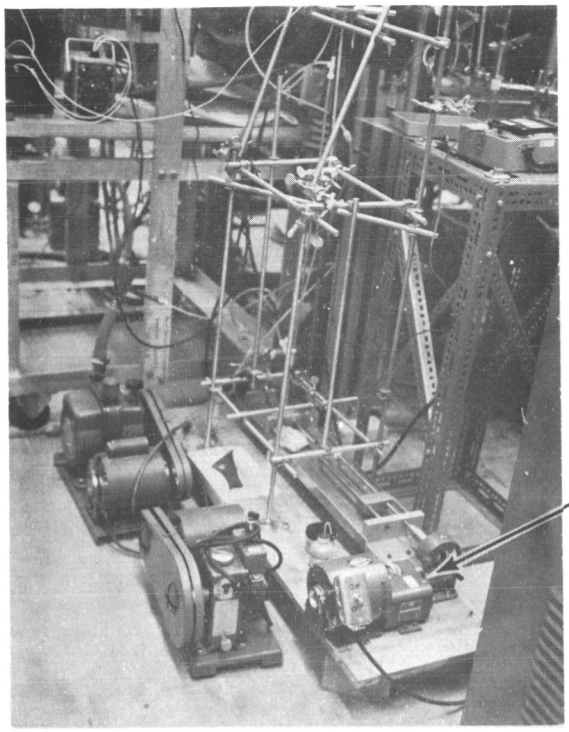

Figure 2.1.17 Mercury Feed System

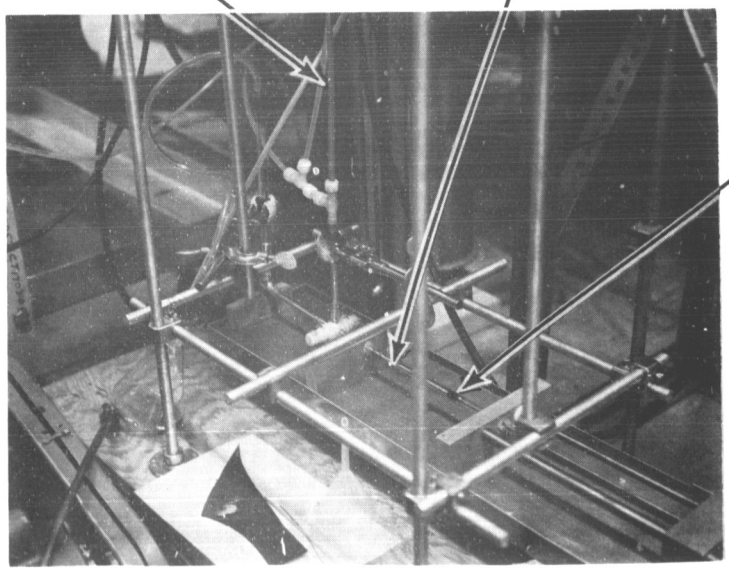

Figure 2.1.18 Mercury Feed System.

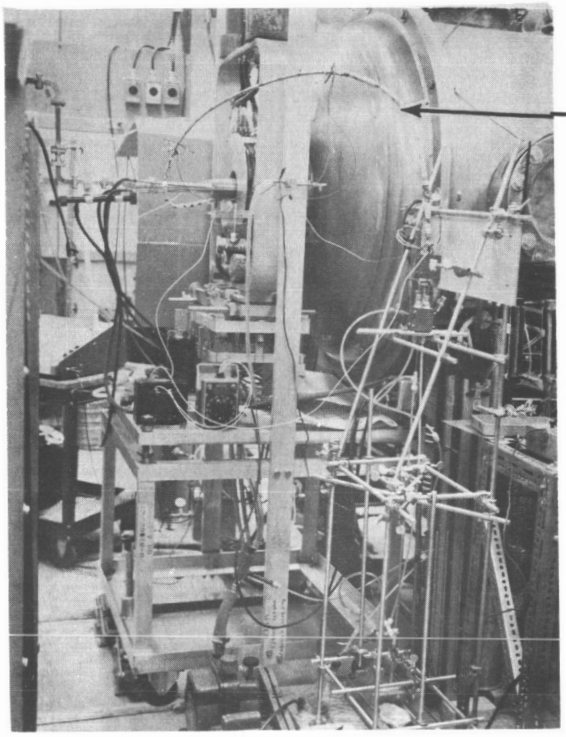

Figure 2.1.19 Mercury Feed System - Overall view.

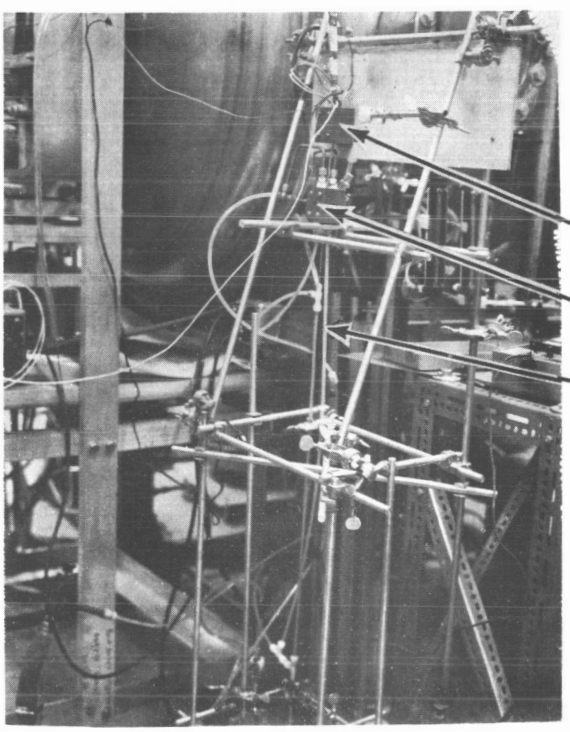

Figure 2.1.20 Mercury Feed System.

During later engine testing, it became evident that the accuracy and the calibration constancy of the rotameter were questionable. Several different types of flow meters were therefore investigated by connecting all of them in series in the bleed line from a cylinder of known volume. The results of this investigation were the following:

Rotameters: Brooks Type 1A-15-1, Matheson No. 610

Both meters indicated flow rates higher than the standard, the Matheson about 50% high and the Brooks about 100% high. The Matheson displayed a consistently high indication over a range of flow rates and thus could be corrected by a constant correction factor; however, the Brooks meter displayed erratic behavior for some values of flow rate and a simple correction factor could not be applied. Both rotameters were suspected of being coated internally with a film of fore pump oil which resulted from the daily evacuation of the flow meter lines in order to make a measurement of the barometric pressure using the feed system manometer.

Thermal Capacity Flow Meter: Hastings Model LF-20X

The Hastings meter indicated flow rates about 20% higher then the standard over the range of flow rates and could be corrected by use of a constant correction factor. This meter was also suspected of being contaminated with pump oil.

Laminar Flow Meter: Hico Delta - P Model HICO-20

Neglecting temperature corrections to the standard the laminar flow device agreed with the standard to within 10% over a range of applicable flow rates. Over a flow range which occurred during the calibration check at a time when, fortuitously, the temperature correction was probably unity, the agreement was within 2%.

During the last half of this contract period, the laminar flow meter was used as the primary flow measuring instrument when using the gaseous propellants.

2.2 PULSED PROGRAM

2.2.1 Vacuum System

A vacuum facility was assembled for use in the experimental work of the pulsed program. This facility is shown in Figures 2.2.1 and 2.2.2. The following specifications apply:

vacuum tank: 1.5' diameter, 3.5' long, non-magnetic stainless steel.

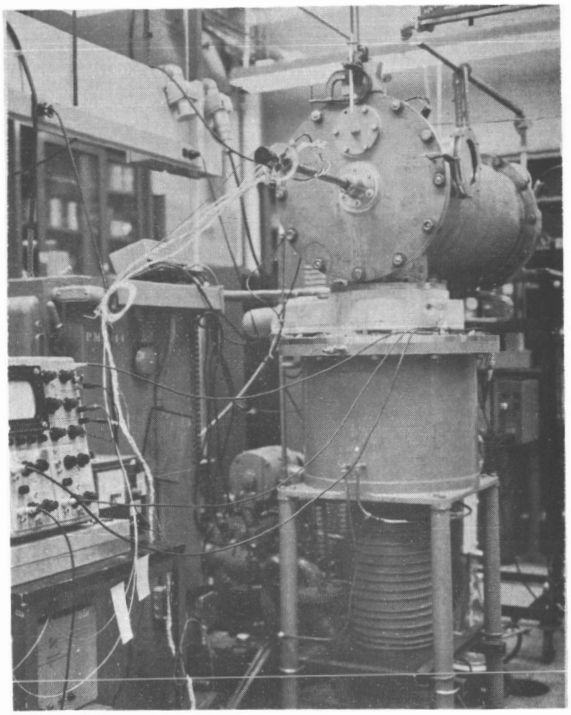

Figure 2.2.1 Vacuum Facility for Pulsed Program - Back View

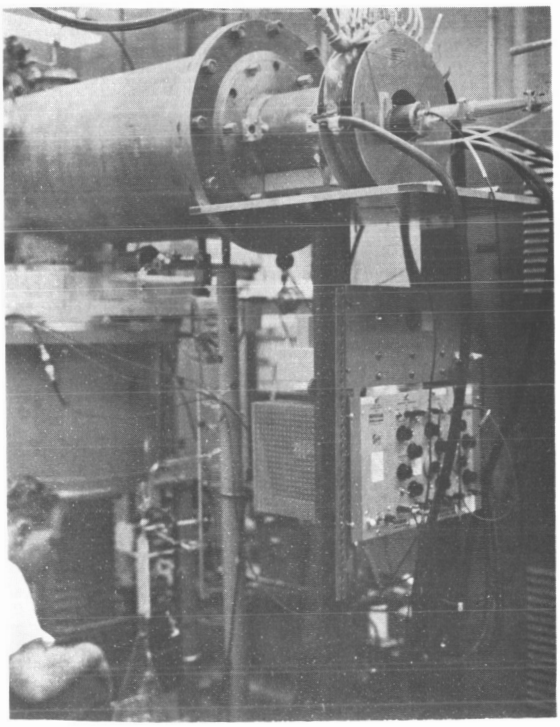

Figure 2.2.2 Vacuum Facility for Pulsed Program - Front View

engine adapter: 8.5" diameter, 11.5" long, brass.

pumping system: (1) oil diffusion pump, rated at 4100 liters per second. With the baffle, the estimated pumping capacity is 2000 liters per second.

(1) holding pump.

(1) fore pump.

ultimate pressure: 8.0×10^{-6} mm (without liquid nitrogen in baffles).

In this facility, the pulsed propellant feed could be operated at 1 μgram/shot and at a pulse rate of two pulses per second while maintaining the background pressure in the 9 to 10×10^{-6} mm range.

2.2.2 R-F System

Figure 2.2.3 gives a block diagram of the r-f system used for the pulsed program. The X-band system was capable of 0 to 5 KW of output power operated on either a pulsed or cw basis. The multivibrator was capable of producing pulse durations of 10 μsec. to 10 millisec. The output of the system was a monotone of 8.35 kmc/sec. The E-H tuner indicated in Figure 2.2.3 was used to minimize power reflected back to the amplifying klystron. For a tuned reflection minimum with no plasma, the loss in the waveguide up to the adapter was found to be about 0.75 db, and the loss in the adapter, circular polarizer, and engine window was found to be about 0.50 db.

Figure 2.2.4 shows the T.W.T., the driver klystron power supply, the amplifying klystron, and the circulator as they appeared in the test facility.

2.2.3 Magnetic Field

The dc magnetic field for the pulsed program was provided by a coil made to specifications identical to those of the coil for the C. W. Program. Field measurements verified the similarity of the two coils.

2.2.4 Pulsed Gas Valve

A solenoid-operated valve was designed for the pulsed program. The design criteria were fast repeatable open-close operation and flow rates comparable to a milligram per second. A cross-section of the valve is shown in Figure 2.2.6.

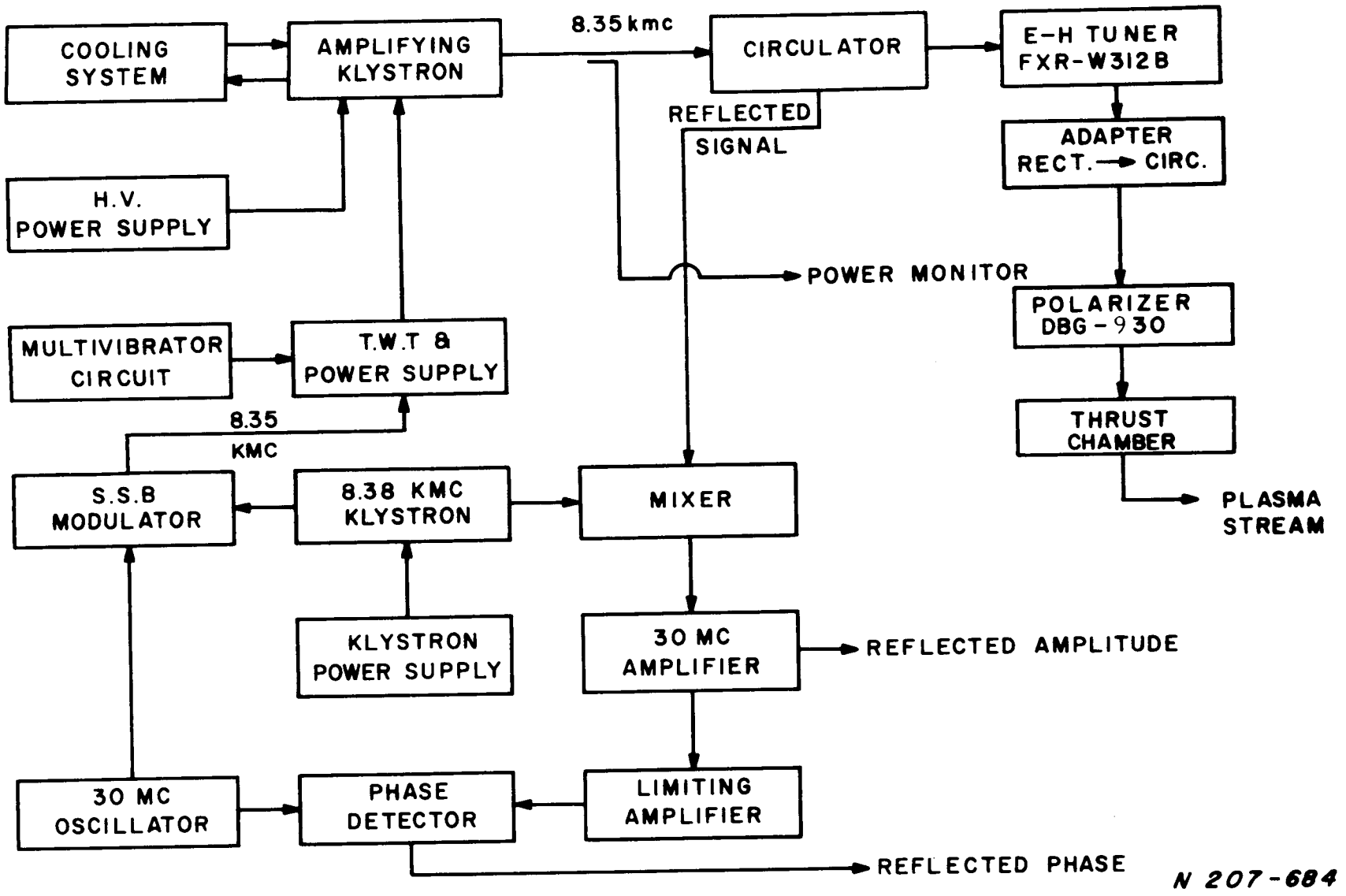

Figure 2.2.3 R-F System Schematic, Pulsed Program, 8.35 kmc/sec.

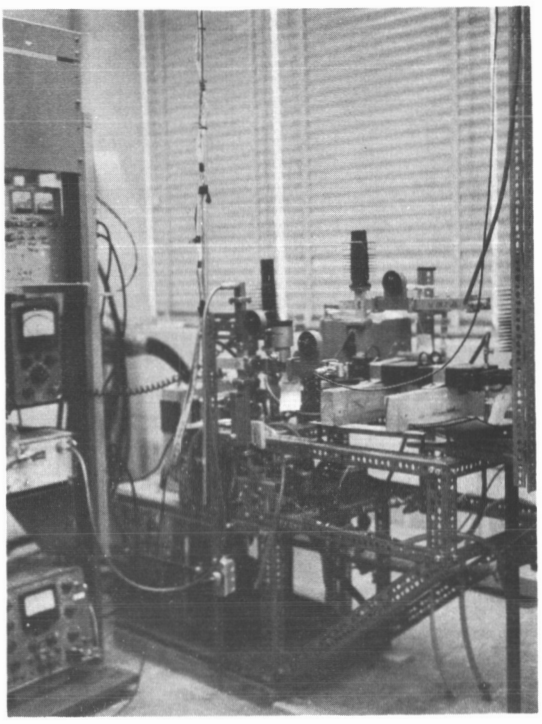

Figure 2.2.4 R-F System, Pulsed Program, 8.35 kmc/sec.

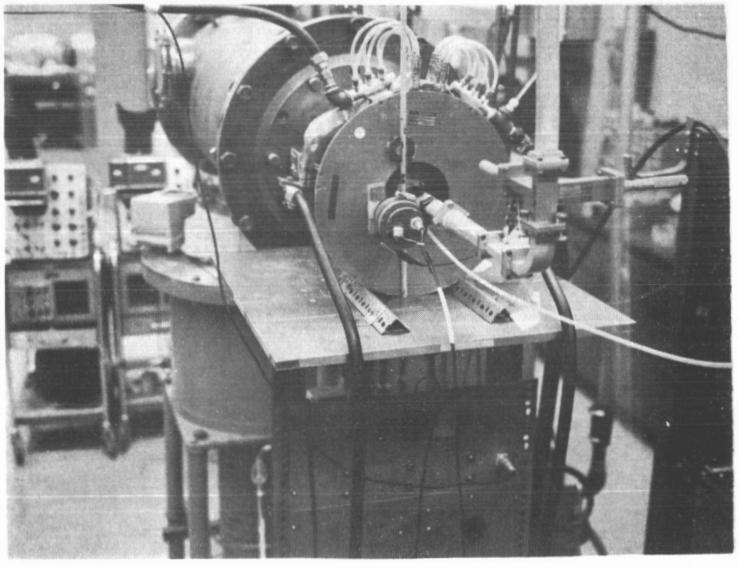

Figure 2.2.5 Shielded Pulsed Gas Valve in Position.

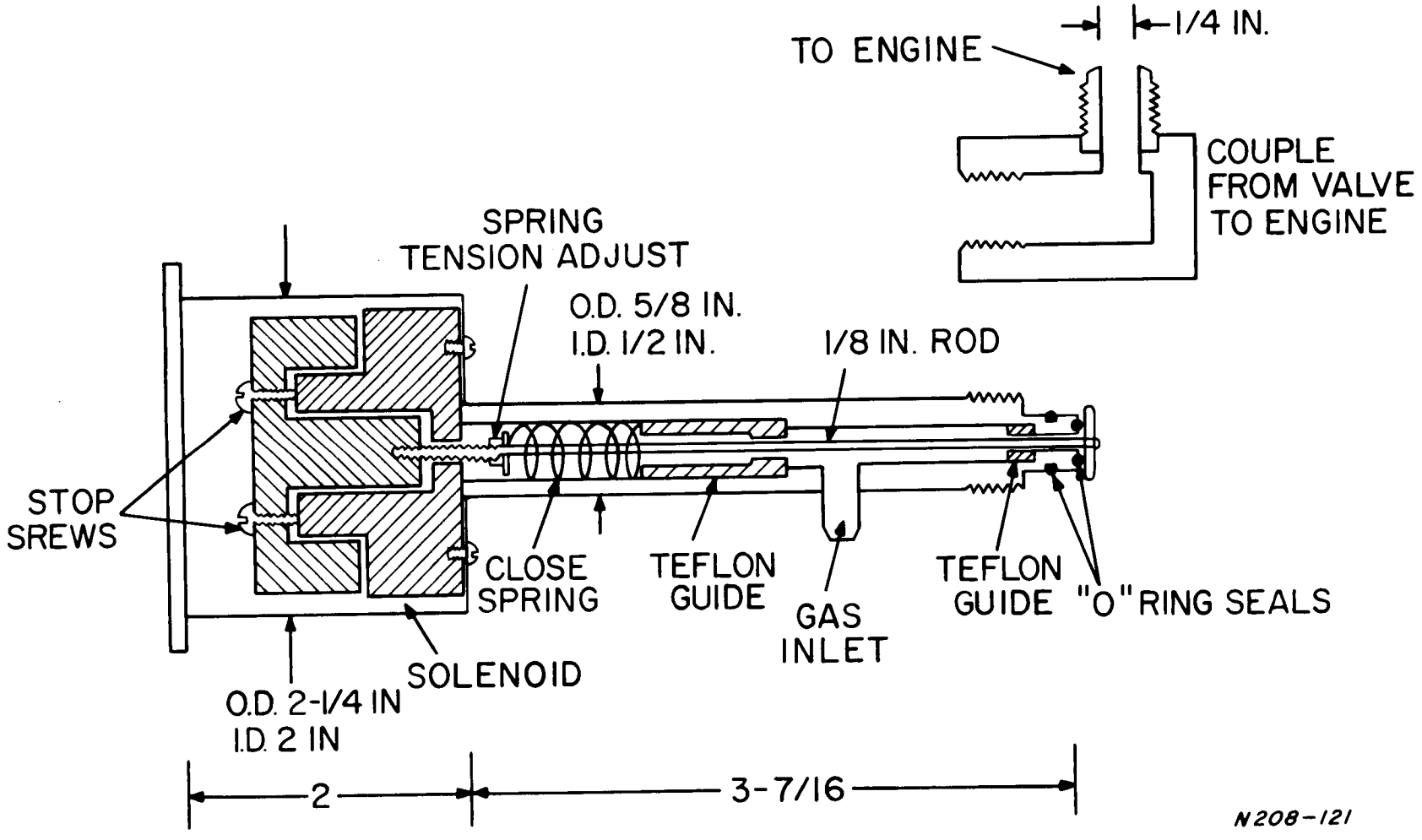

Figure 2.2.6 Pulsed Valve for Propellant Feed.

A power supply was built to actuate the gas valve. It was basically a silicon control rectifier-triggered capacitive discharge. Output voltage peaks could be chosen up to 450 volts, with a solenoid energy of up to 0.05 joules per shot.

Proper valve seating for leak free closure of the gas valve along with injection of desired amounts of propellant was accomplished as a result of proper balance of restoring force, solenoid energy, and maximum opening. The valve was installed in the engine and cold gas pressure profiles were made. An example of a typical gas pulse pressure profile vs. time is shown in Figure 4.2.8. The profile was measured by the gas pressure probe, which will be described later, in the absence of both the dc coil field and the plasma. To protect the solenoid from saturation by the dc coil field, it was necessary to shield the valve casing with iron. With this shielding, valve operation was obtained in the magnetic field of the Cyclops using the full 500 amp dc coil current. The valve may be seen in position at the rear of the coil in Figure 2.2.5.

2.2.5 Thruster

A thruster (Mark IX-L) was designed for the pulsed program. The dimensions of this engine, as seen in Figure 2.2.7, were comparable to the Mark V-L engine used in the C. W. Program. The notable differences were the larger annular propellant duct designed for desired gas flows on a pulsed gas feed basis, the elimination of the coolant duct due to the low average powers anticipated, and the addition of ignition electrodes in the plasma chamber. Tests made on the Mark V-S accelerator in the large vacuum tank using pulsed r-f and continuous propellant flow indicated the necessity for some type of an ignitor to start the discharge. While r-f breakdown occurred when the resonance point was within the thrust chamber, it did not occur at some normally employed magnetic field strengths, where the resonance point was beyond the exit plane of the chamber. The ignitor eventually chosen consisted of a GE No. 43 lamp filament placed in the engine exit plane near the lip of the engine. This device allowed successful ignition for all coil field strengths.

As seen in Figure 2.2.2, the engine was affixed to an engine adapter on the tank. Three small windows were installed in the adapter, two diametrically opposite and very near the engine exit plane, and one near the main tank. The purposes of the windows were to provide access to the plasma stream for spectroscopy and luminosity measurements if desired, and observation of probe positioning in the plasma stream.

A one-half wavelength alumina disc was used as the dielectric window for the pulsed program. The structural integrity of this window was sufficient for the average power levels used.

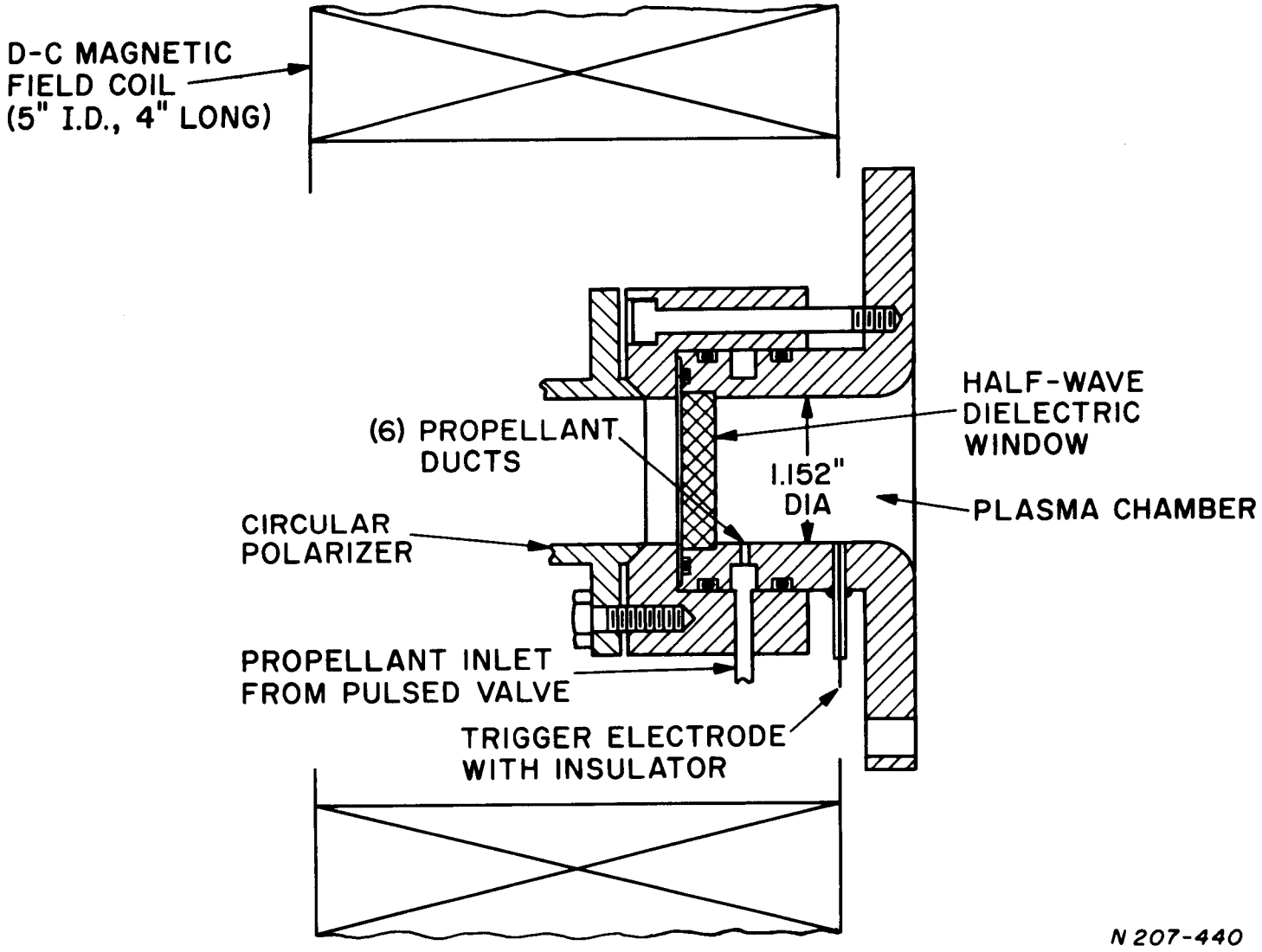

Figure 2.2.7 Pulsed X-Band Longitudinal-Interaction Accelerator; Peripheral Injection (Mark IX-L).

3. DIAGNOSTIC INSTRUMENTATION

3.1 C. W. PROGRAM

3.1.1 Ion Energy Analyzer

The retarding potential probe[1] shown in Figure 3.1.1 was used as an ion energy analyzer. The probe contained two grids, each made of fine nickel screening, the first 200 mesh and the second 500 mesh. The second grid was biased at a negative potential relative to the first, thus repelling electrons but attracting ions. The collector plate behind the second grid was biased at a positive potential relative to the first grid. The first grid was held at ground potential. By varying the potential of the collector plate and recording the ion current as a function of collector plate potential, the integral of the ion energy spectrum was obtained. The derivative of this curve yielded the ion energy spectrum.

Two improvements were made since the probe was used in Contract NAS 3-6266. The first improvement was to change the electrical insulating material used between the grids from teflon to nylon in order to avoid a previously noted degradation of the teflon with usage resulting in spurious probe operation. The second improvement was to record the retarding potential probe data by photographing an oscilloscope display, rather than on an x-y recorder, by using the circuit of Figure 3.1.2. The probe voltage was varied by discharging a capacitor through a resistance. The RC time of the discharge was about 1.4 seconds. Because of the necessity of locating the probe load resistor at high voltage and because of the necessary grounding of the scope input, there existed a known leakage current through the resistor used to measure the ion current. This current resulted in a base line slant (see Figure 3.1.3) that imposed a limitation on the gain of the current axis of the scope trace resulting in a limitation of the obtainable resolution of the ion energy spectrum. The available resolution was sufficient for the measurements at hand, however.

For the measurements made with this probe, the ion current density never exceeded one thousandth of the space charge-limited current density for 500 volts potential difference across the grid spacing used. Thus, space charge effects were considered to be negligible.

Cylindrical tungsten Langmuir probes were located near the retarding potential probe. The Langmuir probes used were made from gold coated, 0.002 in. diameter tungsten wire about one centimeter in length. The probe leads were insulated in the usual manner with a drawn piece of 2 mm pyrex tubing. The gold coating facilitated joining the tungsten wire to an insulated copper lead. After the solder joint had been made, the gold coating was evaporated from the probe surface to prevent its later evaporation and plating onto the pyrex insulator.

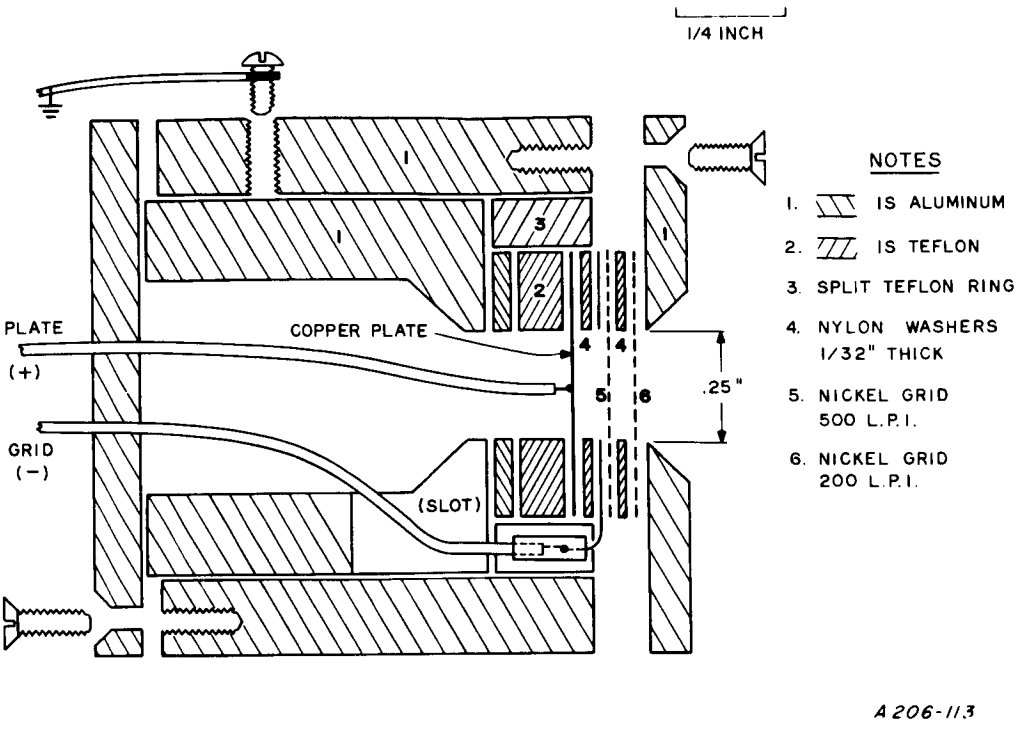

Figure 3.1.1 Ion Energy Analysing Probe.

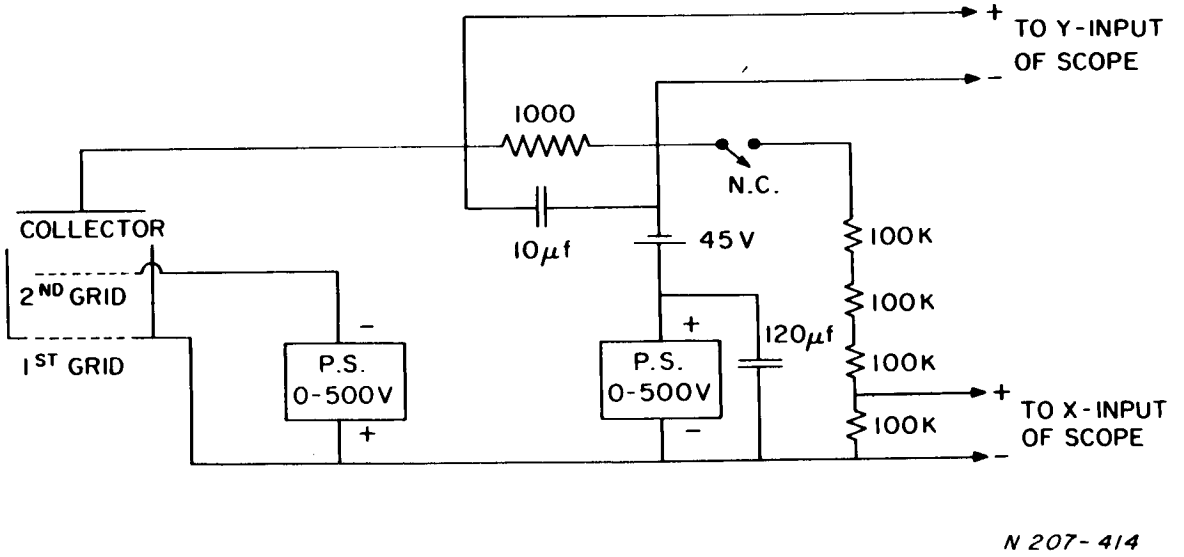

Figure 3.1.2 Retarded Potential Probe Circuit.

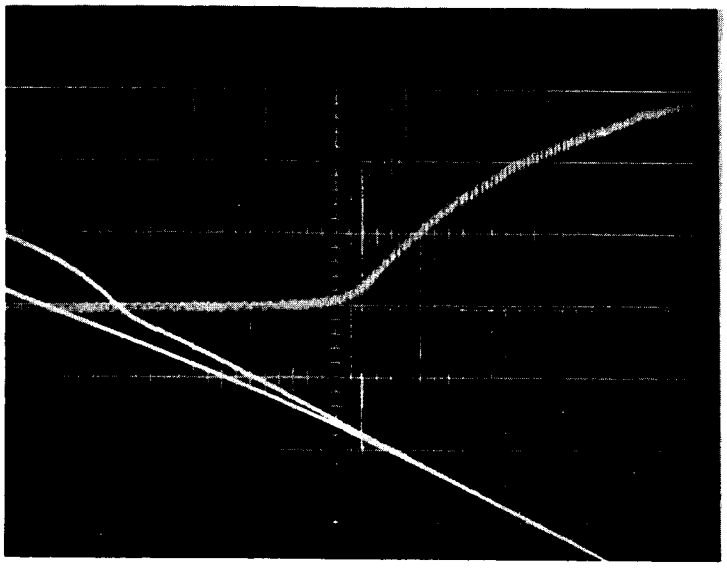

Figure 3.1.3 Typical scope trace recording showing I-V trace and Langmuir probe trace.

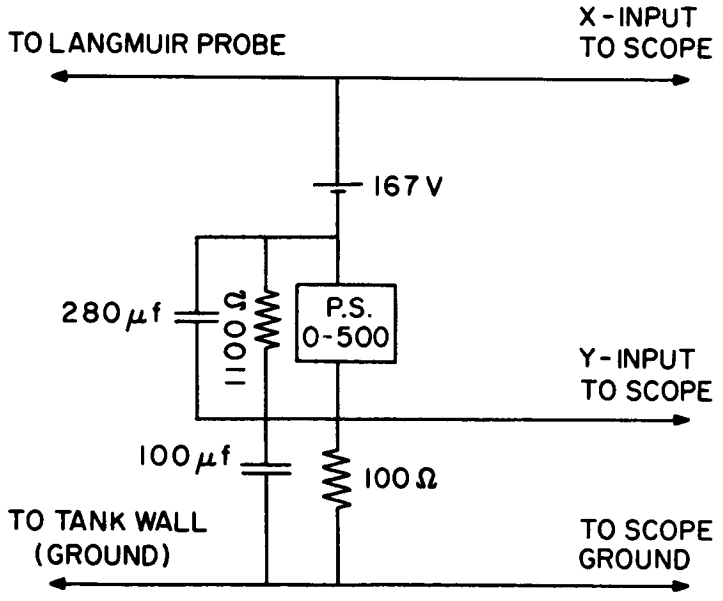

Figure 3.1.4 Langmuir Probe Biasing Circuit.

The biasing circuit for the Langmuir probe is shown as Figure 3.1.4. The probe current was measured using the voltage drop across a 100 ohm resistor connected in parallel with a 100 μf capacitor to provide sufficient filtering.

3.1.2 Potential Probe

The plasma potential probe used was an emitting cylindrical Langmuir probe oriented with its axis perpendicular to the plasma stream. The probe support structure, designed to withstand the high power density near the engine exit port, consisted of a 1 inch O. D. machinable ceramic tube mounted on the end of a quartz tube 3/4 inch O. D., 2 feet long. The quartz tube was mounted on a stainless steel shaft located on the vacuum chamber axis. The shaft passed through a sliding vacuum seal at the far end of the vacuum chamber, thereby allowing adjustment of axial position.

The details of the emitting probe structure are given in Figure 3.1.5 and the circuit for presenting the Langmuir probe characteristics to a scope is given in Figure 3.1.6. In obtaining the data, two traces were run, one with the probe emitting and the other with a cold probe. By comparing the two characteristics, the plasma potential was readily determined as the point of deviation of the two curves[2]. This point is relatively independent of the applicable probe theory, i.e., as the magnetic field in the vicinity of the probe is varied, the probe characteristics change, however, the point of deviation between the emitting and non-emitting characteristic does not change.

3.1.3 Calorimeter

Measurement of the total power carried by the accelerated plasma stream is a relatively simple, accurate, and revealing technique. The plasma impinges on a collector, which, if properly designed, receives essentially all of the plasma energy. The heating rate of the calorimeter, or the steady state temperature rise of a metered calorimeter coolant, then yields a measure of the plasma power. One must take care that the total plasma power is transferred to the calorimeter rather than being carried away by reflected particles, although this is a relatively easy criterion to meet. Radiation and conduction may also carry significant power away from the collector. Interpretation of the measurement is not as simple, however, since <u>total</u> plasma power is measured, including excitation and ionization energies, energy in transverse particle motion, and energy in oscillatory motion. Estimates and independent measurements aid in evaluating the relative importance of these quantities.

The calorimeter used for this work is shown in Figure 3.1.7. It was 10 inches in diameter and 20 inches long. The inlet and outlet water

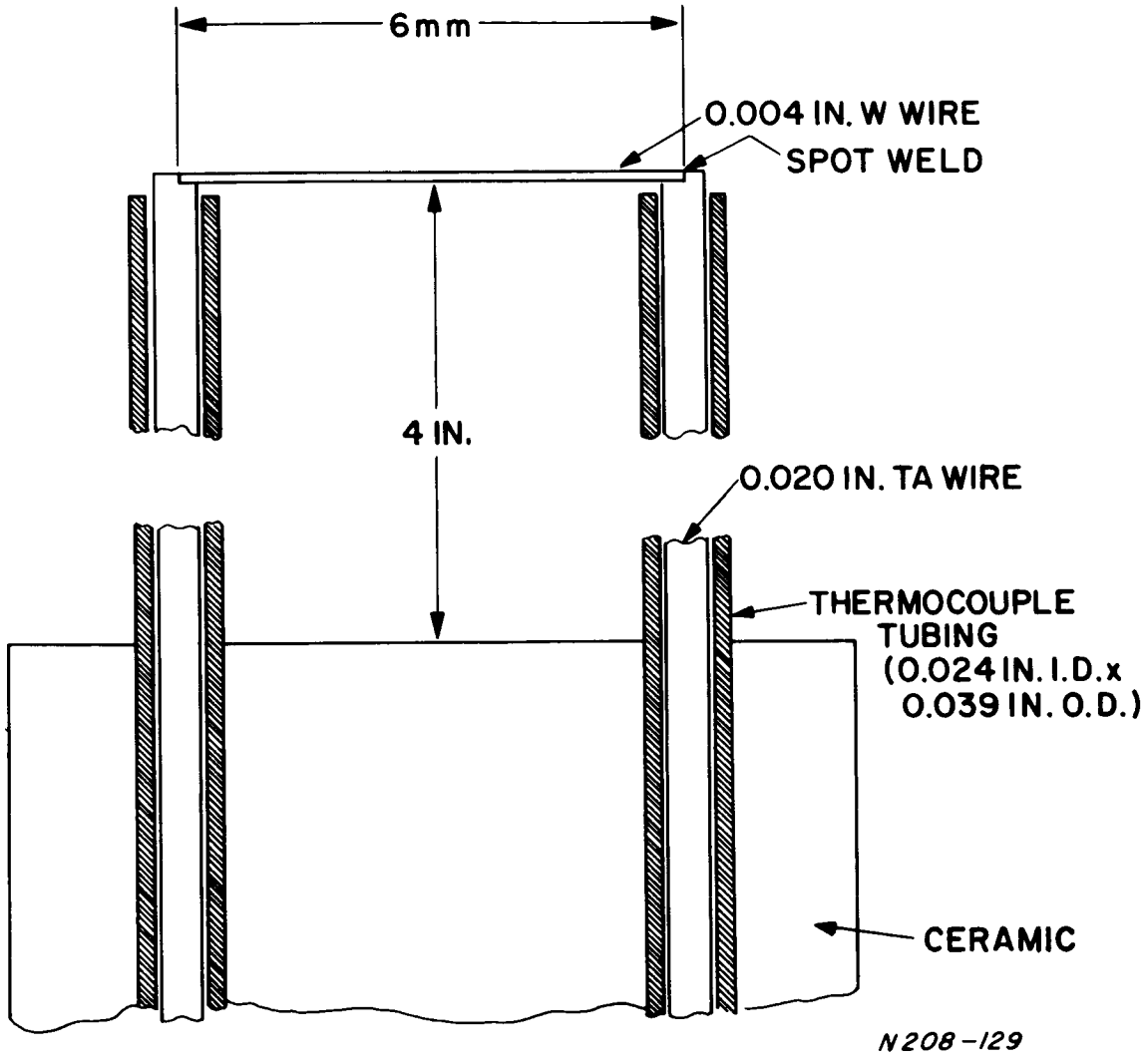

Figure 3.1.5 Emitting Probe Structure Details.

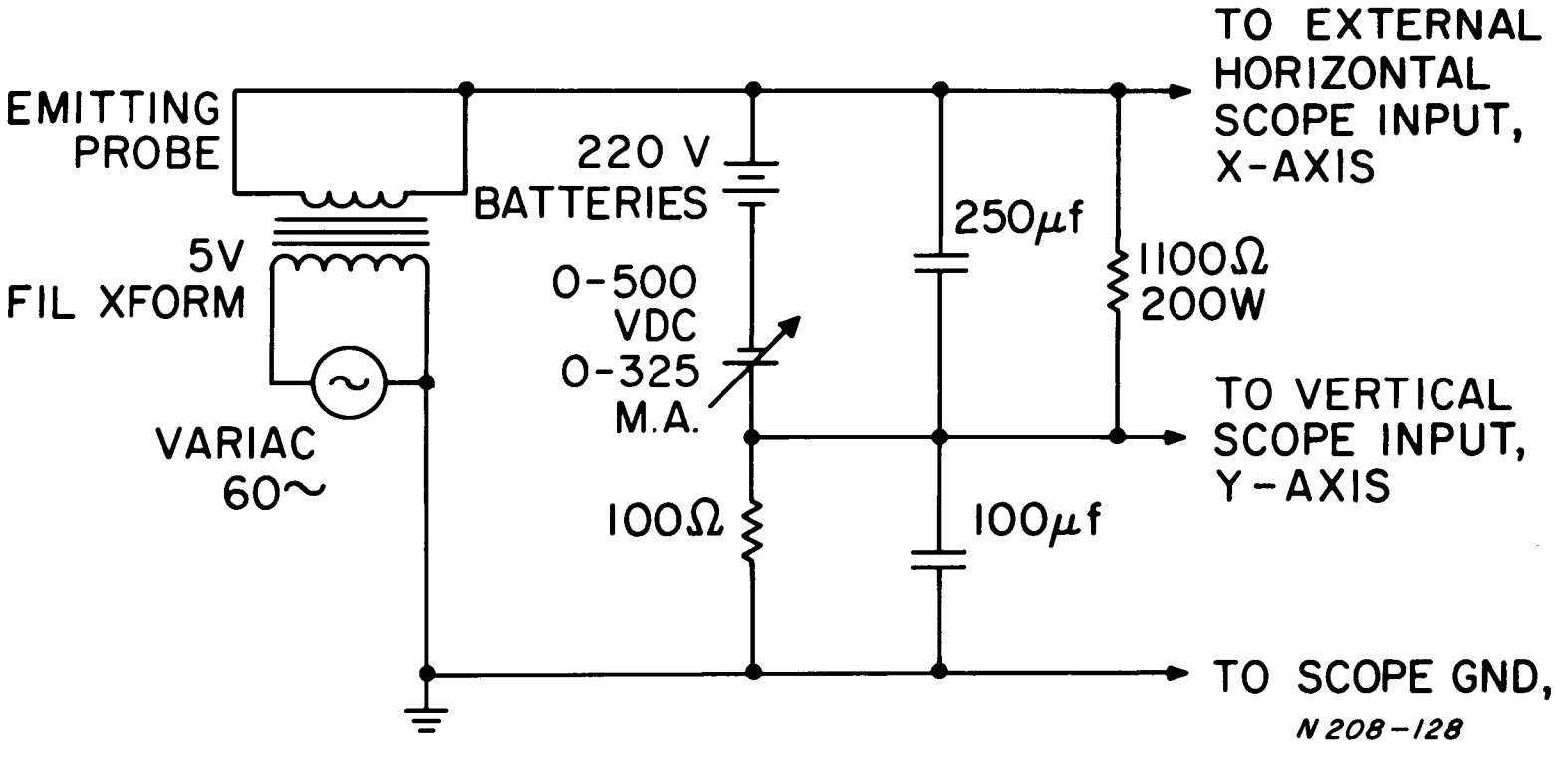

Figure 3.1.6 Emitting Probe Circuit.

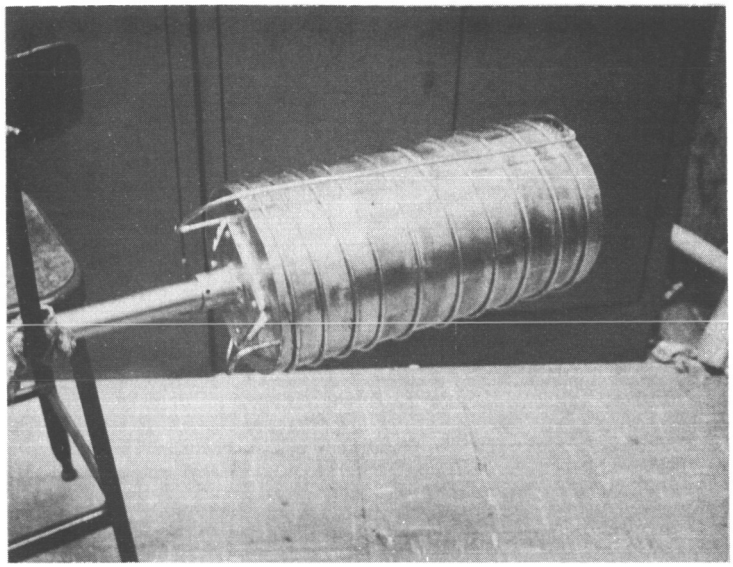

Figure 3.1.7 10" Diameter by 20" Long Steady State Calorimeter, Mounted on Support Shaft.

temperatures were measured with electrically insulated thermocouples immersed in the water lines at points a few inches before entry into and after emergence from the calorimeter collector. Ice baths were used for the reference junctions. A millivolt chart recorder was used to measure and record the thermocouple e. m. f.

3.1.4 Thrust Stand

An assembly drawing of the thrust stand is shown in Figure 3.1.8. Photographic views are shown in Figures 3.1.9-3.1.11. The large rectangular pressure box, which housed the coil and accelerator, was necessary because the coil could not be operated in vacuum. The stand itself, below the box, consisted primarily of positioning tracks for initial and final balancing of the stand. Four thin flexible legs (part #23, Figure 3.1.8) supported the stand and were sufficiently loaded so that slight horizontal thrusts caused appreciable bending of these legs[3]. A linear motion transducer (Sanborn "Linearsyn Type 595DT025, supported by part #33) provided an electrical signal proportional to the displacement. This signal was then amplified (Sanborn Model 3114) and displayed on the Visicord recorder.

Electrical power, coolant water and propellant gas entered through the overhead couplings. Drain lines were attached through the base.

The photograph in Figure 3.1.10 shows the installed stand before attaching the cover plate. The water lines (coil and engine cooling), the electrical power lines (dc for the coil) and the gas input line are visible in this photograph. Water drain lines leading out through the base were installed after these photographs were made. In addition to the normal coil and engine coolant drain lines, an open drain was also required because of coil leakage. Figure 3.1.11 shows the same assembly after installing the cover, polarizer and waveguide sections. The open (left) end of the waveguide was attached to one end of a vertical, 12", flexible waveguide section which in turn was fastened to the vacuum tank; the flexible waveguide section enabled the stand to move laterally while maintaining a tightly coupled and pressurizable waveguide.

Calibration of the stand was achieved by a 1-1/2" x 3-1/2" x .010" piece of brass sheet attached to the waveguide. The spring constant of the brass piece was measured. A precision screw, passing through the vacuum wall and coaxial with and behind the engine provided an accurate means of deflecting the brass piece and therefore of imposing a known, small, axial force on the thrust stand. This calibration could be carried out any time, even while the engine was operating. Before completing assembly of the calibrator, it was determined that the thrust stand sensitivity was symmetric so that calibration was valid even though the calibrator force is anti-parallel to the engine force.

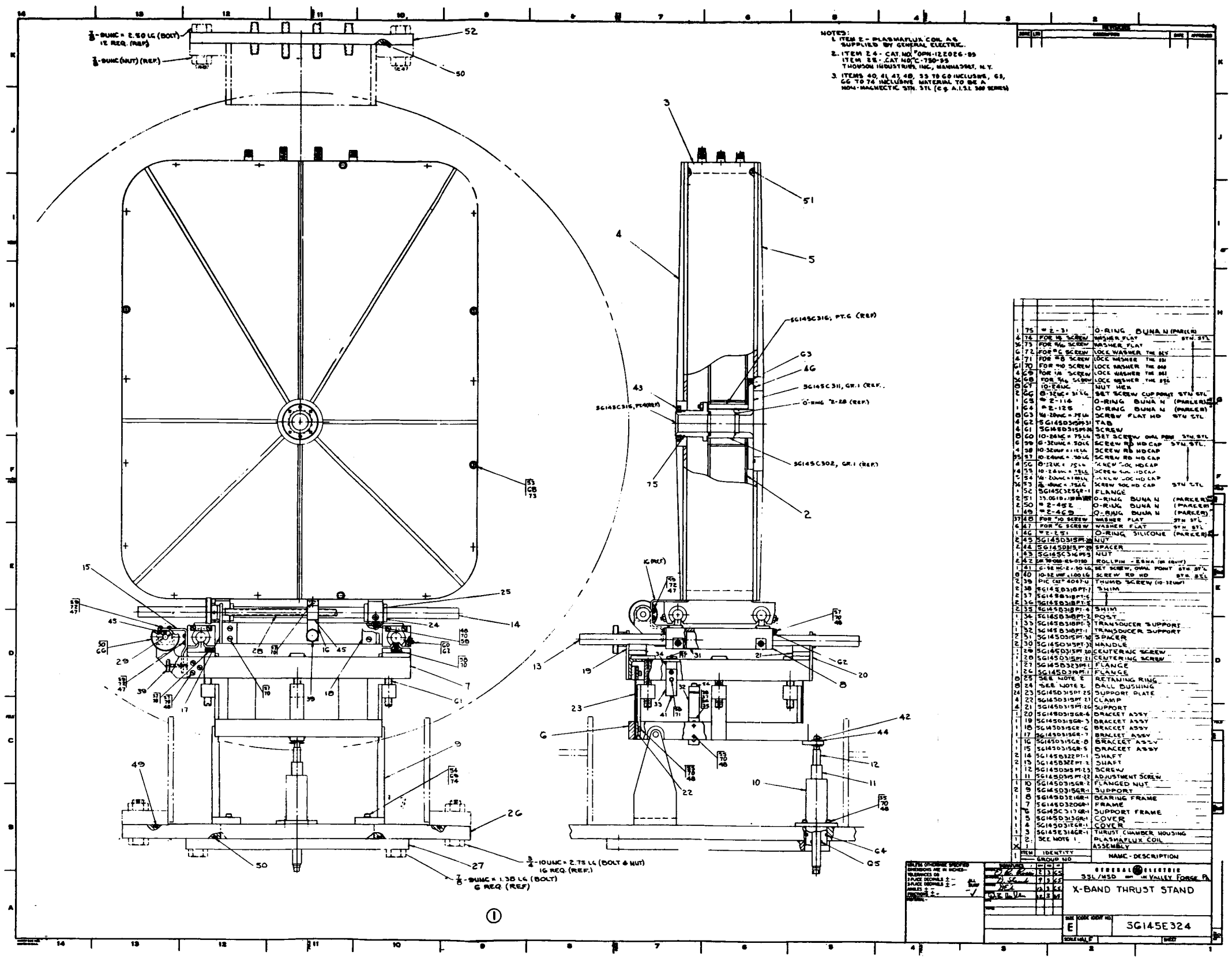

3-9

Figure 3.1.8 Thrust Stand Assembly Drawing

3-10

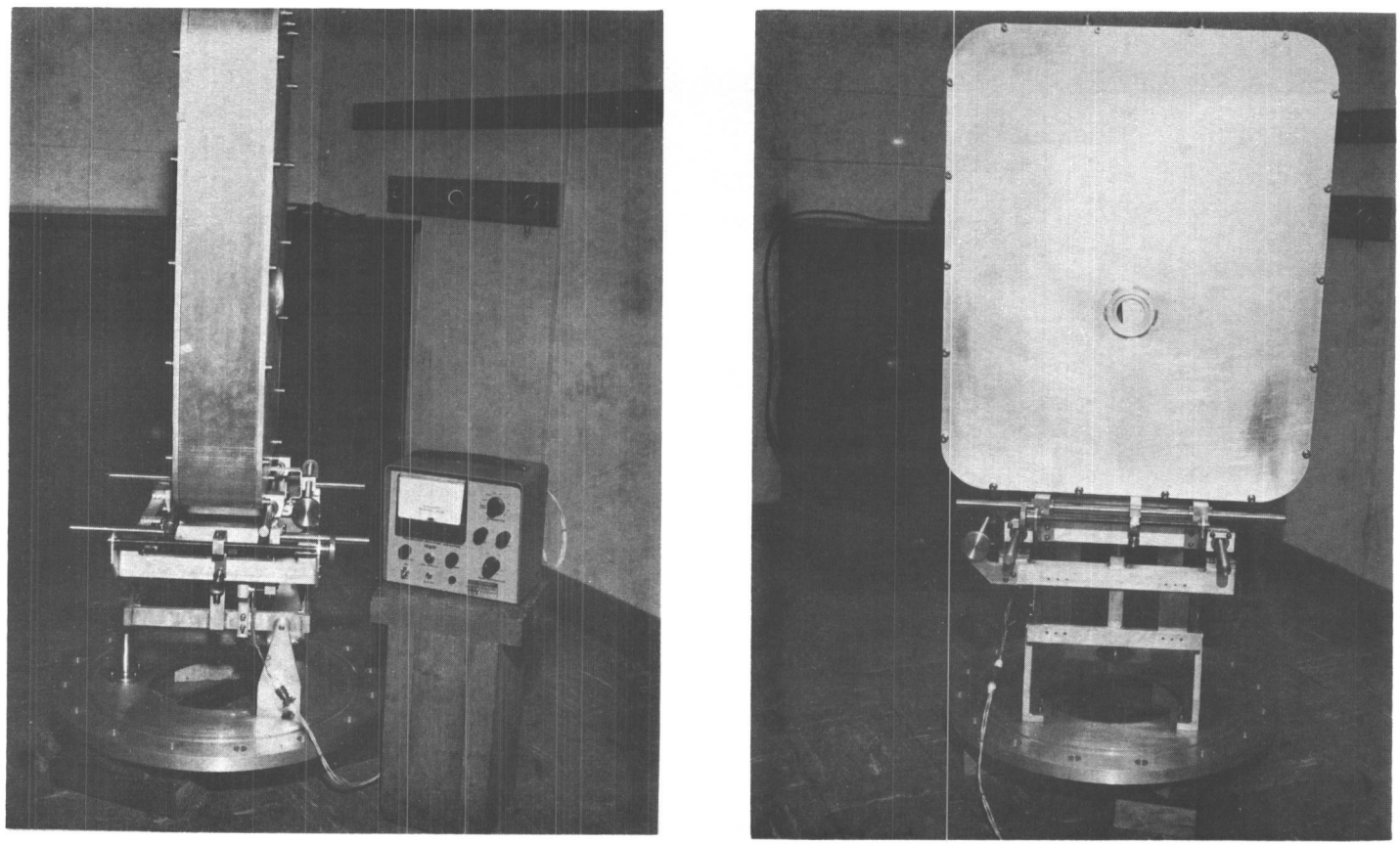

Figure 3.1.9 Thrust Stand, Side and Face Views.

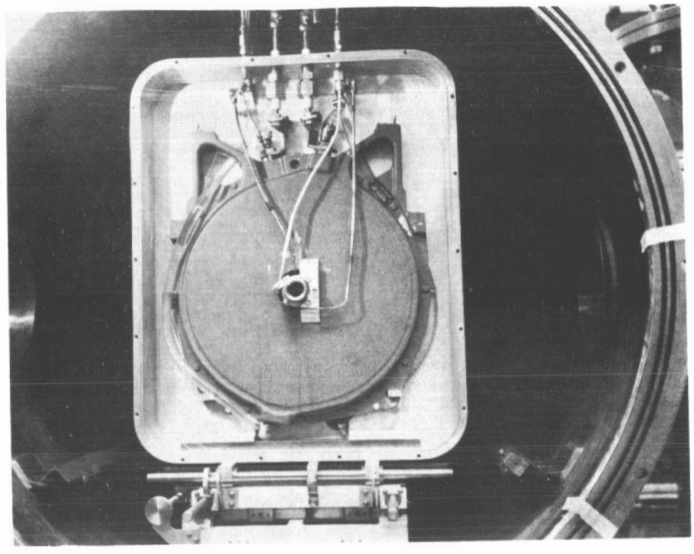

Figure 3.1.10 Thrust Stand with Cover Removed.

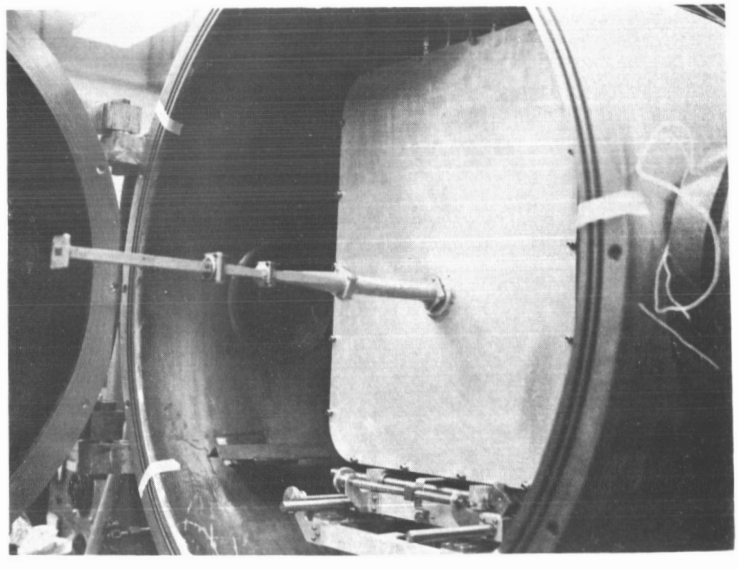

Figure 3.1.11 Thrust Stand with Waveguide Attached.

Each of the four flexible thrust stand legs was made up of one piece of .030" non-magnetic stainless steel sheet. The remainder of the stand was also constructed of non-magnetic material and magnetic pieces were as much as possible removed from the neighborhood of the stand in order to minimize magnetic force effects.

With the thrust stand mounted inside the vacuum chamber a number of instrumentational problems were uncovered which limited the applicability and precision of this device. These are listed below.

1. Magnetic effect: Detectable forces were exerted on the thrust stand due purely to the interaction of the dc magnetic field with miscellaneous ferromagnetic items in the laboratory. For any given field level this was constant and so could be subtracted out.

2. Thermal effects: When the r-f was turned on, with or without a plasma, a slow position shift results, probably due to the waveguide heating and expanding. One procedure which had been used is to turn the r-f on first and let the thrust stand seek a new equilibrium zero before igniting the plasma by turning up the magnetic field.

3. Vibration: The large mechanical pump created a vibration signal on the thrust stand transducer output comparable in magnitude to the thrust signal. The vacuum tank was mounted on vibration absorbing pads and was further isolated from the pump by a bellows section in the vacuum line. It was believed, however, that much of this vibration was being carried into the thrust stand by water lines.

The thrust measurements made during the first half of this contract period were made with the thrust stand installed as described above. During the later portion of this period, the thrust stand was set up outside the chamber with the engine mounted rigidly on the port cover and the coil freely suspended on the thrust stand as shown in Figure 3.1.12. With this arrangement, the problems of running a coil inside a vacuum chamber but at atmospheric pressure were eliminated, however, a new problem was encountered.

The new problem was due to the eddy current interaction between the port cover to which the engine was rigidly mounted and the coil mounted on the thrust stand. The eddy currents were the result of the absence of regulation of the coil power supply. Line voltage fluctuations thus appeared as random impulses or noise to the thrust stand. The effect was reduced by increasing the distance between the coil and port cover (by standing the engine off using an insulating collar), by slotting to break up eddy current paths (Figure 2.1.9), and by changing the material from aluminum to stainless steel thereby increasing its resistance. These modifications reduced the noise level to about the equivalent of 5 mn of thrust which was considered a tolerable level.

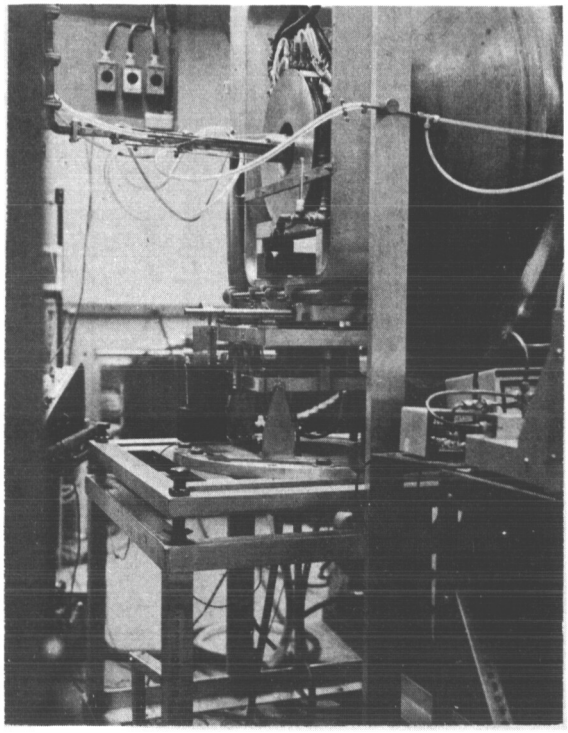

Figure 3.1.12 Externally mounted thrust stand with coil suspended on thrust stand and engine mounted on port cover.

3.2 PULSED PROGRAM

3.2.1 (R, θ, Z) Probe Positioner

In order to probe the engine interior and the plasma stream both on and off-axis with a desired degree of position repeatability, a traversing probe carriage was designed and built for the pulsed program. The resultant probe carriage may be seen in Figures 3.2.1 and 3.2.2, with the gas pressure probe mounted thereon. An extension arm was affixed to the radially traversing rack to keep the main carriage body out of the interaction region. The positioner is shown installed in the tank in Figure 2.2.1. A support was installed inside the tank to keep the carriage shaft from deflecting and binding with the "O" ring at the rear of the tank.

Slight misalignments between rear and front tank plates, engine adaptor, and engine combined to disallow simple centering of the probes. By calibration with each probe, however, a good knowledge of probe position for the given R, θ, and Z was obtained.

3.2.2 Data Recording Techniques

Attempts were made to simplify data taking as much as possible, principally by using a CRO as an x-y plotter. A potentiometer was attached to the shaft which controls the position of the radially traversing probe carriage rack. For a given axial position (Z, relative to the dielectric window) and azimuthal position (θ), the probe was carried along a radial line by the traversing rack. The radial position was displayed on the x-axis of a scope by the potentiometer voltage controlling the sweep of the beam. The y-axis position was a function of the signal amplitude of the probe device. The data were then recorded by a photograph of the CRO face for a given traversal. Examples of the results of this technique may be found in the experimental results section of this report.

3.2.3 Gas Pressure Probe

The gas pressure probe, a CK5702 pentode, is shown in Figures 3.2.1 and 3.2.2. In these photos, the glass envelope was still intact. In actual usage however, the glass was removed and the bare tube was employed to relate ion current to gas pressure[4].

The small mesh screens seen in the figures were to be employed as repelling grids. The outer one was to be at a high negative potential and the inner one some positive potential to retard all charged particles and allow the detection of neutral gas. Operation of the gas density probe in this capacity was unsuccessful, most likely due to secondary emission at the screens. This general problem is treated more completely later on in

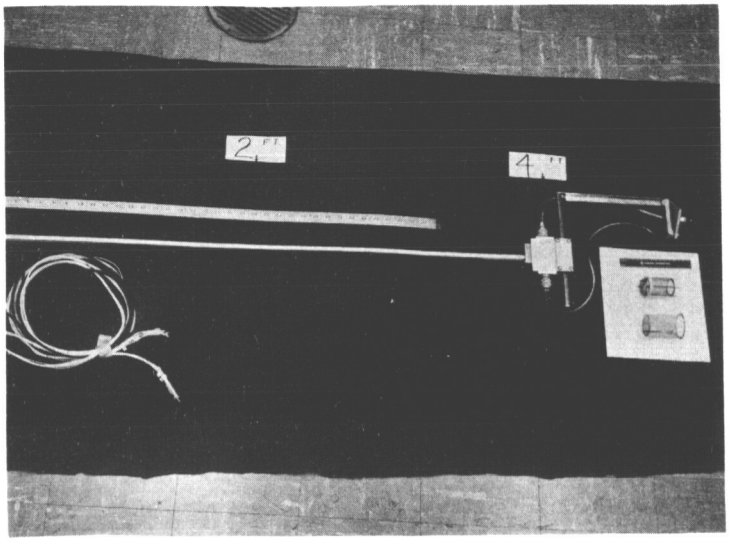

Figure 3.2.1 Probe carriage, gas pressure probe installed.

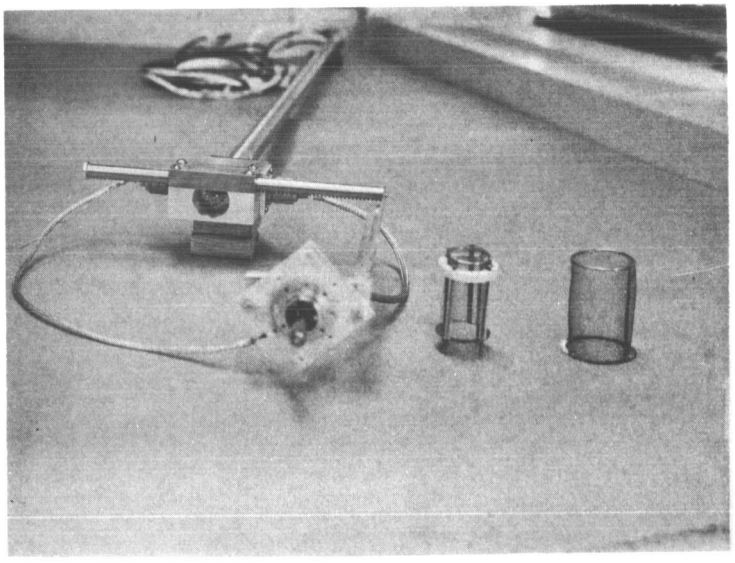

Figure 3.2.2 Probe carriage, gas pressure probe end view.

regard to the operation of the ion-energy analyzer probe.

It is interesting to note that the pentode detector was operated successfully in the region of high magnetic fields in the absence of a plasma. This was accomplished by shielding the tube with a small cup of iron containing enough drill holes to allow free passage for neutrals. The signal amplitude for a given gas pressure was somewhat decreased, but a calibration seemed quite possible.

The circuit for the pressure probe is shown in Figure 3.2.3. The probe was oberated with about 150 V on the second grid and -24 volts on the plate. A feedback circuit was employed in order to maintain the emission current at a constant 2 milliamps.

3.2.4 R-F Probes

Miniature antenna stub probes were used to map the electric field. The probe signal was rectified through a crystal detector and displayed on the y-axis of the CRO. By careful shielding adequate signals were obtained using stub lengths on the order of one-eighteenth of a wavelength. The probe design may be seen in Figure 3.2.4A.

As seen in Figure 3.2.4B, two orthogonal probes were used for simultaneous measurements of the radial and azimuthal components of the electric field. One probe was positioned parallel to the radially traversing rack. Crystal rectifiers were chosen to balance the signal output of the two probes for the free-space electric field mappings. The same probes were used for the field mappings in the plasma, with one of the two signals filtered by a spectrum analyzer. The noise reduction resulting from filtering may be seen in the experimental results.

3.2.5 Magnetic Probe

An experiment was performed to determine the magnitude of the diamagnetic effect due to electrons in cyclotron motion near resonance. An 8 inch diameter, 6 turn coil was built. The coil loops were shielded from radiation by a grounded copper tube. This in turn was shielded from the plasma by a plastic tubing cover. The coil is shown in Figure 3.2.5.

The output coil leads were then fed to the differential amplifier of a scope. The magnitude of the induced voltage was then displayed during the plasma pulse.

The design theory and capability of the probe may be found in Appendix A.

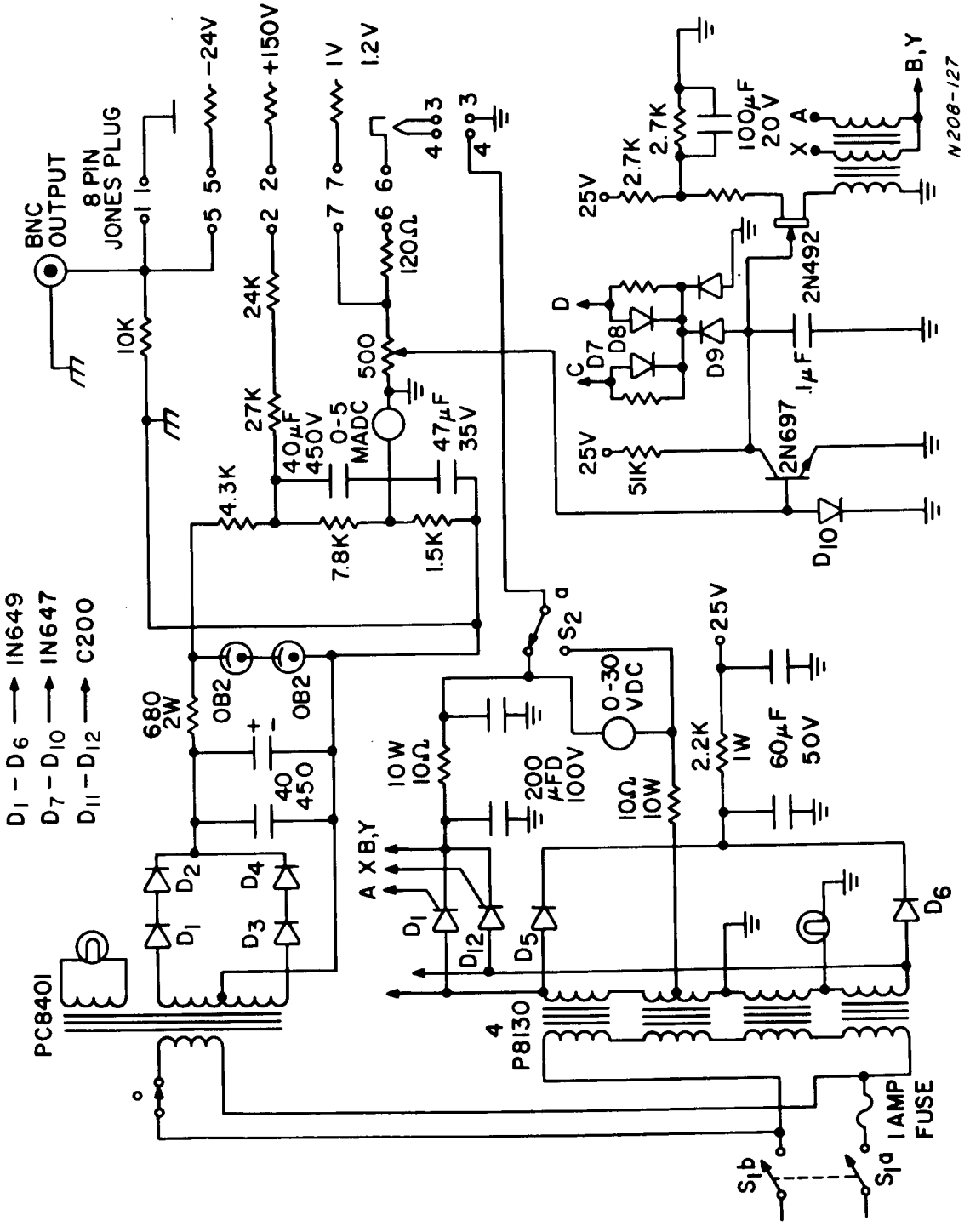

Figure 3.2.3 Circuit for the Gas Pressure Probe.

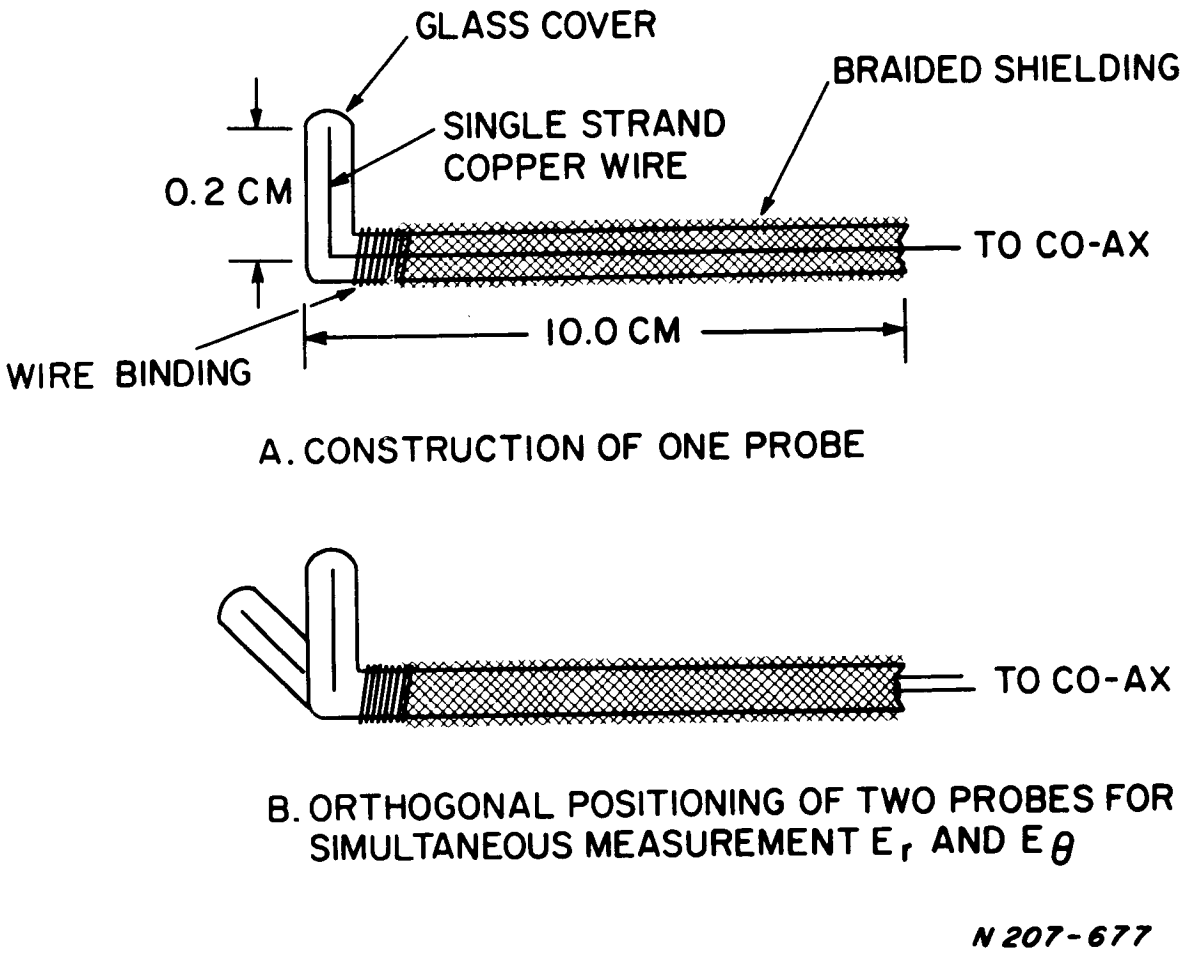

Figure 3.2.4 Movable R-F Probes.

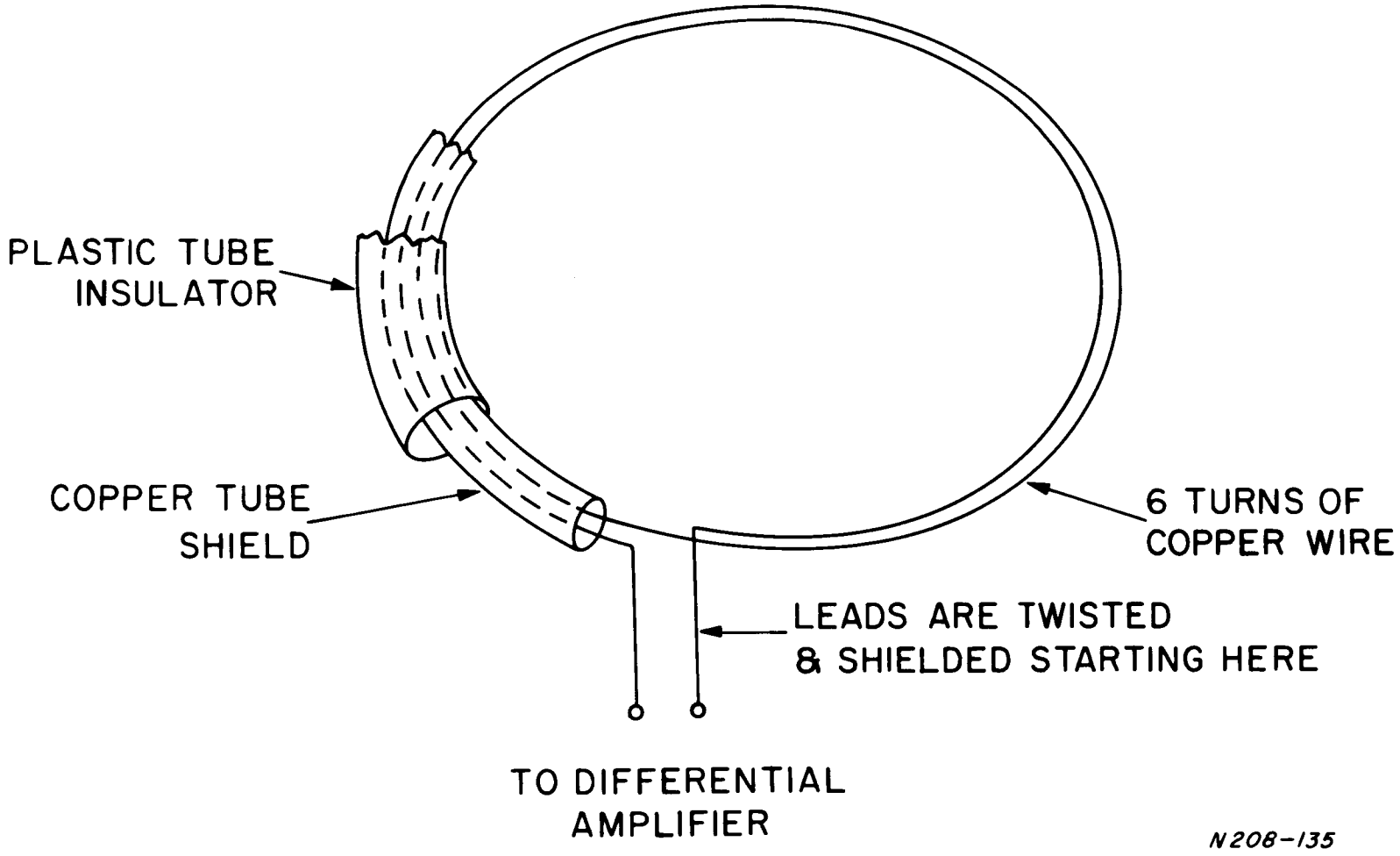

Figure 3.2.5 Probe for Detection of Diamagnetic Effect.

3.2.6 Langmuir Probes

Langmuir probes were used to determine the electron energy at various positions in the plasma stream. Because of the low average powers occurring in the pulsed experiment, no special construction design was needed to maintain the probe integrity during the experiments. Two cylindrical probes were used, one aligned with the field lines to measure the transverse electron temperature component and the other aligned perpendicular to the field lines to determine the longitudinal component of electron energy. (The concepts of temperature and energy will be treated as interchangeable in discussions of these probe results.) The design of the two probes may be seen in Figures 3.2.6 and 3.2.7. Both were designed to withstand heating in order to be used as emitting probes for plasma potential measurements and in order to be cleaned periodically since the probes drew very little current in the pulsed mode of operation.

The circuit for the probe current measurement is shown in Figure 3.2.8. The scope is used with this circuit as an I-V (X-Y) plotter. In order to avoid the problems arising from a fast voltage sweep during a plasma pulse, data sampling was employed throughout this series of runs. This was accomplished as follows:

The power supply charged the capacitor (700 μf) and was then shut down. The RC decay time was about 10 seconds. The plasma was then ignited at a rate of twice per second, with the r-f synchronized to fire at some point within the gas pulse. The CRO (Tektronix No. 541) was then intensity modulation synchronized to some position within the r-f pulse, sampling the load resistor voltage for some hundred microseconds. This value was then seen as a bright dot on the screen, while the remainder of the time (that time between pulses) a faint but steady base line was drawn. Therefore, the plasma was sampled on a pulse-to-pulse basis, and the continuity of the data indicated the uniform plasma conditions which existed from shot to shot. These data represent the average plasma conditions. The synchronizations and a resultant trace are illustrated in Figure 3.2.9.

3.2.7 Ion Energy Analyzer Probe

The retarding potential probe[5] shown in Figure 3.2.10 was used as an ion energy analyzer. It was a four gridded probe, with the first and last grids 200 mesh copper screening, and the middle two grids 500 mesh. The last grid was at ground potential. The third grid was at -200 volts to repel incident electrons from the plasma. The second grid had a variable positive potential applied for separating out the ions that had energies below the stopping potential. The first grid was used to regulate the currents generated due to secondary emission from all sources. (A discussion of the problems involved with this effect may be found in Appendix D.) No bias was applied

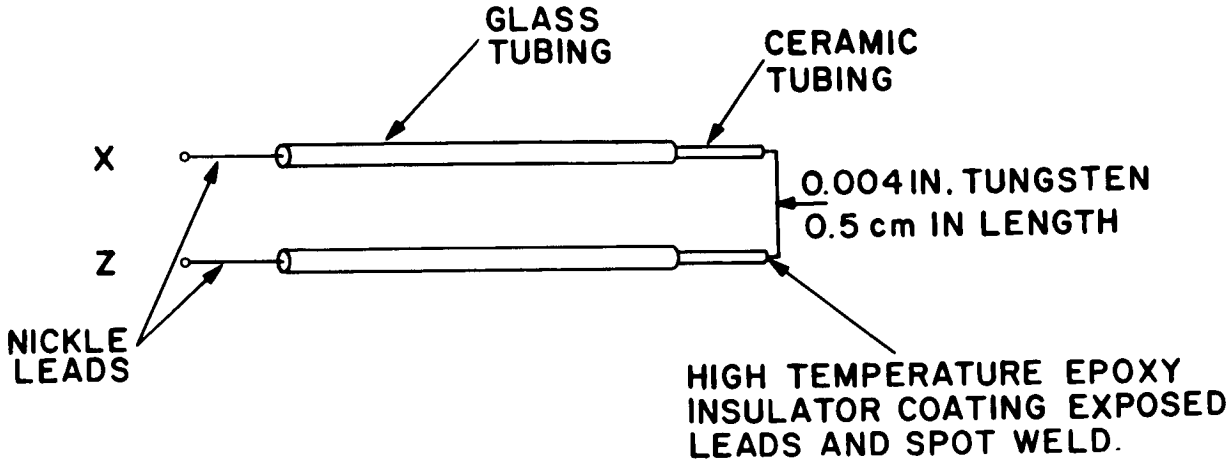

Figure 3.2.6 Transverse Probe for $Te_{//}$.

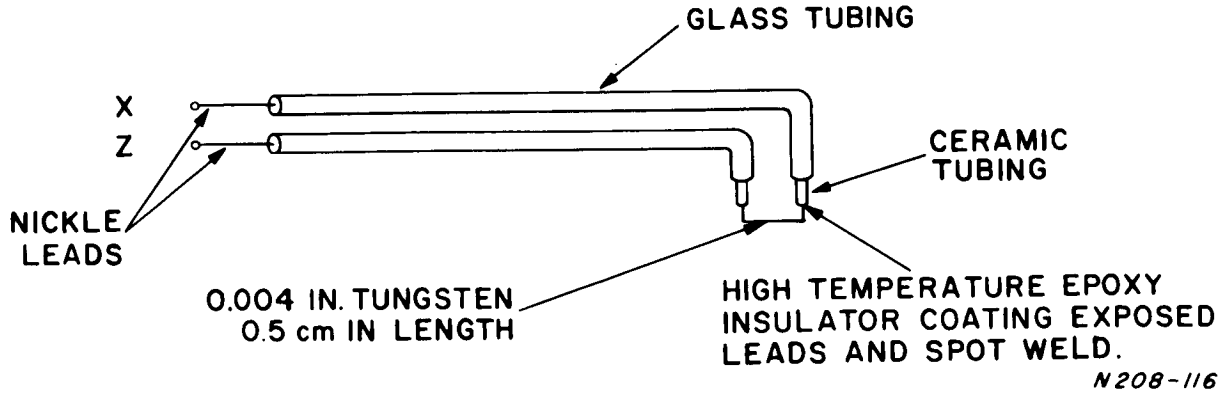

Figure 3.2.7 Longitudinal Probe for $Te_{\perp}$.

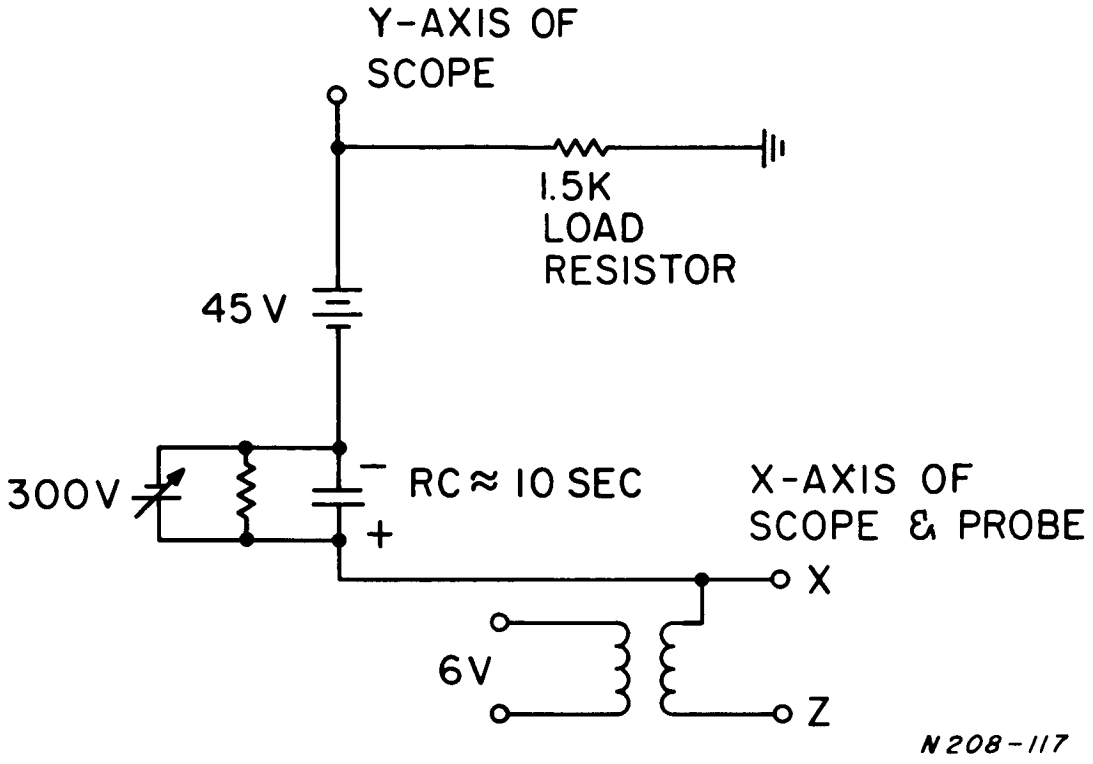

Figure 3.2.8 Langmuir Probe Voltage Sweep Circuit.

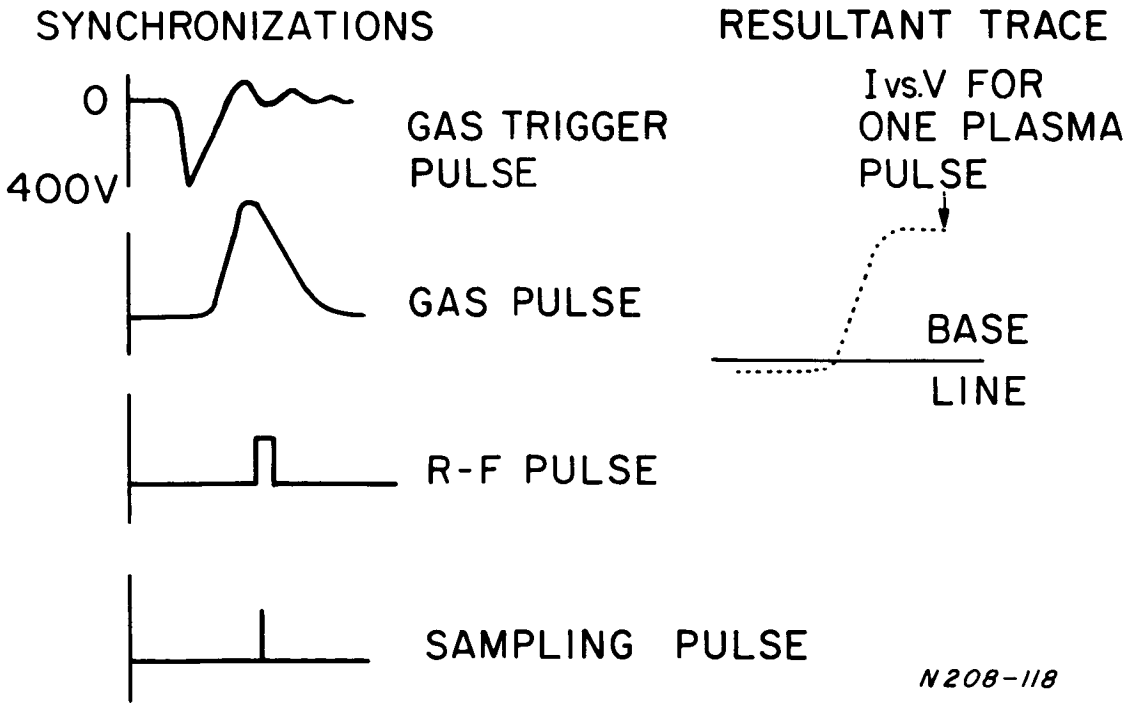

Figure 3.2.9 Synchronizations for Langmuir Probe Data and Resultant Trace.

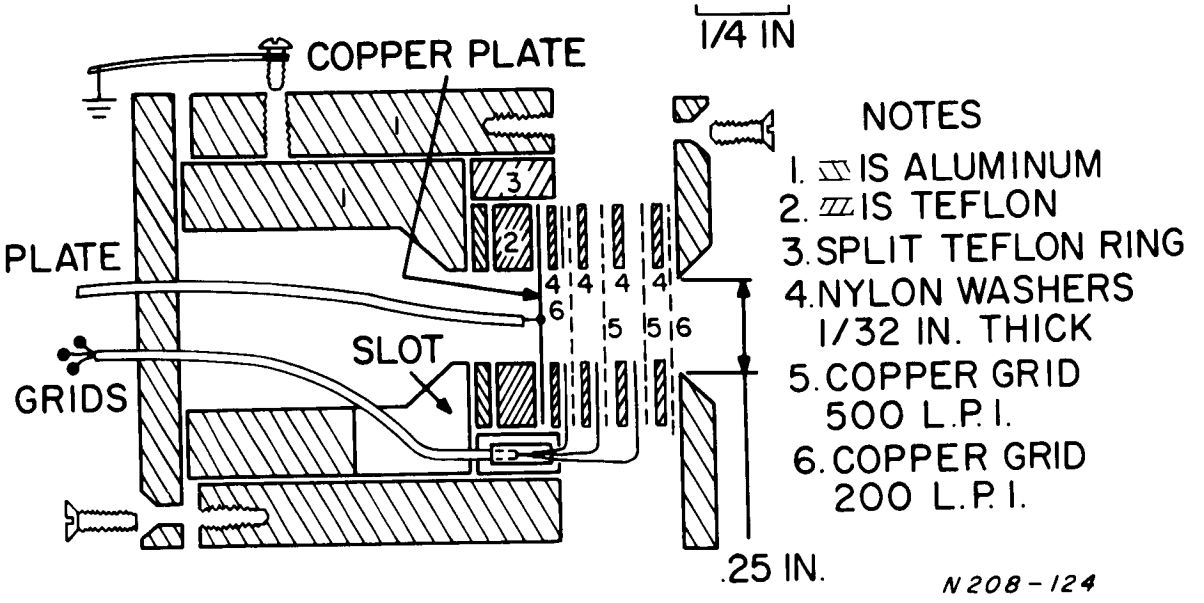

Figure 3.2.10 Ion Energy Analysing Probe.

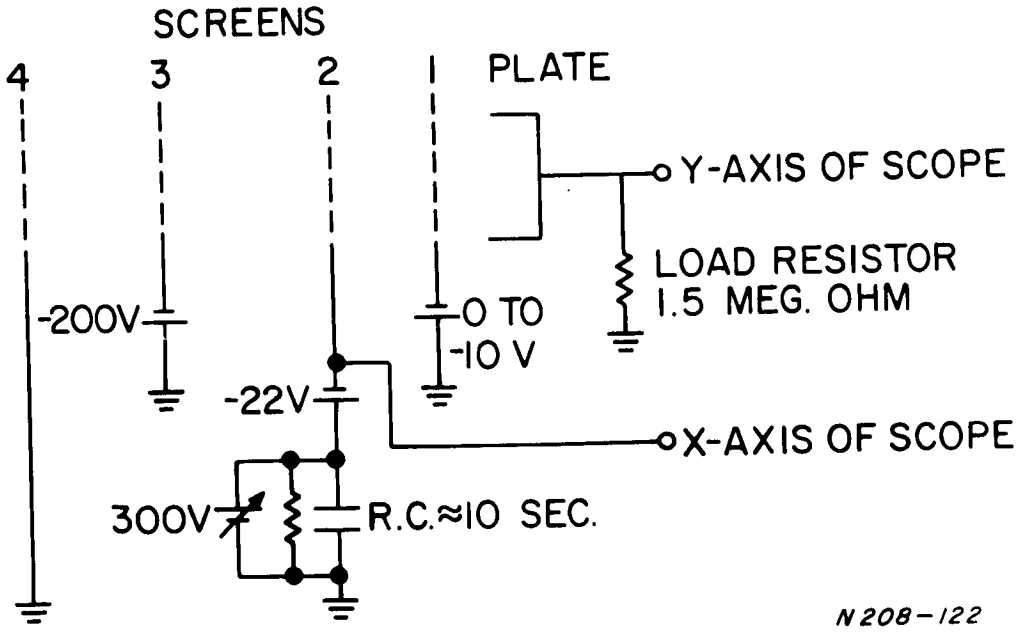

Figure 3.2.11 Retarding Potential (Ion Energy) Probe Circuit.

to the collecting plate. The resulting ion current was measured across the load resistor, as seen in the schematic of Figure 3.2.11. Again, the sampling technique of data taking was employed for some of these measurements.

A fast sweep version of the experiment made use of a Miller integrating circuit which provided a nearly linear voltage sweep from 0 to 300 volts in 50 microseconds. The instrumentation required for this modification is pictured in Figure 3.2.12. The scope on the left provided a phase-delayed intensity modulation for the scope on the immediate right. The delay scope was triggered by the r-f pulse trigger. The voltage sweep was positioned at some point within the r-f (plasma) pulse. A positive gate pulse was delayed to synchronize with the occurrence of the voltage sweep. This gate was then used to intensify the scope trace on the right during the voltage sweep; this scope then displayed a characteristic I-V curve, brightened only during the pertinent voltage sweep.

The trigger unit for the voltage sweep circuit is seen in the background (sitting on the previously mentioned spectrum analyzer, which was not used for this experiment). The scope on the extreme right monitored the relative position of the r-f pulse within the propellant gas pulse.

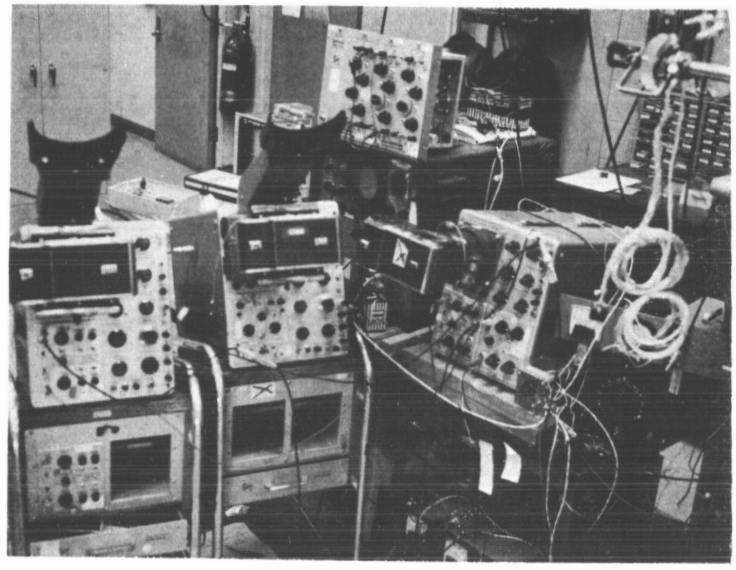

Figure 3.2.12 Instrumentation for Ion Energy Analysis.

4. EXPERIMENTAL RESULTS

4.1 C. W. PROGRAM

4.1.1 Beam Power Measurements

The 10" diameter x 20" long, water-cooled calorimeter was briefly installed in the 4' tank (along with the Mark V-S accelerator mounted on the thrust stand) as shown in Figure 4.1.1. Table 4.1.1 shows the results.

The calorimeter temperature record for the last run is shown in Figure 4.1.2. During this run, after the calorimeter temperature had stabilized, a sheet-metal shutter was lowered in front of the calorimeter blocking the calorimeter entrance but not obstructing its side collecting area. The calorimeter temperature dropped off to about 20% of its unobstructed value, indicating that, even this far back where the background plasma is relatively high, most of the power is entering via a longitudinally directed stream.

4.1.2 Thrust Measurements - Ar, Kr, Xe - Internally Mounted Thrust Stand

The Mark V-S accelerator mounted inside the vacuum chamber as shown in Figure 4.1.1 was run many times, employing a wide variety of conditions: R-f power between 800 and 2500 watts; argon, krypton, and xenon propellants; mass flow rates between 0.25 and 2.0 mg/sec. While making thrust measurements, the calorimeter was removed from the vacuum chamber and the ion energy analysis probe was moved aside so as to be outside of the beam.

During operation of the thrust stand, the noise and vibration levels were unfortunately quite high. Rather serious continuous zero drift was also encountered, probably due to the thermal expansion of the waveguide. Magnetic deflections were also observed. Because of these various adverse effects, actual thrust measurements were made by noting the change in thrust stand position at the instant of r-f power shut down. A typical record is shown in Figure 4.1.3. The noise, drift and magnetic effects are obvious here, but the shift in position at shut down is also clearly observable and measureable.

If the data in Figure 4.1.3 are evaluated, the overall efficiency ($T^2/2\dot{m}P$) is calculated to be 0.46 and the specific impulse ($T/\dot{m}g$) is 6300 seconds. Reactions up to 51 millinewtons ($\sim$ 5 gm) have been measured; at 51 millinewtons the input gas flow (krypton) was 1.7 mg/sec and the input r-f power was 2080 watts, yielding a total efficiency ($T^2/2\dot{m}P$) of 0.38. A large number of additional data points were accumulated with the internally mounted thrust stand and are shown in Figures 4.1.4, 4.1.5 and 4.1.6.

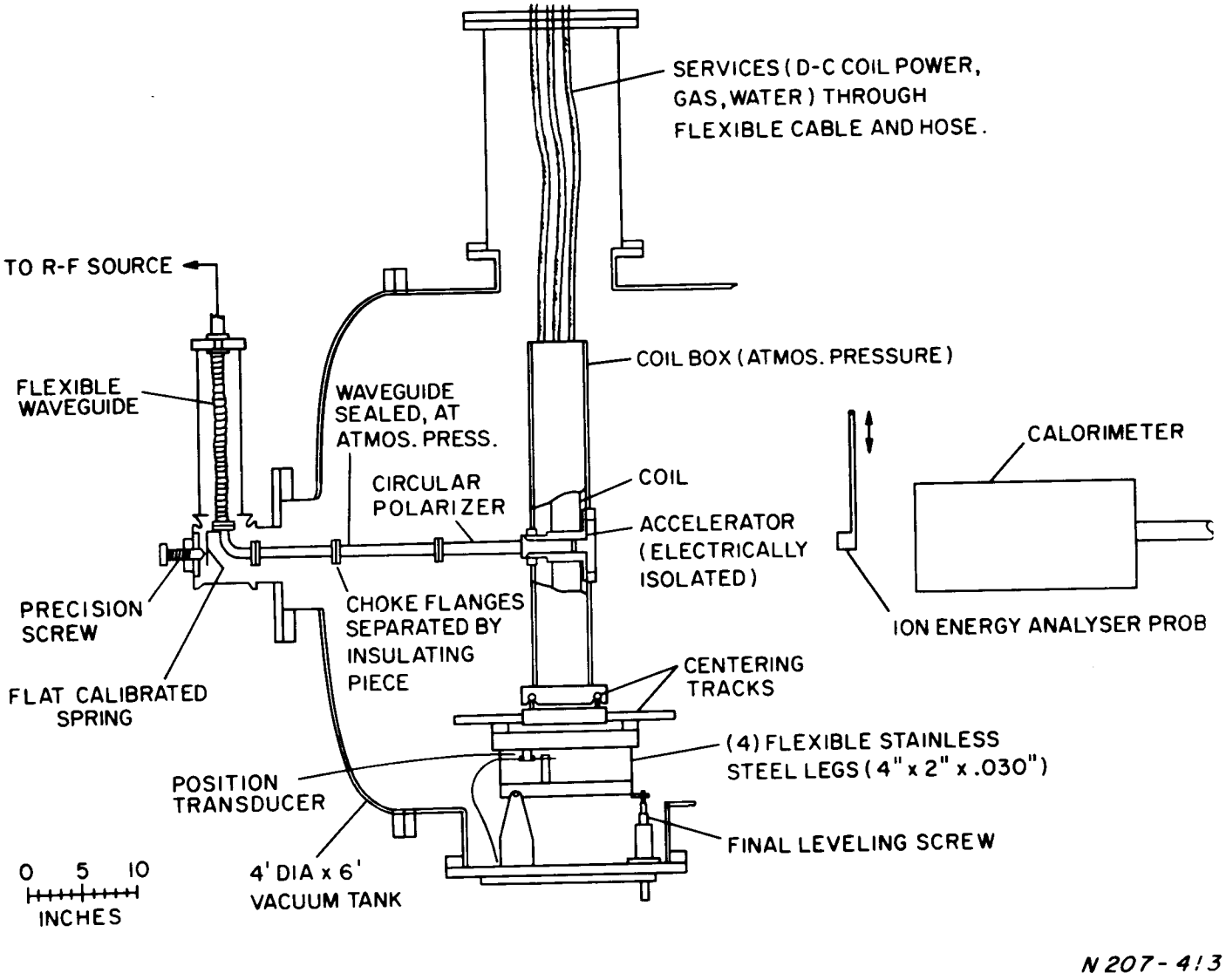

Figure 4.1.1 Mark V-S Accelerator Mounted on Thrust Stand in Vacuum Tank.

TABLE 4.1.1 CALORIMETRIC EFFICIENCY MEASUREMENTS

Propellant	Mass Flow mg/sec.	Chamber Pressure mm Hg.	Input Power watt	Dist. cm	Calorimetric Efficiency
Ar	0.9	1×10^{-4}	1037	30	60.6
Ar	0.9	1×10^{-4}	498	20	53.7
Ar	0.75	8×10^{-5}	498	20	56.5
Ar	0.75	8×10^{-5}	498	20	58.0
Kr	1.8	1.8×10^{-4}	2075	20	59.8
Kr	1.5	1.6×10^{-5}	1500	20	60.6
Kr	1.8	1.8×10^{-4}	1500	20	67
Kr	1.8	1.8×10^{-4}	1500	40	55
Kr	1.8	1.8×10^{-4}	1500	60	25

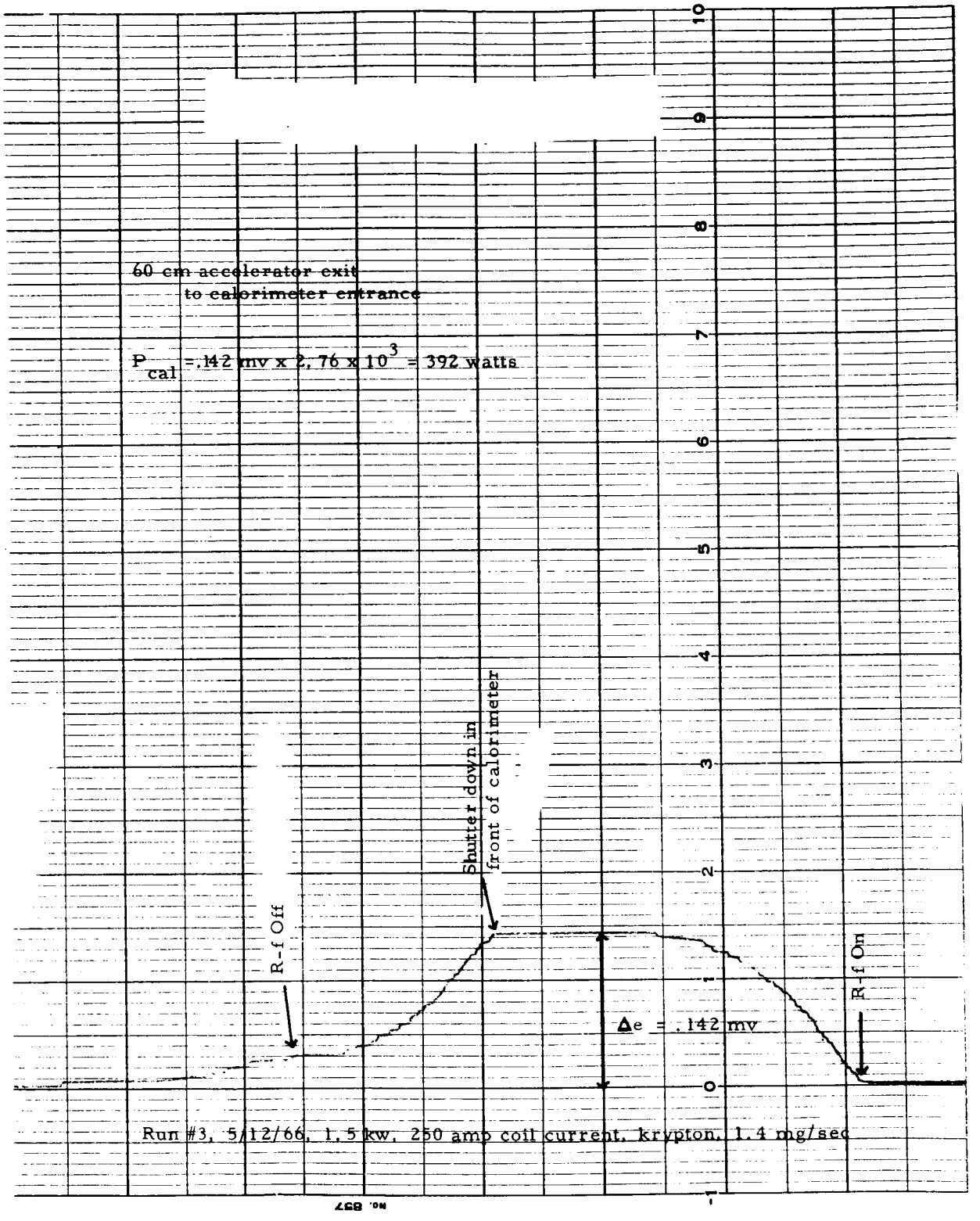

Figure 4.1.2 Calorimeter Temperature Record.

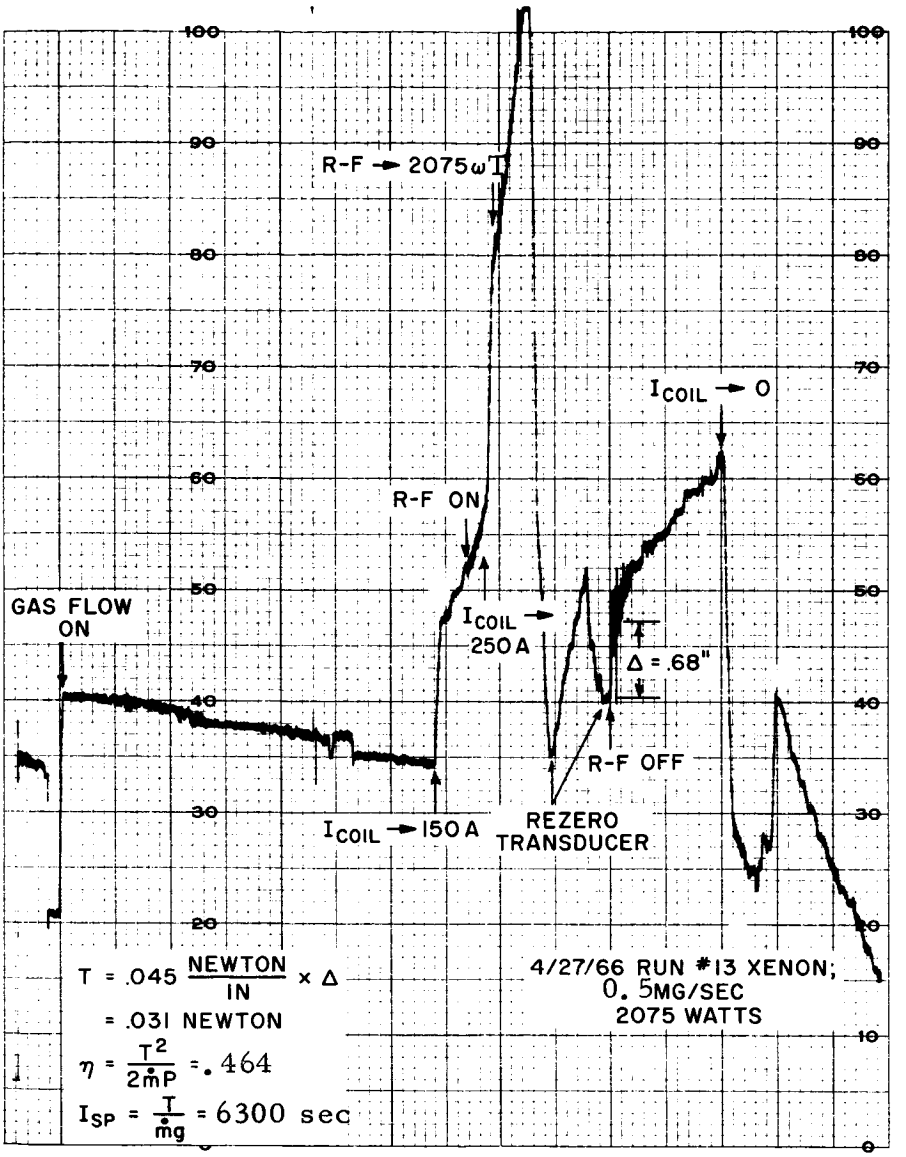

Figure 4.1.3 Typical Thrust Measurement Data Record, Mark V-S Accelerator

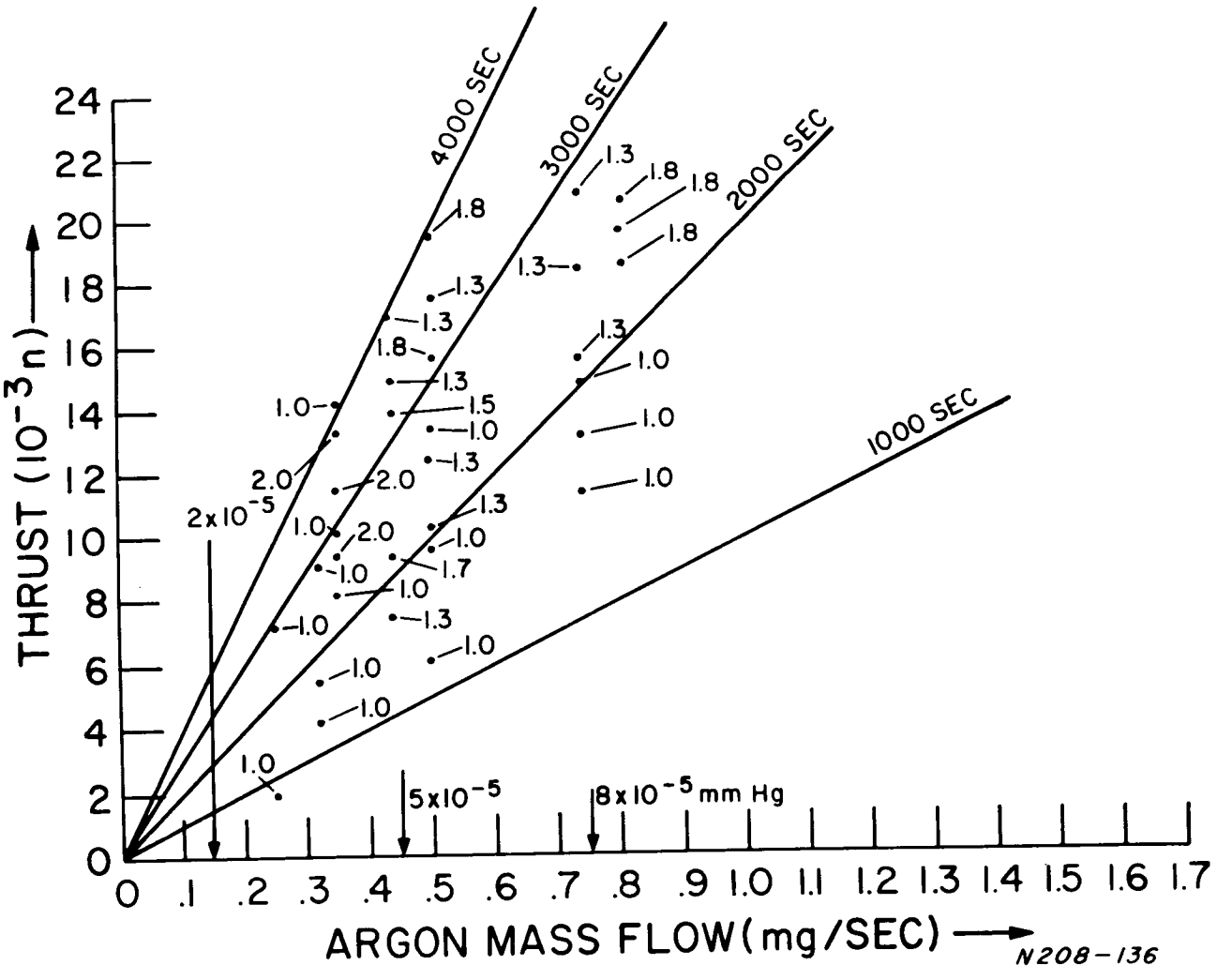

Figure 4.1.4 Thrust-Mass Flow Plot, Mark V-S Thruster, Argon.

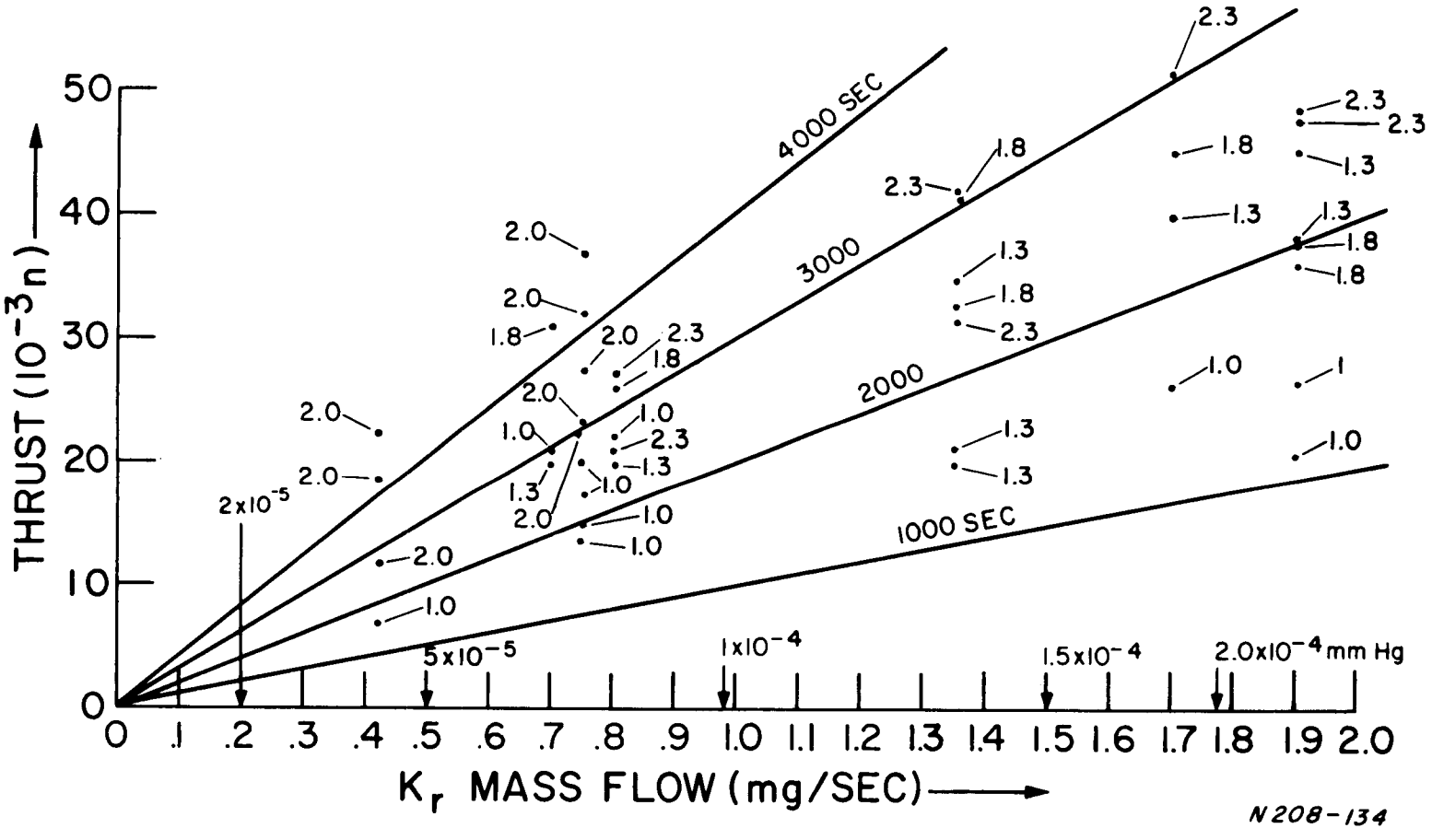

Figure 4.1.5 Thrust Mass Flow Plot from Thrust Data; Mark V-S Thruster, Krypton.

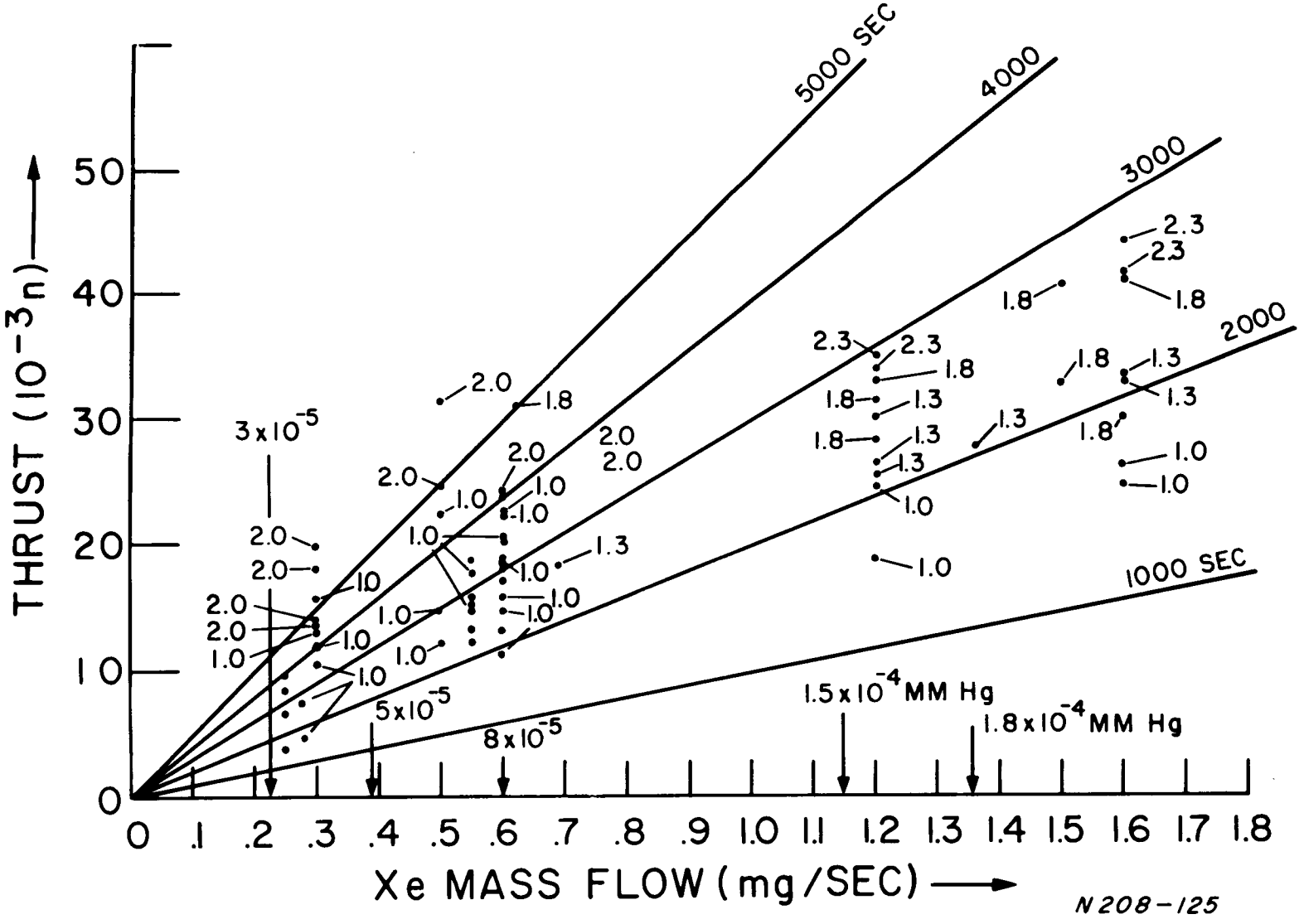

Figure 4.1.6 Thrust-Mass Flow Plot from Thrust Data; Mark V-S Thruster - Xenon.

The number located beside each point indicates the input power and the numbers above the abscissa indicate the chamber background pressure occurring for the indicated mass flow rate. Note that the major portion of the data was obtained for background pressures in the high 10^{-5} mm Hg range. Thus, entrainment effects were most likely present and evaluation of the engine performance in terms of this data is questionable since the actual accelerated mass is not known. The results of the ion energy analysis indicated in the next section yield a measure of the entrainment magnitude.

4.1.3 Simultaneous Thrust and Ion Energy Measurements

A series of experiments were run using the three gases; argon, krypton, and xenon; with two different values of flow rate for each gas. Two input powers, 1037 KW and 2075 KW, and the two magnetic field currents, 210 amp and 250 amp, were used in all combinations for each gas and flow rate. For each run, a thrust measurement, a retarding potential probe measurement, and a Langmuir probe measurement were made. The experimental arrangement was as shown in Figure 4.1.1. A complete data set required 24 runs. Each retarding potential probe trace was corrected to give the ion energy using either Langmuir probe results or utilizing the first inflection of the I-V curve since it was shown to occur at plasma potential. The derivative of the I-V curve, designated by f(V) was then used to calculate the average velocity, $\overline{v}$, and the average ion energy, $\overline{V}$, expressed in electron volts. The equations used were

$$\overline{v} = \frac{2e}{m} \int V^{1/2} f(V)\, dV / \int f(V)\, dV \qquad (4.1.1)$$

and

$$\overline{V} = \int V f(V)\, dV / \int f(V)\, dV. \qquad (4.1.2)$$

Since

$$\overline{V} = \frac{1}{2} \frac{m}{e} \overline{v^2}, \qquad (4.1.3)$$

the velocity efficiency, $(\overline{v})^2/\overline{v^2}$, was also determined and was found to be greater than 0.80 in all cases.

The retarding potential probe data were recorded on film by displaying the I-V (current-retarding potential) curves on a scope face using the circuit of Figure 3.1.2. The collector current was measured by sensing the potential drop across a 1 K ohm resistor. Maximum ion currents of up to 200 μamp were measured. The ion retarding potential was varied by turning off the power supply after it had been set at approximately 350 volts and letting the 120 μf capacitor discharge through the 12K ohm shunt resistance of the power

supply. The 45 volt bucking battery allowed the potential to be swung through zero retarding potential. A typical recorded scope trace is presented in Figure 3.1.3.

An interesting effect was observed during preliminary probe usage. The effect was the occurrence of negative current to the collector when the collector potential was sufficiently high to repell all incident ions. The negative current occurred only when the accelerator was operated at high power and high magnetic field for relatively low mass flow. When the potential difference between the collector plate and the second grid was increased by making the second grid more negative, the negative current to the collector decreased and could be reduced to zero for second grid potentials as great as -630 volts. Because the negative current decreased with increase of potential difference the effect was not leakage or secondary emission but rather could have been due to the incidence of high energy electrons with energies in the vicinity of 500 ev. It was noted that increasing the mass flow tended to decrease the occurrence of high energy electrons.

The I-V curve obtained from the trace of Figure 3.1.3 is shown in Figure 4.1.7. The resulting energy distribution function is shown in Figure 4.1.8.

Cylindrical tungsten Langmuir probes were used to obtain the local plasma potential relative to ground potential. This was necessary since the first grid of the energy analyzer was tied to ground and the plasma potential was typically 20 to 30 volts above ground potential. Thus, the ions acquired additional energy upon passing from the plasma into the probe. The true ion energy was obtained, therefore, by subtracting the measured plasma potential from the retarding potential of the energy analyzer. The measured plasma potential is indicated in Figure 4.1.7 and the true ion energy is indicated on the upper scale. The ion current in Figure 4.1.7 for retarding potential less than the plasma potential was composed of the ions having directed kinetic energy plus background plasma ions which were accelerated from the plasma potential to the probe.

The standard means of obtaining a Langmuir probe oscillogram was to bias the probe negatively relative to ground potential by increasing the power supply voltage to 250 volts (see the probe circuit of Figure 2.1.4). The power supply was then shut off allowing the 280 μf capacitor to discharge sweeping the probe from -83 to 167 volts.

The Langmuir probe traces are shown as the upper curves of Figure 3.1.3 where one signal was chopped between two scope inputs enabling recording at two different gains for the purpose of examining the electron retardation region in more detail.

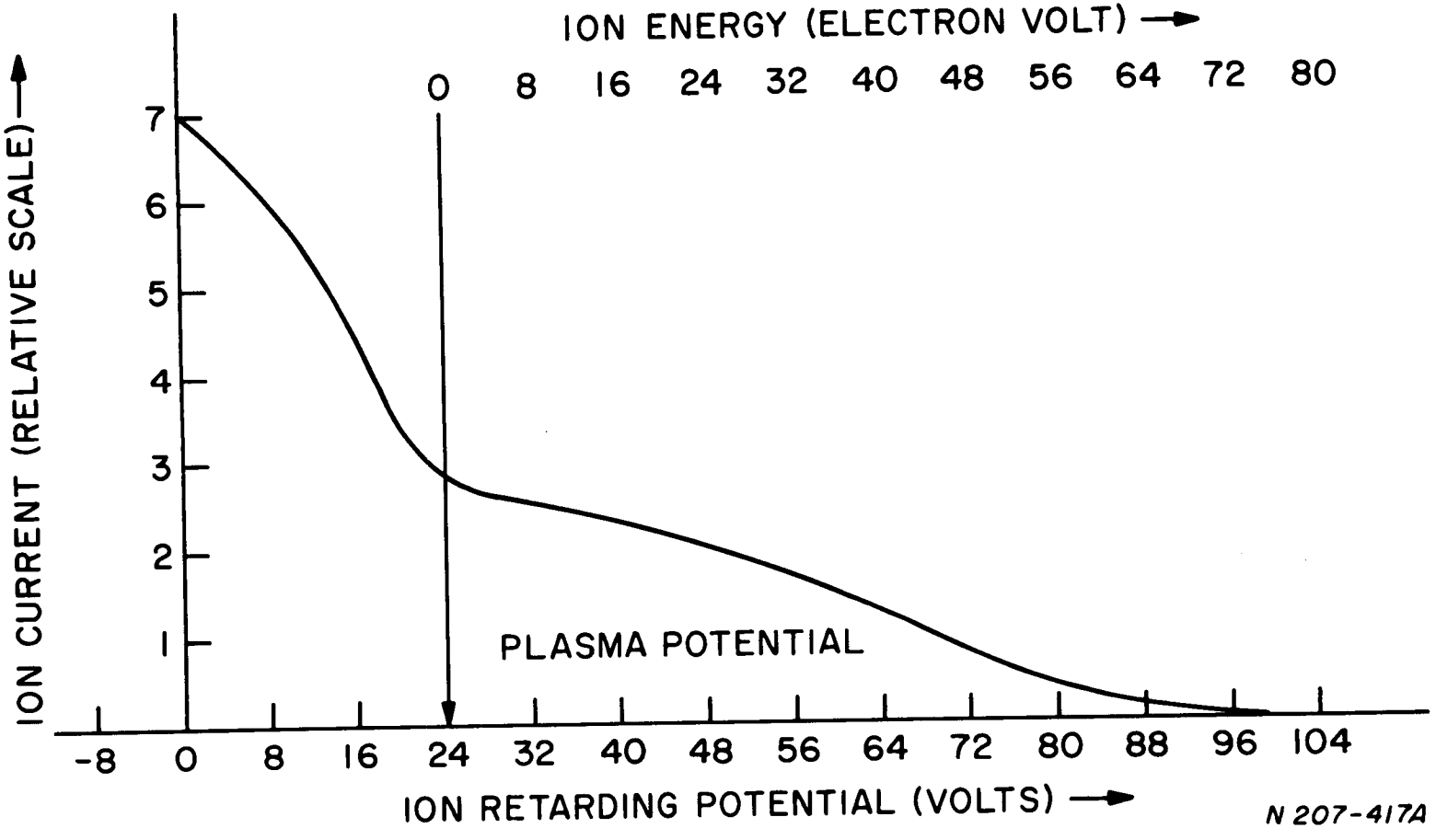

Figure 4.1.7 I-V Curve Obtained From Trace of Figure 3.1.3

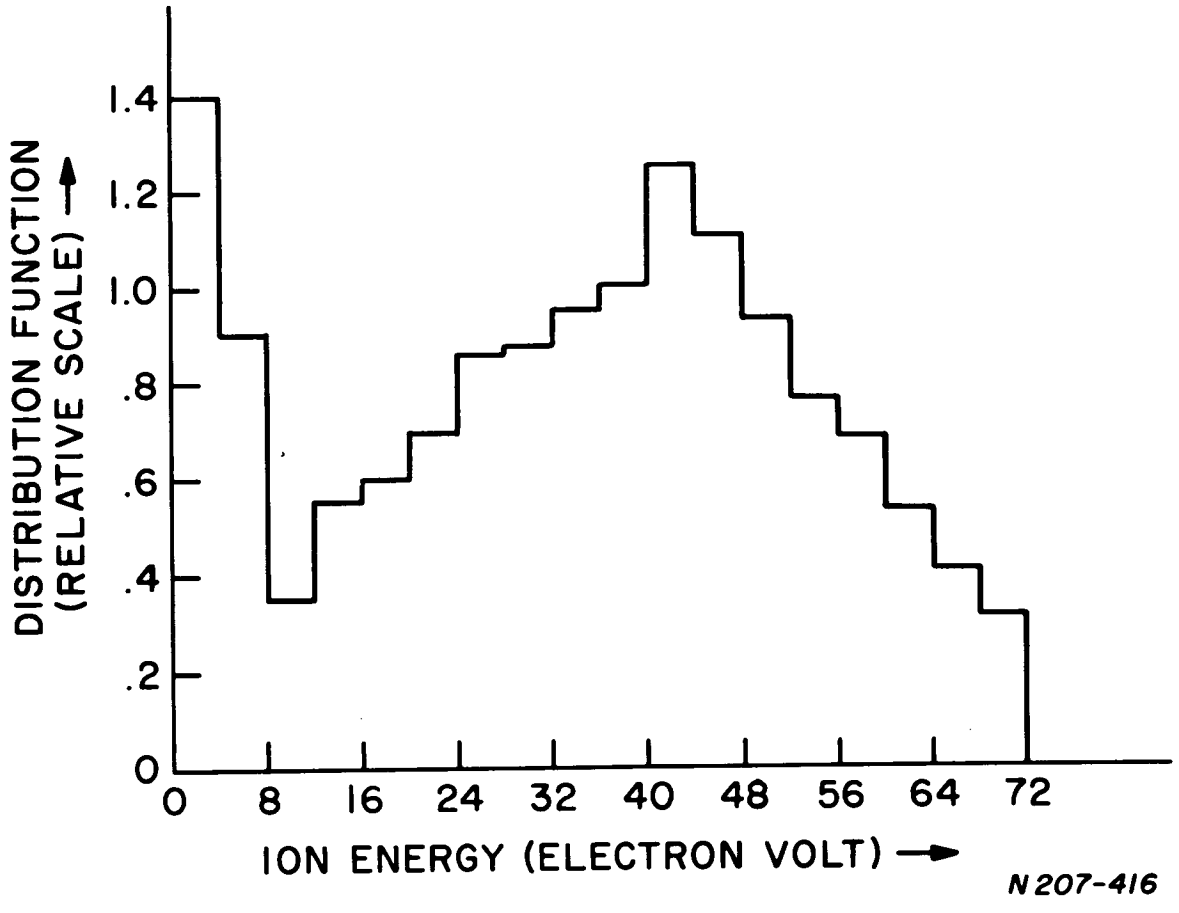

Figure 4.1.8 Energy Distribution Function Obtained by Differentiating the I-V Curve of Figure 3.1.3.

Plasma potentials were estimated from inspection of the plot of $\ln j_e$ vs. probe potential. Using this estimate, the accelerating field electron collection region of the probe trace was processed. Unfortunately, the plasma conditions of the present experiment ($n_e \sim 10^{10}$ cm^{-3}, 3×10^4 °K $\leq T_e \leq 6 \times 10^4$ °K) dictated that the accelerating field electron current to the probe was limited by a combination of orbital loss and space charge effects. Thus, the probe theory was relatively complex[5]. In most cases, however, it was possible to fit cylindrical Langmuir probe theory to the data in the accelerating field electron collection region, thus enabling the locating of the plasma potential to within a probable error of $\pm$ 0.5 volt.

It was noted after a number of Langmuir probe traces were analyzed that the determined value of the plasma potential coincided with the first inflection of the I-V trace of retarding potential probe as can be observed in Figure 3.1.3. Thus, for later data, the Langmuir probe traces were not analyzed and the plasma potential was located by the first inflection of the I-V curve to within $\pm$ 4 volts.

The results are shown in Table 4.1.2 and Figure 4.1.9. The table shows the values of specific impulse determined by the thrust measurement and the ion energy measurement. Generally, the energy analysis determined value was less than the thrust determined value with best agreement occurring at low magnetic field and power. Also compared in the table is the metered input mass flow and the average accelerated mass flow as inferred from the energy analysis results, i.e., the value of $F/\overline{v}$ where F is the measured thrust and $\overline{v}$ the average ion velocity as determined from the energy analysis. This time, the metered mass flow value was the lower with best agreement occurring again at low field and low power.

Figure 4.1.9 compares in graphic form the values of specific impulse using the measured thrust and the metered input mass flow with the specific impulse values determined from the ion energy analysis. It is seen that for the low power, low magnetic field points the thrust determined values were between 2 and 4 times the retarding potential determined values. For the high power, high magnetic field case the ratio was as large as 10 for xenon, about 6 for krypton, and about 4 for argon. For either power value, the point with the higher magnetic field value consistently yielded the higher ratio. This result strongly suggests entrainment since at higher magnetic field values the resonance position was moved forward relative to its position at lower field values thus allowing a greater number of background neutrals to diffuse into the accelerating region where they are ionized either by electron impact or charge exchange and contribute to the thrust.

4.1.4 Thrust Measurements - Ar, Kr - Externally Mounted Thrust Stand

The strong evidence for the occurance of entrainment using inert

TABLE 4.1.2

Results of retarding potential probe measurements and thrust measurements obtained simultaneously.

Gas	$\dot{m}$ mg/sec.	P_o KW	I_B amp	F mn	$F/\dot{m}g$ sec	$\bar{V}$ volt	$\bar{v}/g$ sec	η_v	$F/\bar{v}$ mg/sec	$F/\bar{v}\dot{m}$
Kr	0.75	1.037	210	13.5	2100	20.3	606	.81	2.27	3.5
Kr	0.75	1.037	250	17.2	2700	23.1	669	.87	2.63	4.0
Kr	0.75	2.075	210	22.1	3480	37.5	854	.88	2.64	4.0
Kr	0.75	2.075	250	32.0	5000	34.1	808	.96	4.03	6.2
Xe	0.30	1.037	210	10.3	3520	39.7	788	1.0	1.34	4.5
Xe	0.30	1.037	250	11.7	4000	35.6	682	.87	1.72	5.7
Xe	0.30	2.075	210	13.5	4590	22.5	639	.84	2.23	7.4
Xe	0.30	2.075	250	18.0	6120	31.8	544	.85	3.38	11.3
Xe	0.50	1.037	210	12.05	2460	21.9	543	.88	2.36	4.7
Xe	0.50	1.037	250	22.5	4600	31.1	645	.87	3.56	7.1
Xe	0.50	2.075	210	24.7	5070	49.6	818	.88	3.09	6.2
Xe	0.50	2.075	250	31.5	6450	37.9	677	.79	4.74	9.5
A	0.35	1.037	210	8.9	2600	42.6	1351	.86	.67	1.9
A	0.35	1.037	250	14.1	4100	35.2	1232	.88	1.16	3.3
A	0.35	2.075	210	8.9	2600	50.7	1519	.91	.60	1.7
A	0.35	1.037	210	11.3	3280	45.3	1415	.88	.81	2.3
A	0.5	1.037	210	9.4	1910	39.4	1142	.88	.85	1.7
A	0.5	1.037	250	19.3	3940	27.6	1119	.96	1.77	3.5
A	0.5	2.075	210	18.8	3840	41.6	1360	.89	1.41	2.8
A	0.5	2.075	250	21.6	4410	36.4	1241	.85	1.77	3.5

Notation for Table I

$\dot{m}$ = metered input mass flow, mg/sec.

P_o = input microwave power

I_B = coil current, amp

F = measured thrust, millinewtons

$F/\dot{m}g$ = specific impulse, sec, thrust and mass flow determined value

$\bar{V}$ = average ion energy, electron volts

$\bar{v}/g$ = average specific impulse, sec, retarding potential probe determined value

η_v = velocity efficiency

$F/\bar{v}$ = average accelerated mass flow, mg/sec

$F/\bar{v}\dot{m}$ = ratio of accelerated mass to input mass

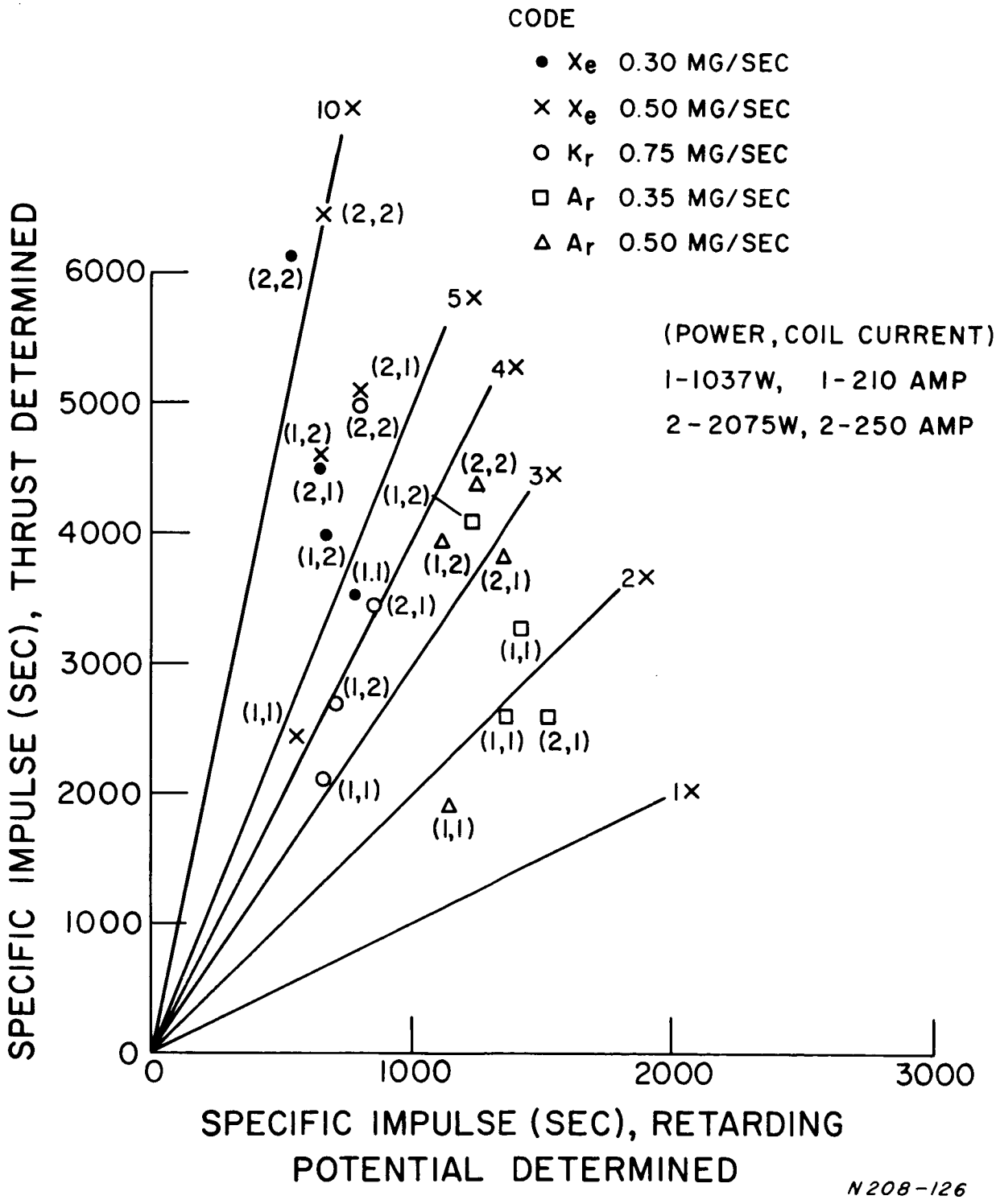

Figure 4.1.9 Comparison of Thrust Determined and Retarding Potential Determined Values of Specific Impulse.

gases suggested the use of a propellant capable of being cryogenically pumped. In order to minimize the technical problems involved in modifying the engine, mercury was chosen over the alkali metals because of its relatively low vaporization temperature. In addition, to simplify the system the engine was mounted on a vacuum port cover with the external surfaces of the engine outside of the vacuum thus exposing feed and coolant line connections. This arrangement also simplified the calibration and adjustment procedures associated with the thrust stand since it too was located external to the vacuum chamber.

The coil was mounted directly on the thrust stand with no mechanical connection existing between the engine and the coil. Thrust resulting from the magnetic interaction between the plasma and the coil was measured but any component resulting from purely thermodynamic or aerodynamic effects was not included in the measurement.

A further improvement was the design of a new engine having the same internal dimensions as the Mark V-S engine but having additional cooling capacity, thus permitting longer operating periods without overheating of the window. The new engine, designated Mark VA-S, had a larger external dimension than the earlier version. Thus, a new coil having a 5 inch I. D. was required. The resulting experimental arrangement was shown in Figure 3.2.1.

In order to check out the new system, thrust measurements were made using argon and krypton. The results of these measurements are given in Figures 4.1.10 and 4.1.11.

Comparing these results with those obtained with the internally mounted thrust stand and the Mark V-S engine, Figures 4.1.4 and 4.1.5, it is seen for argon that the agreement is good for low mass flow, but for mass flow values above approximately 0.3 mg/sec. the earlier tests yielded higher thrust values. The same conclusions may be inferred from the krypton data although the data points are not directly comparable as is the case for the argon data.

This difference in thrust level for the two engines may possibly be explained in terms of outgassing of the Mark V-S engine because of insufficient water cooling. This explanation was suggested by an incident which occurred during initial testing of the Mark VA-S engine. The engine was originally mounted using a nylon insulating flang having an I. D. small enough that it was either heated directly by the r-f or by the presence of the hot plasma. In any case, some of the nylon was vaporized and subsequently condensed over the interior of the engine. The insulating flange was then replaced with one appropriately modified so as to avoid its being heated. When the engine was first run after the replacement, the engine performance was found to have markedly increased. The good performance continuing for the first day and for the first half of the second day. The performance dropped during

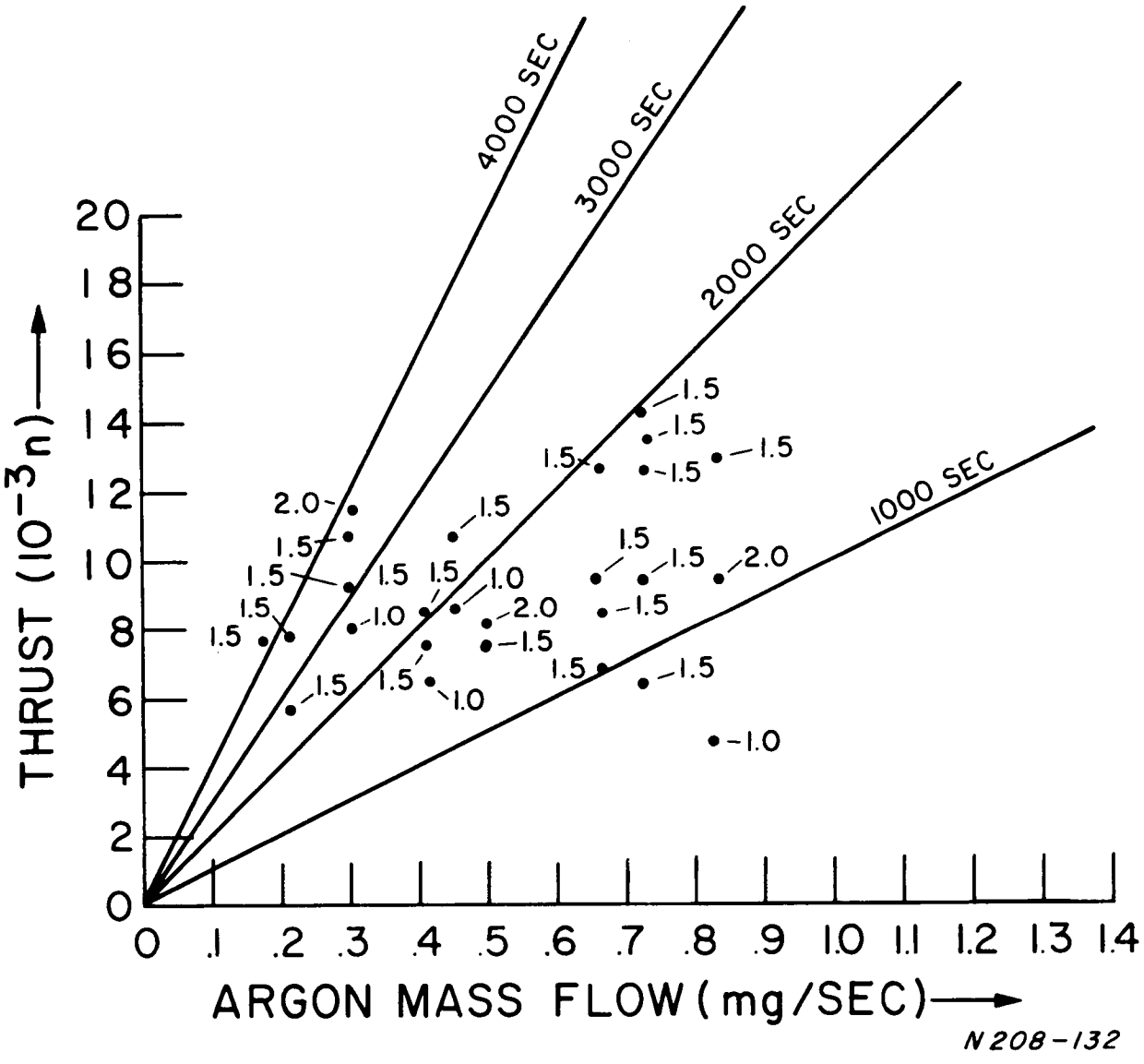

Figure 4.1.10 Thrust - Mass Flow Plot, Mark VA-S Thruster, Argon.

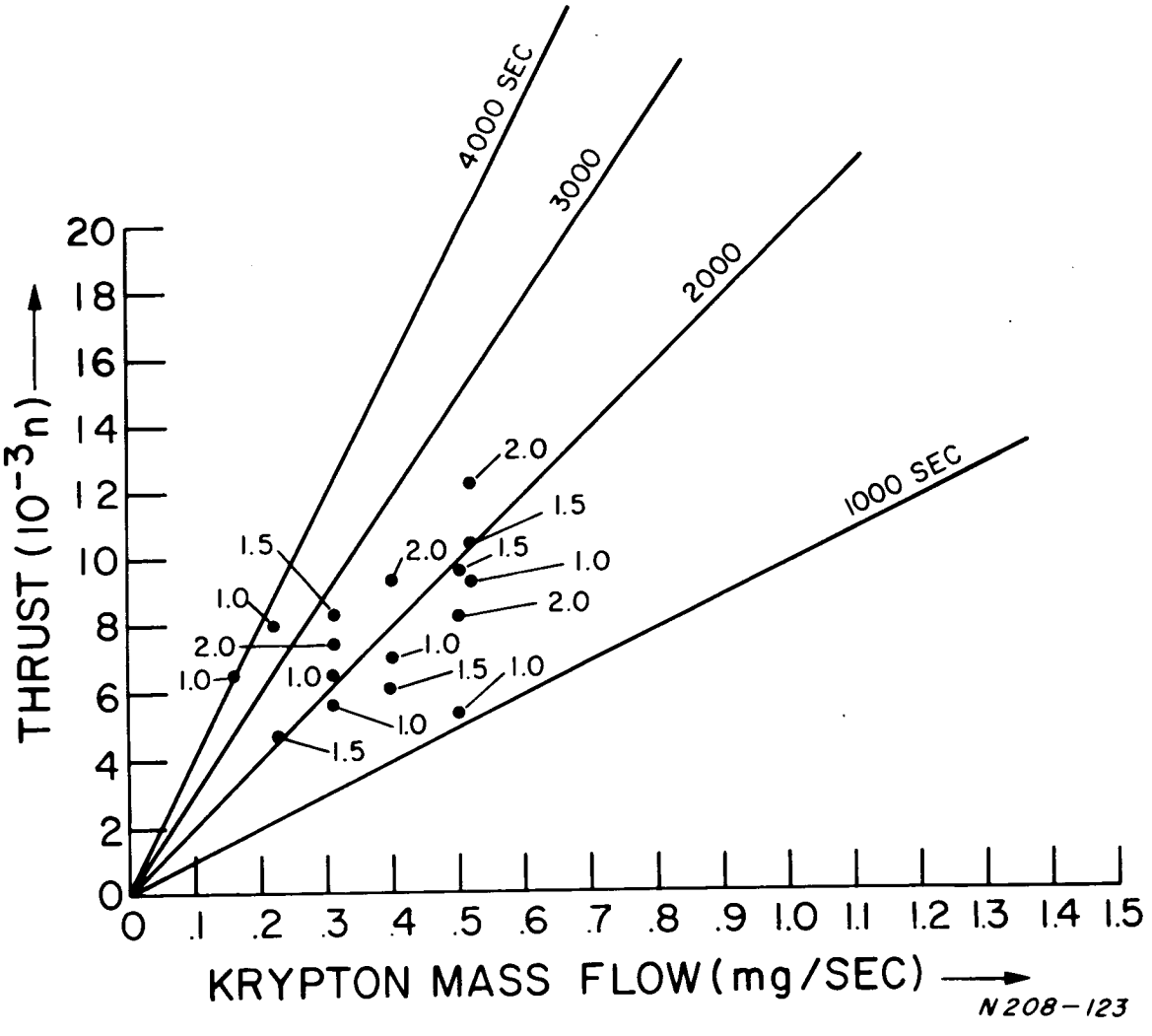

Figure 4.1.11 Thrust-Mass Flow Plot, Mark VA-S Thruster, Krypton.

the remainder of the second day. On the third day the performance had dropped to that indicated in Figure 4.1.10 and remained at that level during the following two months. A wide range of magnetic field strengths was explored and the effect of the relative location of the engine and the coil was checked during that period. Nothing that was done was successful in increasing the engine performance. It was concluded that the initial good performance was probably due to the outgassing of the engine which continued for about 10 hours of operation and that when the outgassing terminated the engine performance dropped to the low but reproducible level observed during later testing. It is suspected that the better performance of the Mark V-S engine was probably due to an outgassing effect since the engine, due to its inadequate cooling, was never run for sufficiently long time to be fully outgassed.

4.1.5 Potential Measurements

Using the emitting cylindrical Langmuir probe described in section 3.1.2, the on-axis plasma-potential was measured as a function of distance for the Mark V-S accelerator.

Figures 4.1.12, 4.1.13 and 4.1.14 show the results obtained for argon at flow rates of 0.70 and 0.35 mg/sec for different values of input power and magnetic field strengths. For the high power case, potential differences up to 160 volts are indicated while for low power the indicated potential difference is 80 volts.

If these measured potential differences are compared with the results of the retarding potential probe, which indicate an average ion energy of approximately 40 volts for the same engine conditions, further evidence for entrainment via charge exchange is indicated.

On the other hand, an additional possibility cannot be ignored. It is that multiple ionization may have occurred and the average ion energy of 40 volts corresponds to 80 volts if the ion is doubly ionized and corresponds to 160 volts if quadruply ionized. This possibility would bring the two potential measurements into agreement, although it would not exclude the possibility of entrainment via non-charge exchange processes and thus would not contradict the evidence for entrainment obtained from the simultaneous thrust and ion energy measurements.

4.1.6 Thrust Measurements - Mercury

The results of the thrust measurements using mercury are presented in Figures 4.1.15 and 4.1.16. The experimental arrangement used was the externally mounted thrust stand with the Mark VA-S engine mounted directly on the port cover of the vacuum chamber. The mercury feed system was a

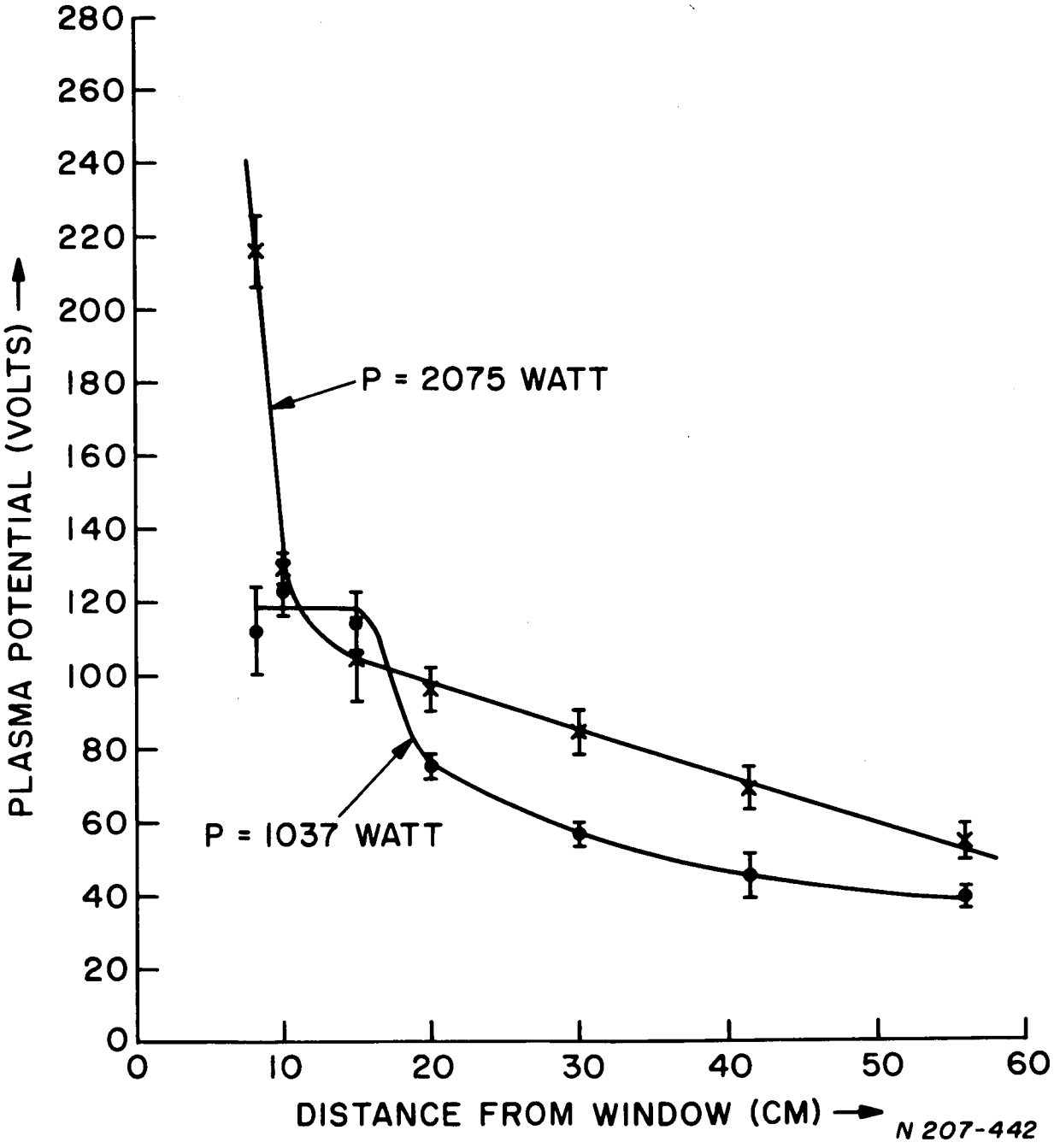

Figure 4.1.12 Axial Plasma Potential vs. Distance from Window, Imag = 250 amp, $\dot{m}$ = 0.7 mg/sec Argon.

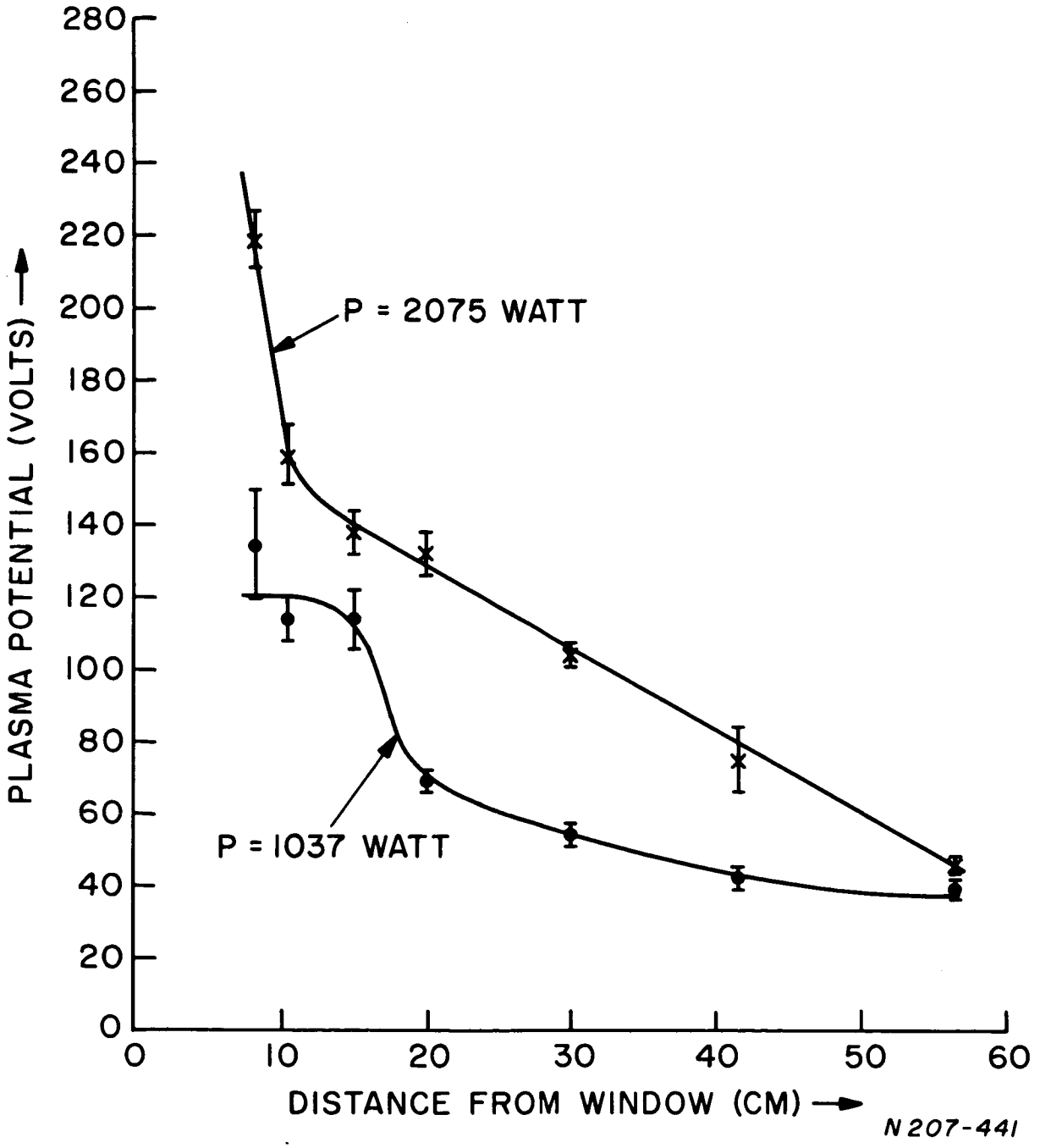

Figure 4.1.13 Axial Plasma Potential vs. Distance from Window, Imag = 210 amp, $\dot{m}$ = 0.7 mg/sec Argon.

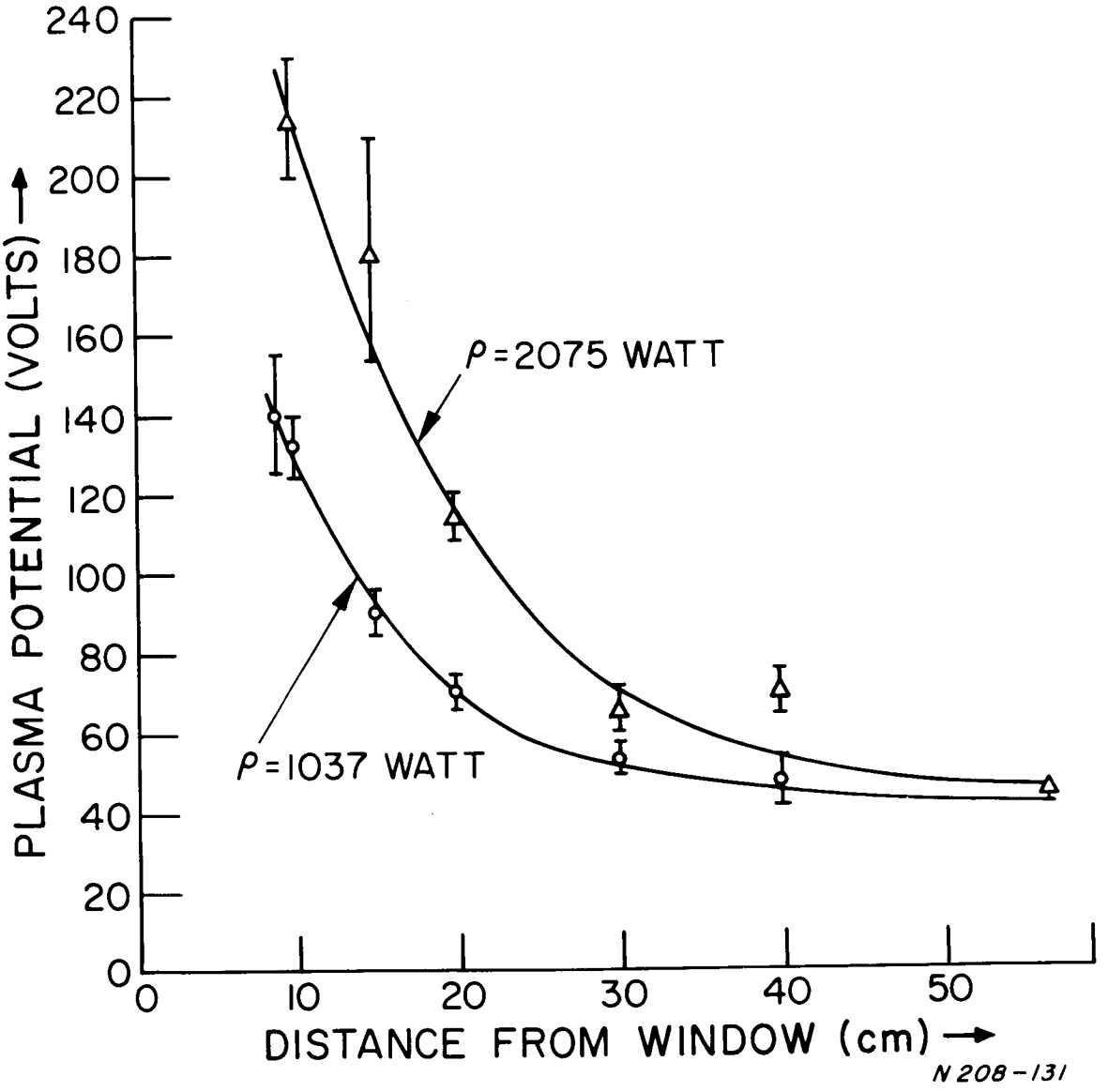

Figure 4.1.14 Axial Plasma Potential vs. Distance from Window, Imag = 210 amp, $\dot{m}$ = 0.53 mg/sec, argon.

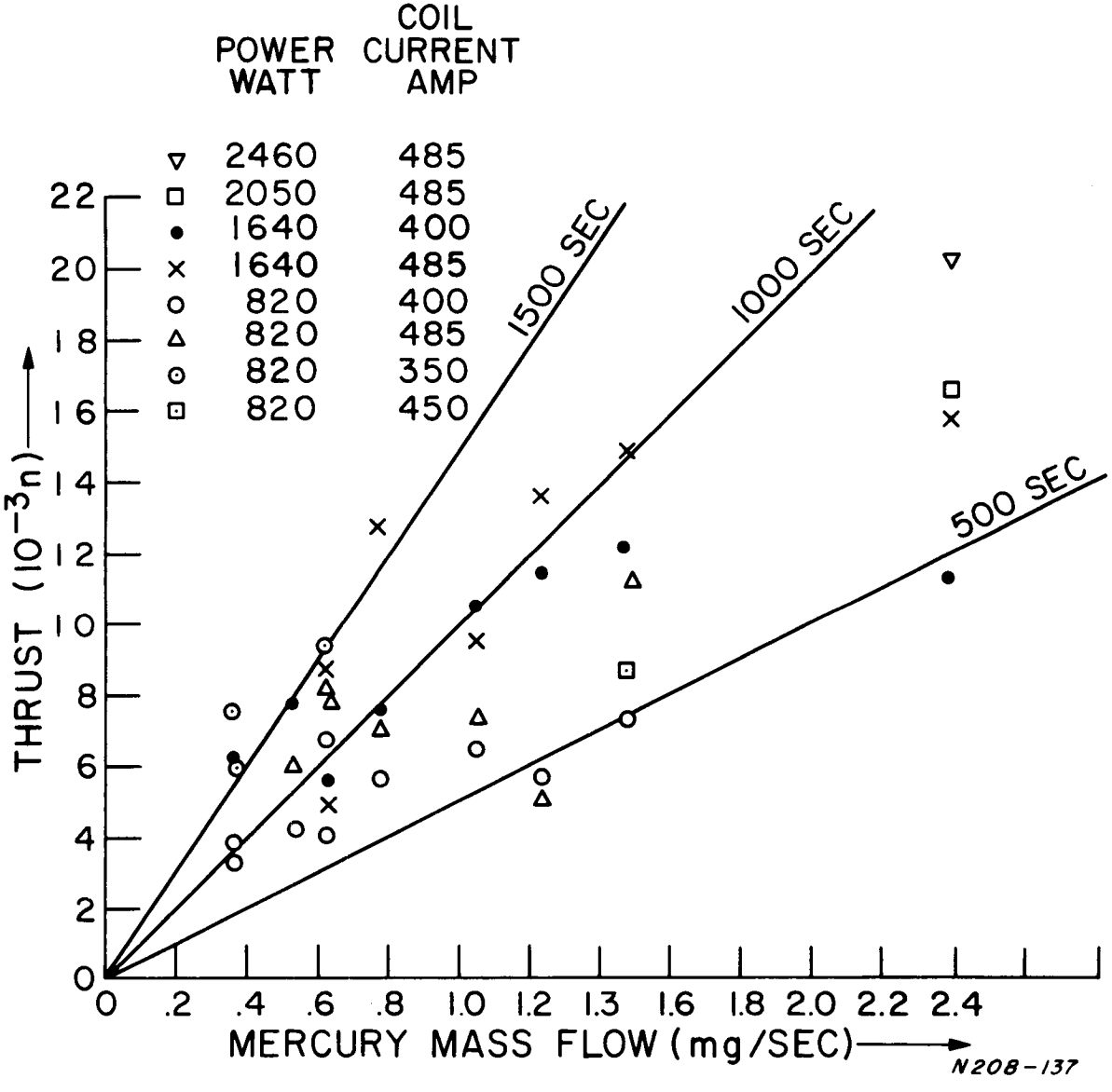

Figure 4.1.15 Thrust vs. mass flow, mercury.

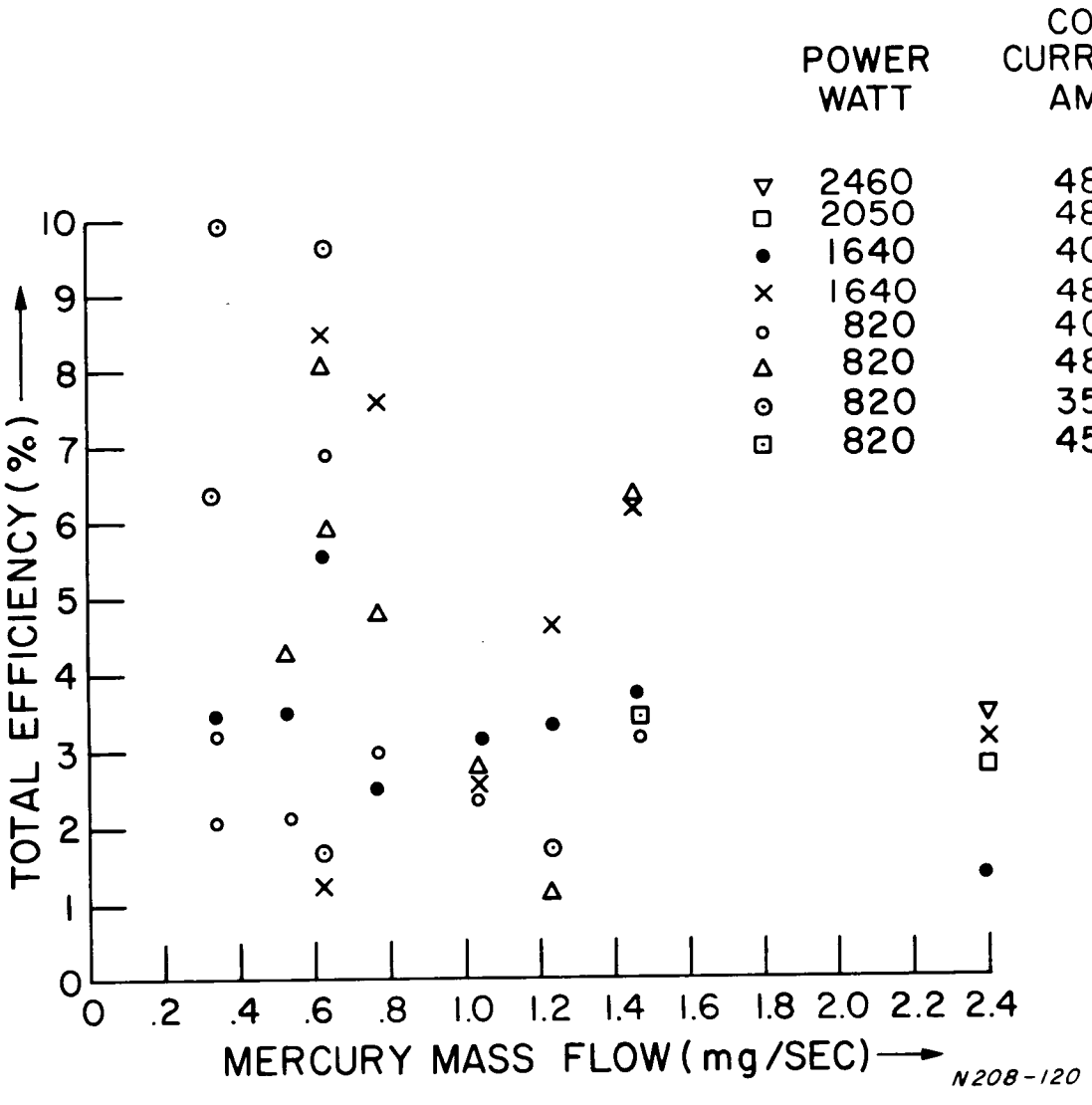

Figure 4.1.16 Total efficiency vs. mass flow, mercury

positive displacement type which is described in Section 2.1.6. The mercury vapor was cryogenically pumped by the mercury beam catcher described in Section 2.1.5. Using liquid nitrogen in both the beam catcher and the diffusion pump baffles, the background pressure, as indicated by an ionization gauge calibrated for air, was between 4.5×10^{-7} and 1.5×10^{-6} mm Hg during engine operation. The thrust stand was calibrated periodically during the testing period of each day and the calibration was found to remain constant throughout each daily testing period although slight variation in calibration occurred from day to day.

Figure 4.1.15 indicates a reduction of specific impulse with increasing mass flow rate. Also, it can be seen that for a constant flow rate the tendency was for the specific impulse to increase with increasing magnetic field and increasing input power. Figure 4.1.16 indicates that the total efficiency also decreased with increasing mass flow rate. The dependance of the efficiency on the magnetic field and the input power, however, was not clear from the data. It is clear, none-the-less, that near the lower flow rate limit (the r-f discharge could be maintained at flow rates less than approximately 0.36 mg/sec) the overall efficiency was less than 10% with the value being most probably in the neighborhood of 2 to 6%.

The computation of the efficiency values was based on the assumption that the microwave circular polarizer at the input to the engine is 100 percent efficient. In actuality it was non-ideal and only about 65% of the transmitted power was associated with the right-hand circularly polarized wave. (See Appendix B for an example of the method of determining the fraction of the power carried by either component.) The remaining 35% of the transmitted power was carried by a left hand circularly polarized component which was either reflected at the point in the plasma where the electron density had built up to the critical density, or was transmitted with little attenuation if critical density was not approached. In either case, the circular polarizer transmitted only about 65% of the power in a component that could be utilized. Thus, based on the utilizable input power rather than the total input power, all of the reported over-all efficiencies may be increased by a factor of 1.5.

4.2 PULSED PROGRAM

4.2.1 R-F Mapping

The relative electric field strength in the engine and exhaust region was mapped both in free space and in the presence of a plasma. The r-f probes previously described were employed to measure simultaneously the radial and azimuthal components of the electric field at a given point.

A typical X-Y plot is shown in Figure 4.2.1. The upper trace is the E_θ component, at 5 mv/cm, and the lower trace is the E_r component at

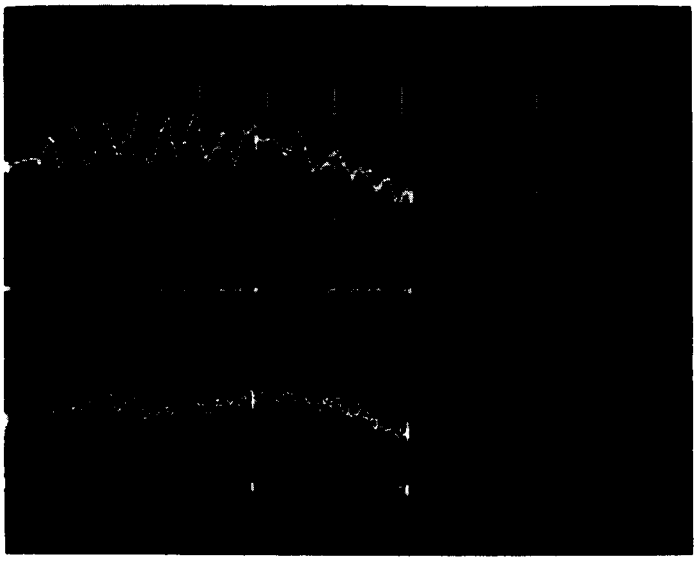

Figure 4.2.1 Typical X-Y Plot. Upper Trace E_θ = 5 mv/cm. Lower trace E_r = 2 mv/cm, θ = 225°, Horizontal Scale, R = 0.16 cm/cm.

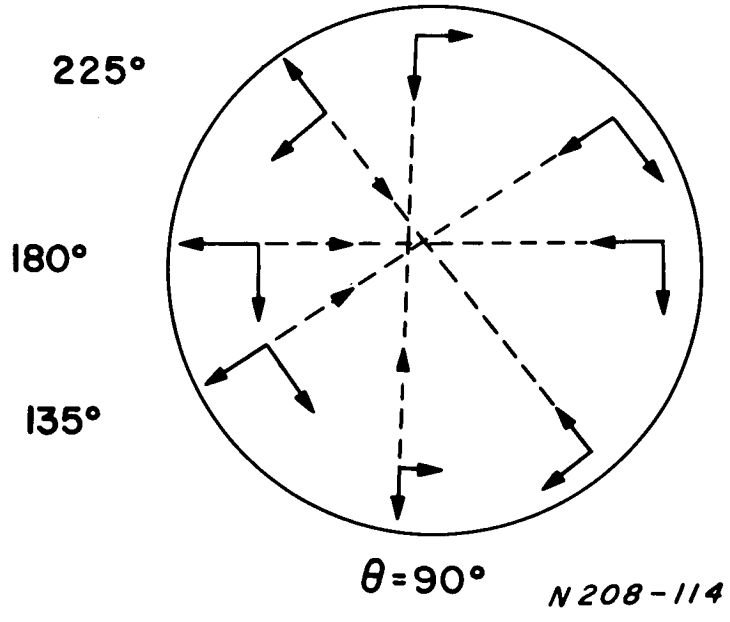

Figure 4.2.2 Diagrammed Probe Traversals of the Engine.

2 mv/cm. The other coordinates are Z = 0.5 cm and $\theta = 225^{\circ}$. The transversal of the engine is diagrammed in Figure 4.2.2. The lack of a common center is due to the mis-alignments previously described. The extreme left of the trace corresponds to the condition of the radial stub resting on the engine wall. The probe was moved along the dotted path in the direction of the arrow, simultaneously sweeping the scope trace to the right. Due to the gross dimensions of the probe (shielding and glass covering included) and the slight mis-alignment, the probe could never traverse a distance as large as the engine diameter. It was found that starting at the $\theta = 90^{\circ}$ position and moving vertically along the engine diameter gave the longest path of travel. This then became the most often used mapping path in the experiment. This was fortuitous since the maximum electric field was aligned in this direction as can be seen in the experimental results.

Data were taken inside of the engine for Z = 0 (at the window) to 4 cm, in steps of 0.5 cm, and for $\theta = 90^{\circ}$, 135°, 180° and 225°. Some typical results of one of these free space mappings are shown in Figure 4.2.3. This plot represents the relative radial component of the electric field strength vs. azimuthal position in the engine, in the plane z = 0.5 cm from the dielectric window, and at the radius r = 0.2 cm from the engine wall. The distinctive places of maximum (90° and 270°) and minimum (0° and 180°) in this plot are characteristic of an imperfect circular polarizer. A pattern of similar shape was obtained at the output of the circular polarizer. This pattern is shown in Figure 4.2.4. It is interesting to note that the pattern rotated 45° on passing thru the window. Any anisotropy in the window or its brazed joint to the engine insert could have caused rotation of the pattern. From this plot, it may be computed that a maximum of 58% of the input power goes into the right-hand or extraordinary wave (see Appendix B). All of the above measurements are free-space measurements.

Figures 4.2.6a thru k show an r-f field mapping data set in a plasma. These results are typical of the mappings that were made and specifically correspond to the following input parameters:

R-f Power Input:	3 KW, 1 millisecond pulses, 2 pulses per second
D. C. Coil Current:	450 Amps
Regulator Pressure to Pulsed Gas Valve:	6.5 lb.
Background Tank Pressure:	1.5×10^{-6} mm Hg.
Approx. Flow Rate:	0.1 milligram sec.
Gas:	Argon

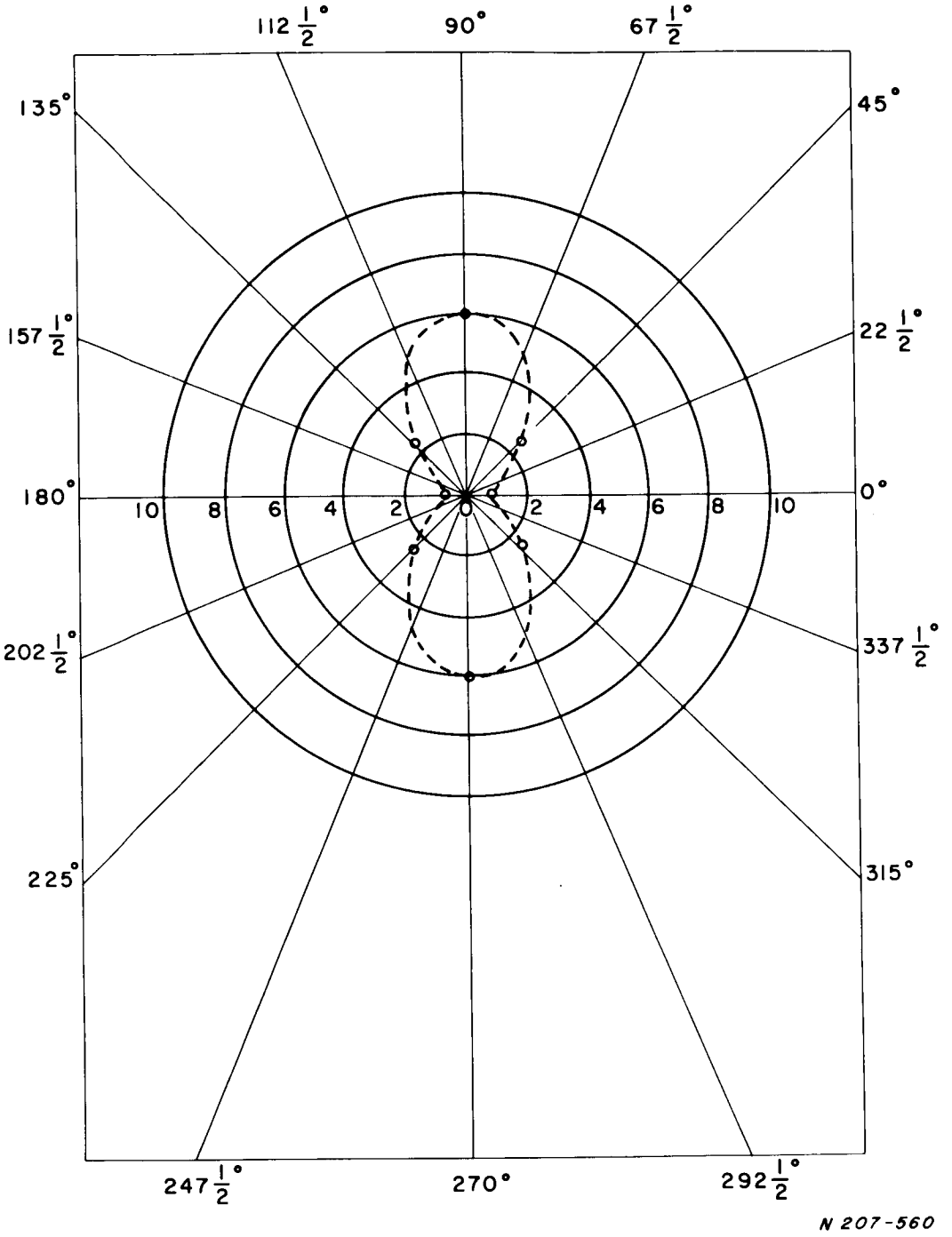

Figure 4.2.3 Radial Component of the Electric Field in the Engine.
Amplitude vs. Azimuthal Position
Z = 0.5 cm From the Window
r = 0.2 cm From the Engine Wall

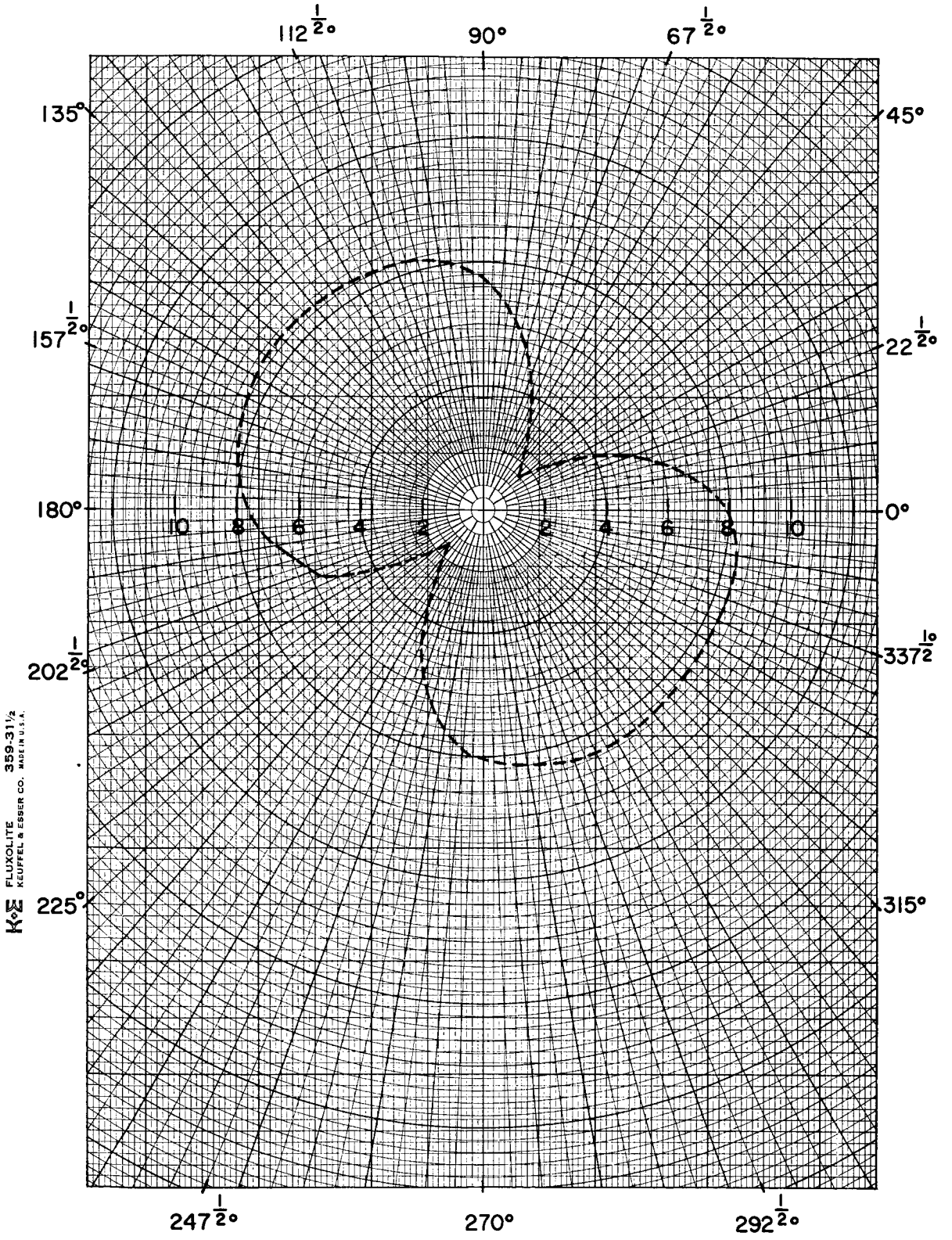

Figure 4.2.4 Output of Circular Polarizer Preceding Engine.

EXPERIMENTAL CONDITIONS

LOW FLOW R-F FIELD MAPPING

R-F = 3KW, 1MILLISEC PULSES
2 PULSES PER SEC.

I_{coil} = 450 AMPS
θ = 90°
ARGON

DEFINITION & SCALE

UPPER TRACE = E_r, RADIAL COMPONENT OF ELECTRIC FIELD

LOWER TRACE = E_θ, AZIMUTHAL COMPONENT OF ELECTRIC FIELD

HORIZONTAL SCALE

1 CM. ON TRACE = 0.16 CM VERTICALLY FROM BOTTOM OF ENGINE FOR (a) THRU (i)
= 38 CM VERTICALLY FROM BOTTOM OF ENGINE FOR (j) AND (k)

Z = 0.0 CM
$E_r = E_\theta$ = 1 VOLT / CM

Z = 0.5 CM
$E_r = E_\theta$ = 1 VOLT / CM

(a)

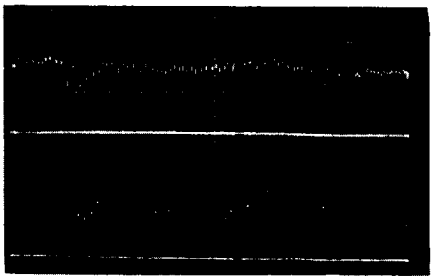

Z = 1.0 CM
$E_r = E_\theta$ = 1 VOLT / CM

(b)

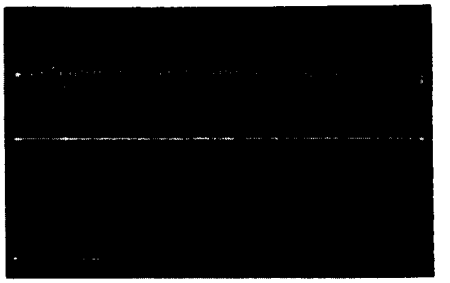

Z = 1.5 CM
$E_r = E_\theta$ = 1 VOLT / CM

(c)

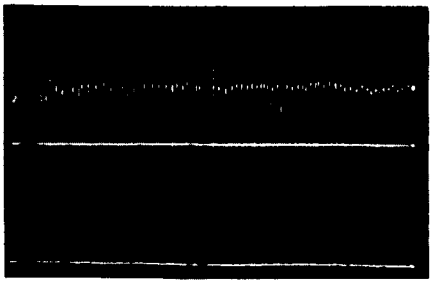

(d)

Figure 4.2.5 Low Flow R-F Field Mapping

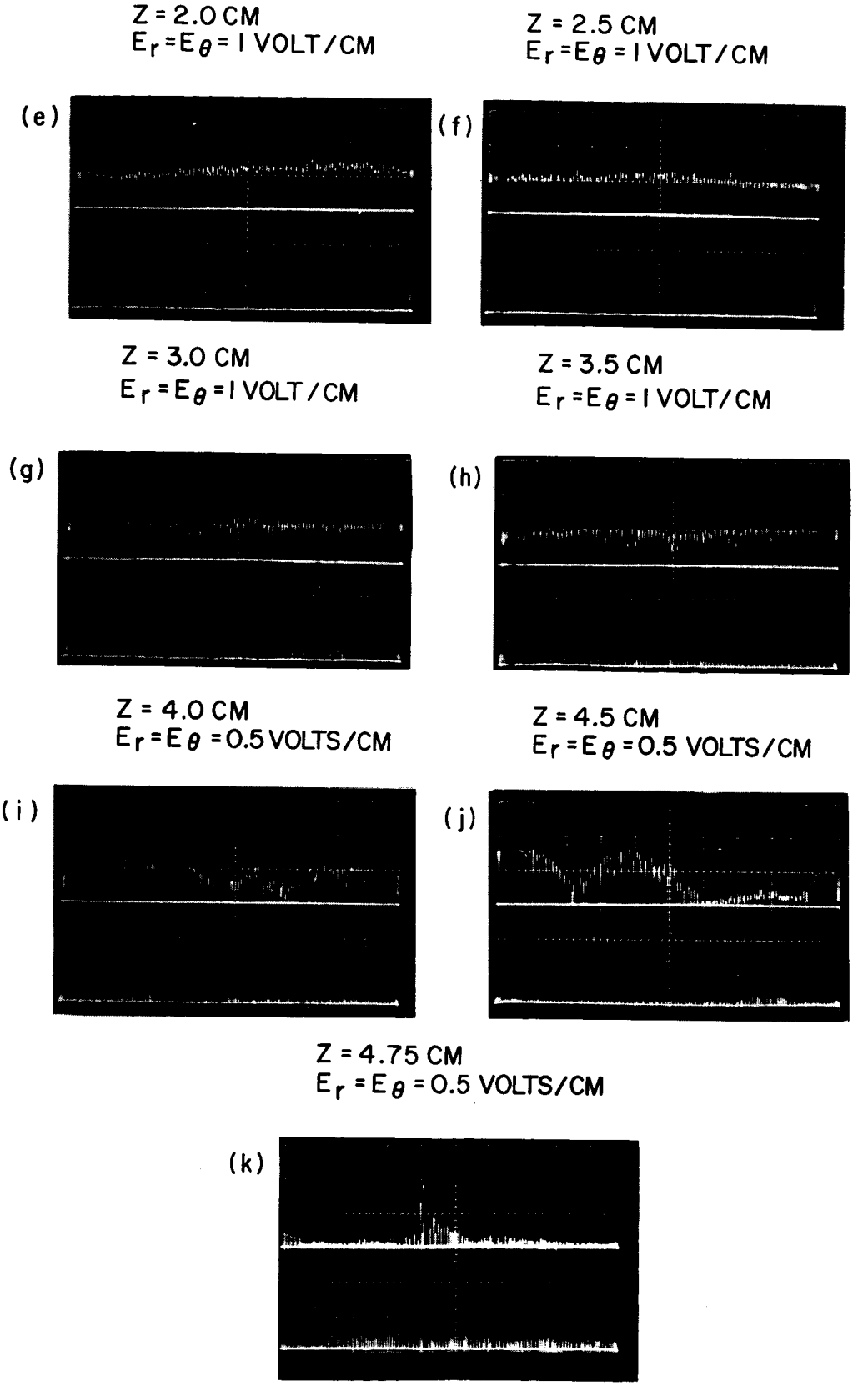

Figure 4.2.5 Low Flow R-F Field Mapping (Cont'd)

The upper trace is the radial component and the lower trace is the azimuthal component of the electric field. The ordinate is signal amplitude and the abscissa is radial position as described previously. In the presence of the plasma, the signal becomes "blurred" due to multiple sources of radiation that we shall simply term "plasma noise." In order to eliminate some of this noise in favor of the input r-f signal, a Polorad Spectrum Analyzer, Model TSA-S, with a 4.37 to 23 GHZ tuning range, was used as a frequency selective synchroscope to condition the radial component. The video output of this unit was then fed to the oscilloscope for recording. The marked difference between the filtered (upper trace) and direct inputs (lower trace) is readily seen.

Figures 4.2.5a to i show a sweep from the bottom to the top of the engine ($\theta = 90^{o}$) for a given axial distance (Z) from the dielectric window. Figures 4.2.5j and k show the vertical sweep in the engine exit plane from a distance of one engine radius below the center of the exhaust stream to about 3 cm above center. Because of their different processings, the two components should not be compared quantitatively but may well be compared qualitatively.

As sketched in Figure 4.2.6, there exists a resonant surface, determined by free space measurements of B_{res}, over which resonant absorption should occur. The experimental observation of the resonant surface is evident in Figures 4.2.5h through k. It is seen in Figures 4.2.5h and i that resonance was just beginning to occur in the center of the engine at a distance of 4 cm from the window. Figure 4.2.5j shows this very clearly on its compressed scale in which the center of the engine is located at 2-1/4 cm from the left end of the trace. In Figure 4.2.6, the depth for total absorption can be predicted from the engine boundaries. This is seen to be about 0.6 cm. Figures 4.2.5i to k show the absorption to have occurred in about 0.8 cm.

Figures 4.2.5a through k support the description that follows:

The radiation (TE_{11} Mode) is transmitted to the engine through an imperfect circular polarizer and a half wave dielectric window. The radiation causes ionization of the introduced gas as it propagates in the engine which is a simple extension of the circular waveguide. Since some energy is absorbed in producing the ionization build up, the electric field strength decreases slightly with distance from the window. Finally, the electron number density becomes large enough to totally reflect the left-hand polarized component passed by the polarizer; this occurs between 1.0 and 1.5 cm from the window. About forty percent of the total input power is lost as can be predicted from the plots of the output of the circular polarizer.

The right-hand polarized wave continues to propagate at nearly constant amplitude. It is then absorbed over the resonant surface. Furthermore,

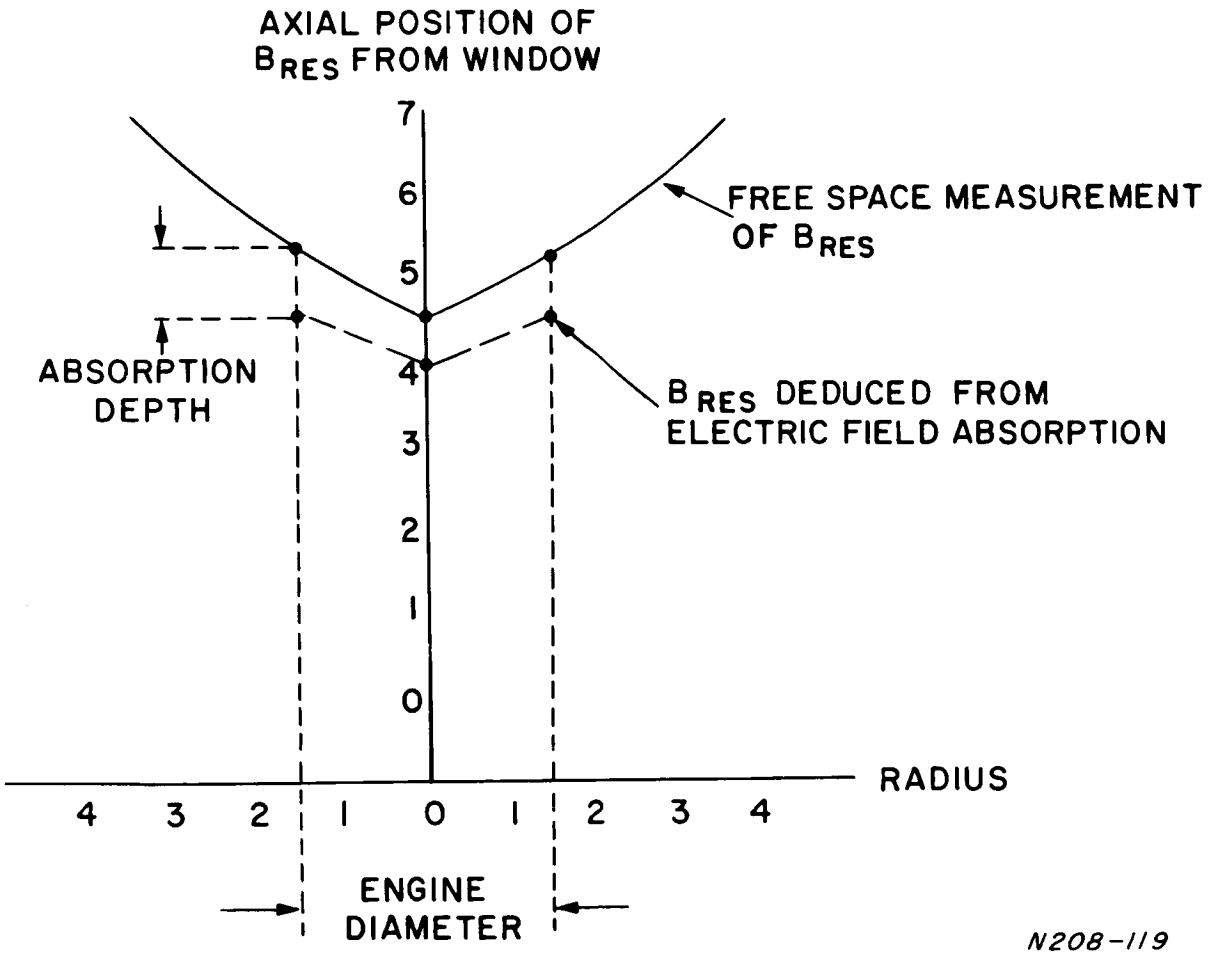

Figure 4.2.6 Axial Position of Resonant Field Strength (cm) vs. Radius From Coil Center (cm).

the radiation is seen to be confined almost completely within the plasma column, even when the plasma column exists beyond the engine exit plane. No significant r-f "leakage," therefore, is measured, and it may be concluded that the energy of the right-handed wave is efficiently transferred at resonance to the plasma.

It was seen here, as in all previously reported r-f experiments with the Cyclops, that total absorption occurred at a point in space prior to the predicted absorption point taken from the free space measurement of B_{res}[1]. In this case, the absorption was about 0.5 cm "early." An explanation of this result in terms of a thermal Doppler frequency shift with numerical results may be found in Appendix B[6]. The computed magnitude of this shift corroborated the electron temperature measurements.

4.2.2 Cold Gas Pressure Mapping and Flow Rate

Cold gas (no plasma, no magnetic field) pressure mapping was performed. The gas density probe described previously worked quite satisfactorily for this purpose. A typical gas pulse profile taken inside the engine is shown in Figure 4.2.7. The upper trace shows the SCR-triggered discharge to the valve at 500 volts/cm; the lower trace is the pressure profile at 50 mv/cm. For this large a gas pulse, the tank background pressure fluctuated from 3 to 4.4 x 10^{-5} mm Hg during the pulse. The pressure at the probe in microns may be found approximately by[4]:

$$P = (48.3V)^{1.3} \qquad (4.2.1)$$

where V is in volts. The maximum in this figure is in the micron range.

Like the r-f measurements, mappings traversing a given engine plane were made. These indicated a constant pressure in a plane at a given axial position, with the pressure decreasing with distance from the window. Figure 4.2.8 shows the peak pressure profile in the engine exit plane. Here we started from the approximate engine center and moved upward. The upper trace is again the SCR discharge at 500 volts/cm and the lower is the pressure on the Y-axis at 10 mv/cm; the X-axis is .38 cm from engine center = 1 cm on scope trace. As would be expected, the pressure dropped off with radial distance outside of the engine, but little confinement was observed in this no-plasma case.

Figure 4.2.9 shows a typical axial pressure and density mapping as a function of distance from the window. The regulator pressure for this particular run was much higher than for our normal engine-in-operation runs. The assumption of isentropic flow was made in generating the density profile from the measured pressure profile.

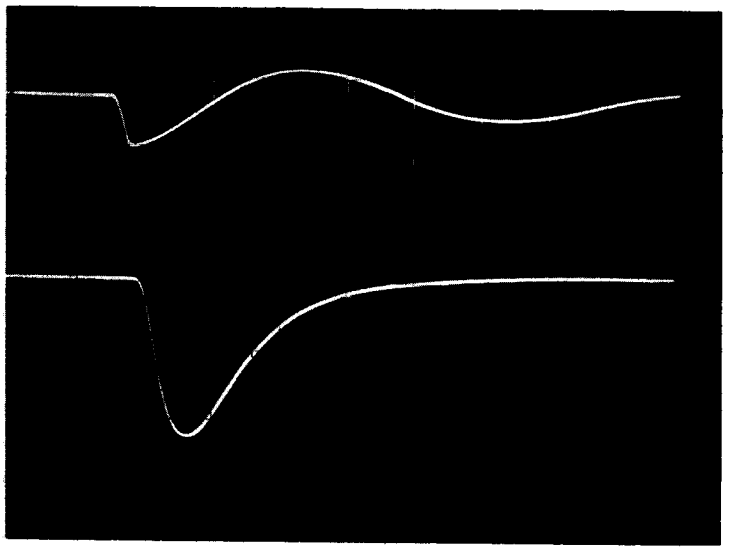

Figure 4.2.7 Upper Trace - Valve Triggering Pulse, 500 volts/cm.
Lower Trace - Pressure Profile, 50 mv/cm - Sweep 5 msec/cm

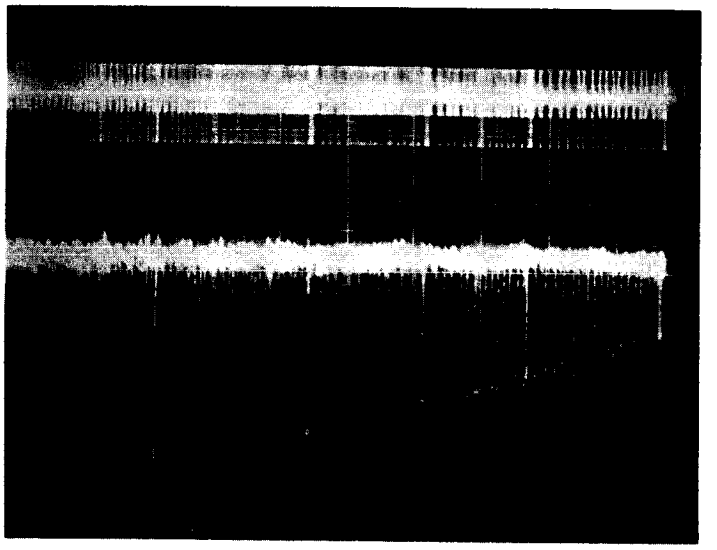

Figure 4.2.8 Upper Trace - Valve Triggering Pulse, 500 volts/cm.
Lower Trace - Pressure Profile on Engine Exit Plane X-Axis
Radial Position, .38 cm/cm.

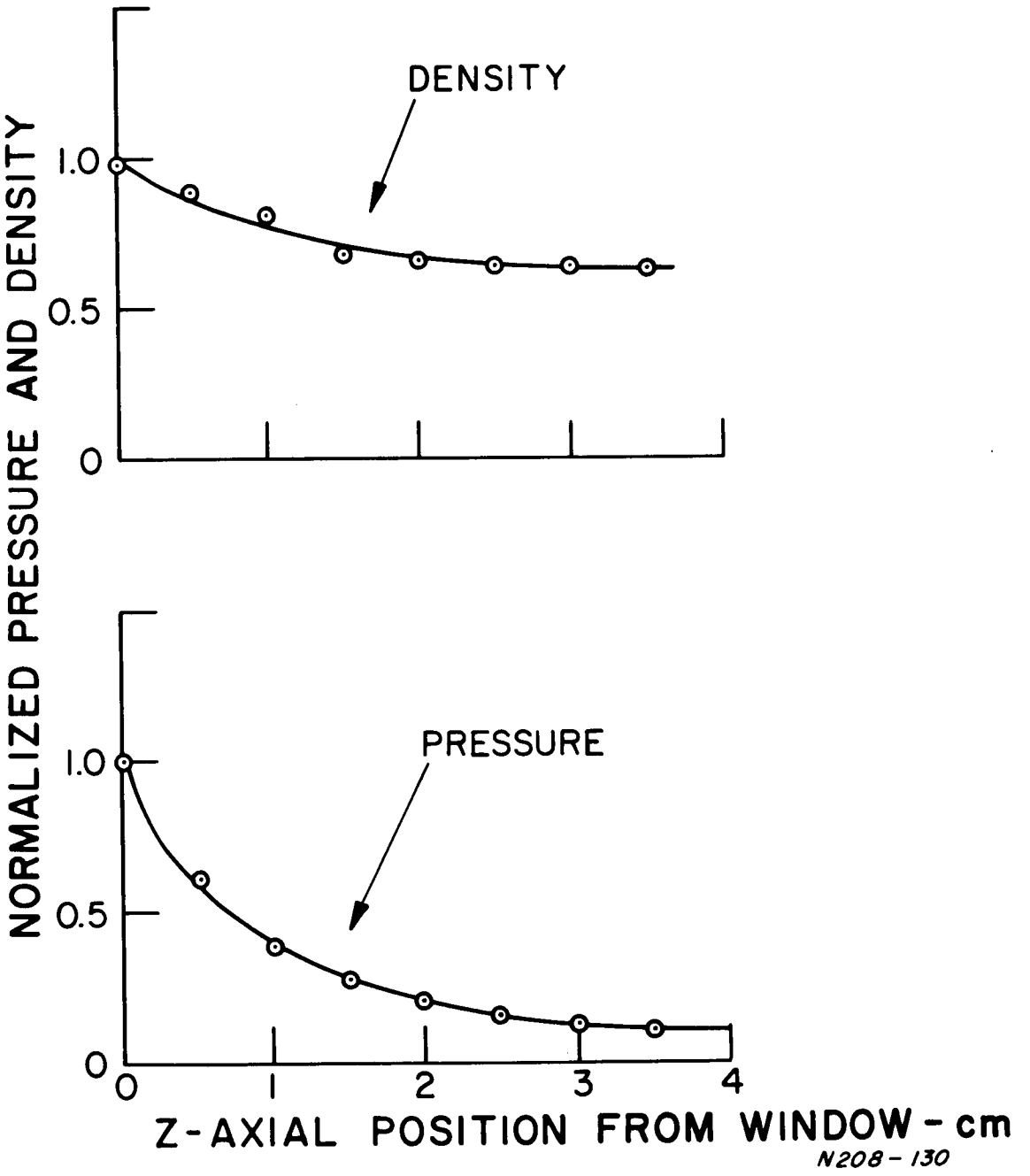

Figure 4.2.9 Pressure and Density vs. Axial Position Normalized to: 9.3 microns Hg and 2.01×10^{-8} gm/cm^3 or 3.04×10^{14} particles/cm^3.

The measurement of the propellant flow rate was determined with the diffusion pump valve closed. This removed all pumping action during a test run and allowed the tank to leak up at its pre-determined rate of 4×10^{-5} mm Hg/minute. A chosen number of gas pulses were then introduced into this closed system. The resulting final pressure was then recorded on a McCleod gauge. From this information, the mass per pulse was then calculated as follows:

$$M_p = \frac{PVM}{RTN} \qquad (4.2.2)$$

where, M_p = mass per pulse
P = corrected pressure reading,
$= P_{McCleod} - P$ leak
V = total volume of the tank and appendages
$= 2 \times 10^5$ cm^3
$R = 82$ cm^3 - ATM/K$^\circ$ - Mole
$M = 40$ gm/Mole for Argon
T = equilibrium temperature, 300°K
N = total number of pulses of gas introduced into the tank.

Many runs were made for different values of gas pressure input to the pulsed valve. Within the engine near the propellant inlet, the gas pressure measuring pentode was used to simultaneously measure the pressure vs. time profiles of the input pulse. A photo was taken at the start of each run. By using these photographs together with Equation 4.2.1, Figures 4.2.10 to 4.2.12 were plotted giving the variation of pressure with time for single pulses of different mass-per-cycle data sets. This information enabled the determination of the instantaneous propellant flow rate that occurred during an r-f pulse located in time within a gas pulse. The relationship

$$M = KP\Delta t,$$

was used, where K is a constant of proportionality, P is the absolute pressure and Δt is the time duration of the r-f pulse. The total mass per pulse is

$$M_p = K \int P \, dt; \qquad (4.2.3)$$

and is therefore proportional to the area under the pressure vs. time profile. The mass flow rate is, then,

$$\dot{M} = \frac{M}{\Delta t} = \frac{M_p}{\int P \, dt} \; P \; . \qquad (4.2.4)$$

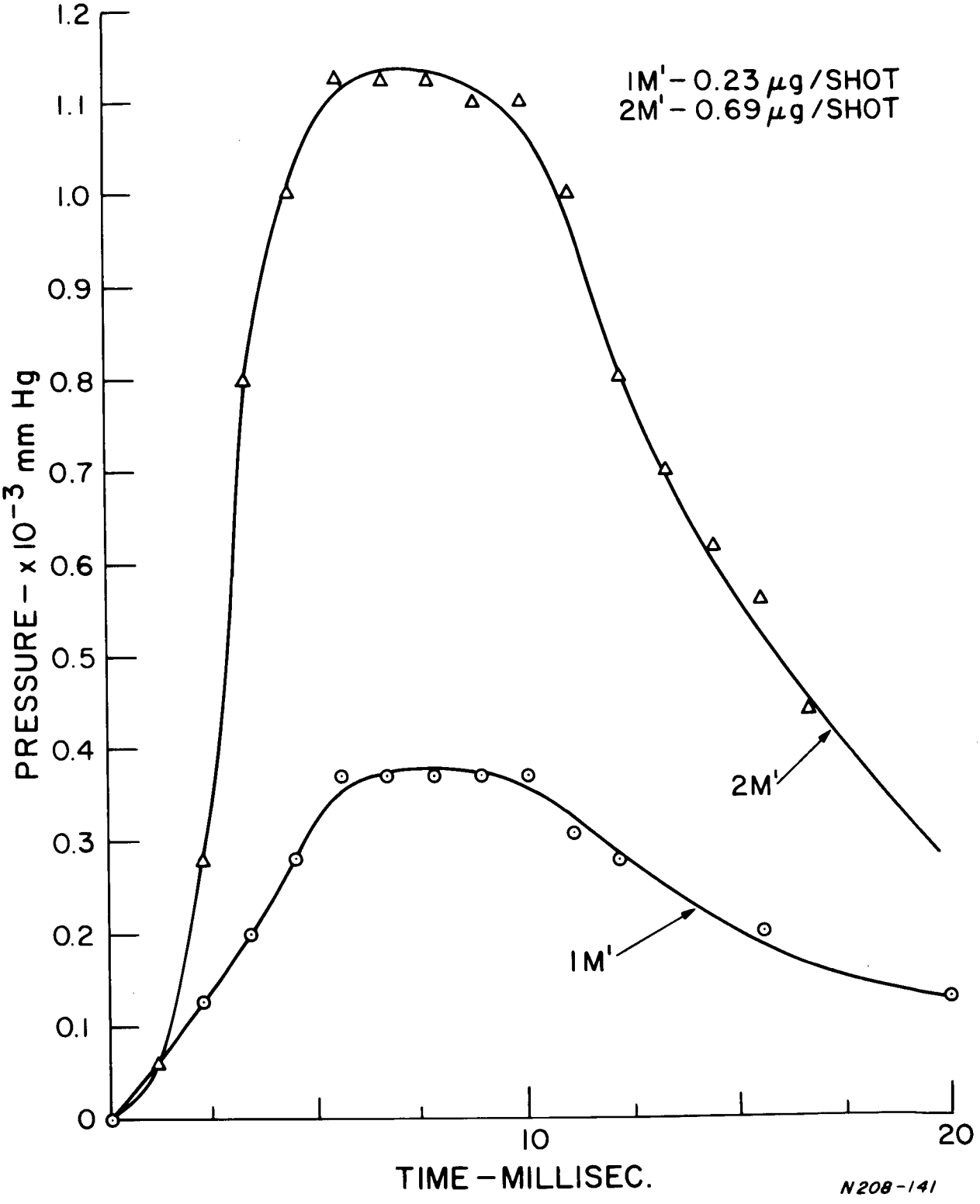

Figure 4.2.10 Pressure vs. Time Profile.

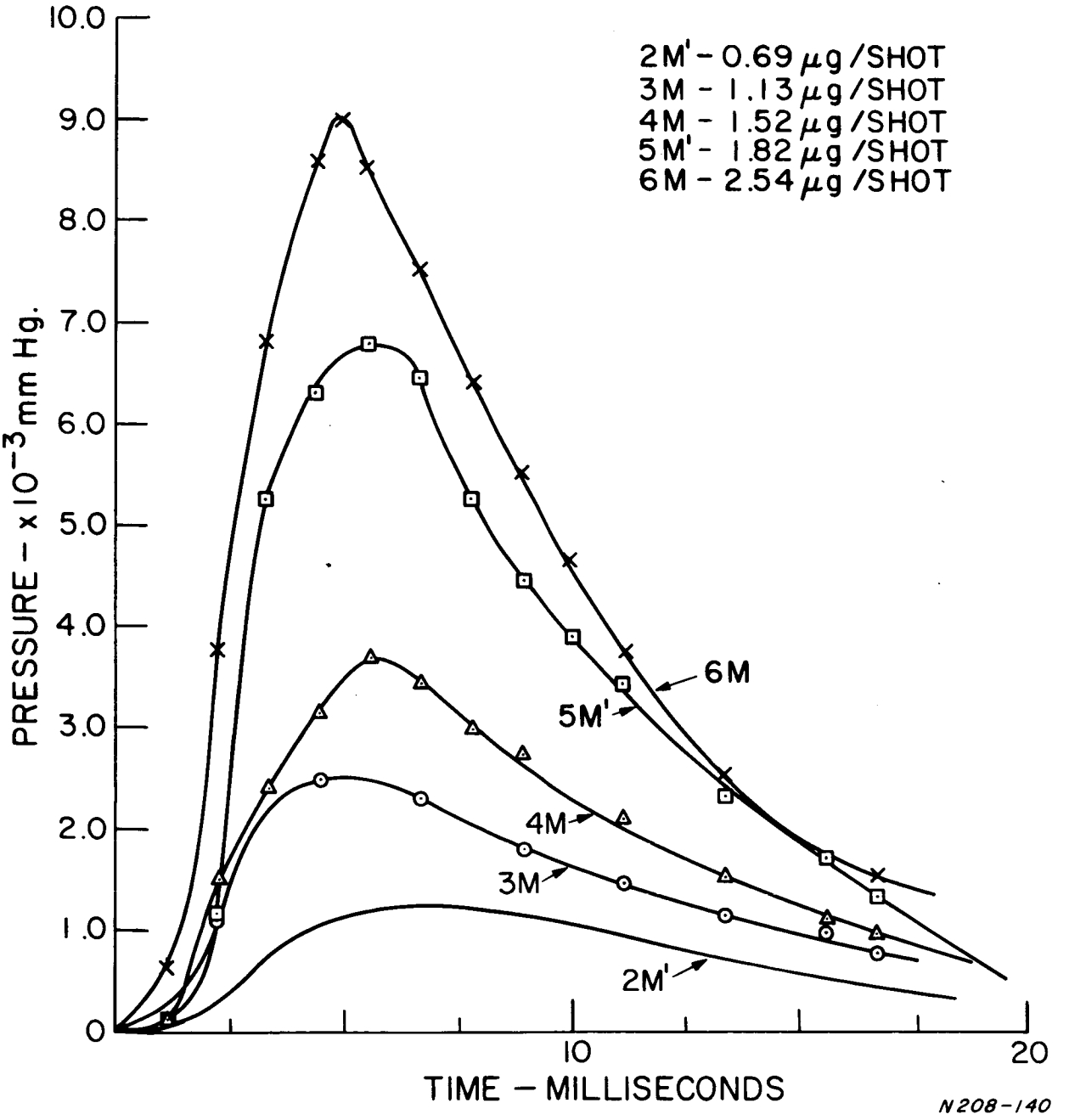

Figure 4.2.11 Pressure vs. Time Profile.

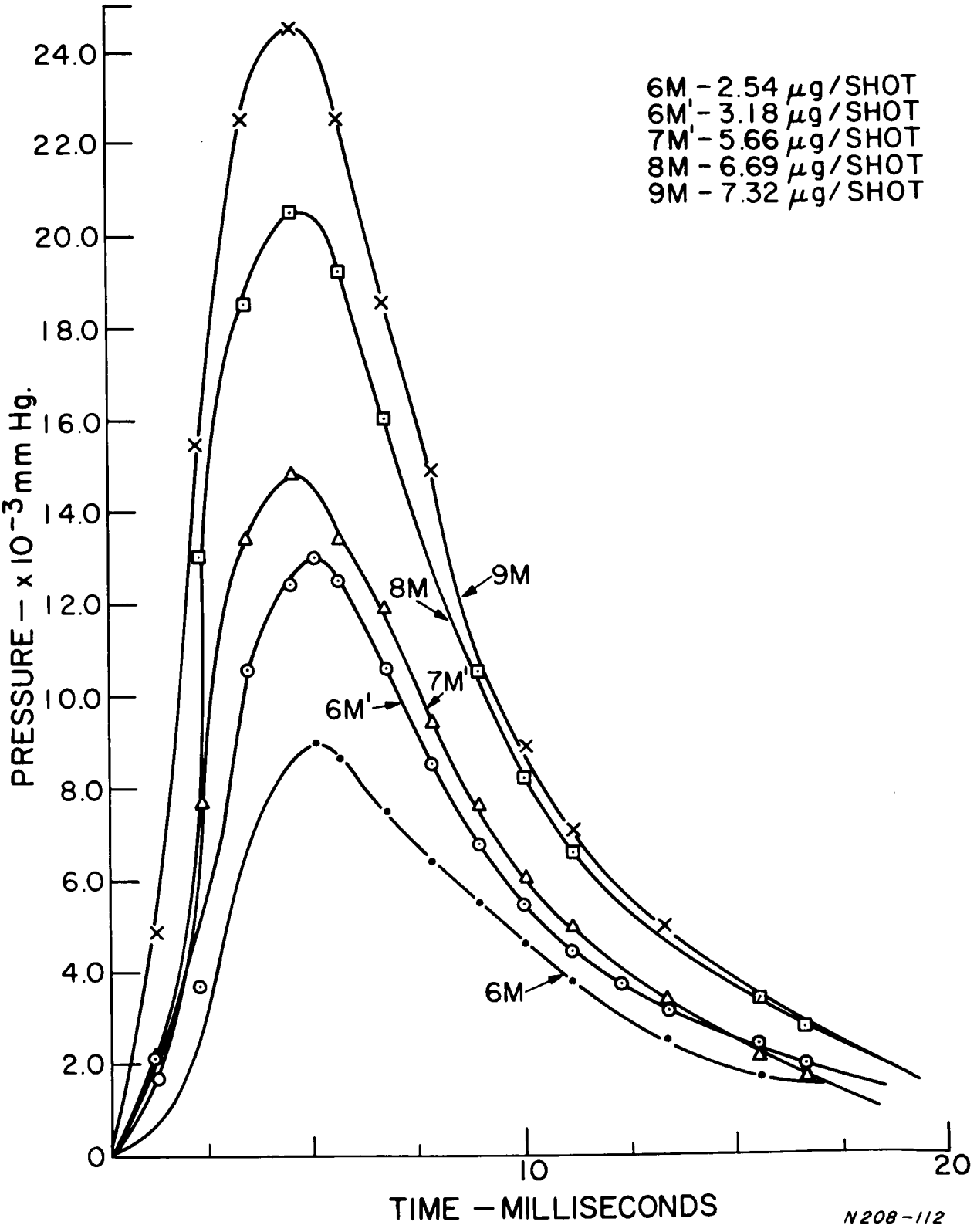

Figure 4.2.12 Pressure vs. Time Profile.

The integrals of the pressure-time curves shown in Figures 4.2.10 to 4.2.12 were taken by means of a planimeter. A value of $M_p/\int P\,dt$ was then computed for each integrated curve and the average value of K was used to determine the resulting mass flow rate (in micrograms per millisecond) vs. pressure (in mm Hg.) calibration curve shown in Figure 4.2.13. This data verified that the flow rates used in the Pulsed Program were comparable to those used in the C. W. Program.

4.2.3 Electron Energy Profiles

Extensive use of Langmuir probes provided data on the electron energies in the interaction region. After a study of recent experimental and theoretical work on the applicability of the probes in the high magnetic fields[6-8], and in flowing plasmas[9-11], it was concluded that the electron energy information contained in the retarding potential region of the I-V characteristics remained unaffected by the conditions that existed in the interaction region. The measured electron or ion saturation currents, however, would be of dubious value for obtaining electron or ion density information. Selected calculations and theory pertinent to this portion of the diagnostic experiments are included in Appendix C.

Due to the volume of data taken in this experiment, the results will be presented generally and in tabular form, with interpretations restricted to a close examination of a particular data run, for one set of experimental conditions. Only the engine region was explored and downstream measurements were not made.

The data sampling technique, as described previously, was used throughout this experiment. Both qualitative and quantitative data analyses were employed; that is, by means of a high-intensity background lamp the photographs of the CRO characteristic I-V traces were superimposed to offer an unambiguous display of energy (slope) changes in consecutive traces.

The electron energy vs. axial position were all of the same general form, exhibiting loss of longitudinal energy near resonance, and a thermalization to some new average level of energy beyond the resonance point. The transverse energy measurements exhibited the converse characteristics, generally rising to some level near the resonance and then dropping off again.

The particular case which will be described below corresponds to the following input parameters:

R-F Power Input:	3 KW, 1 millisecond pulses, 2 pulses per second

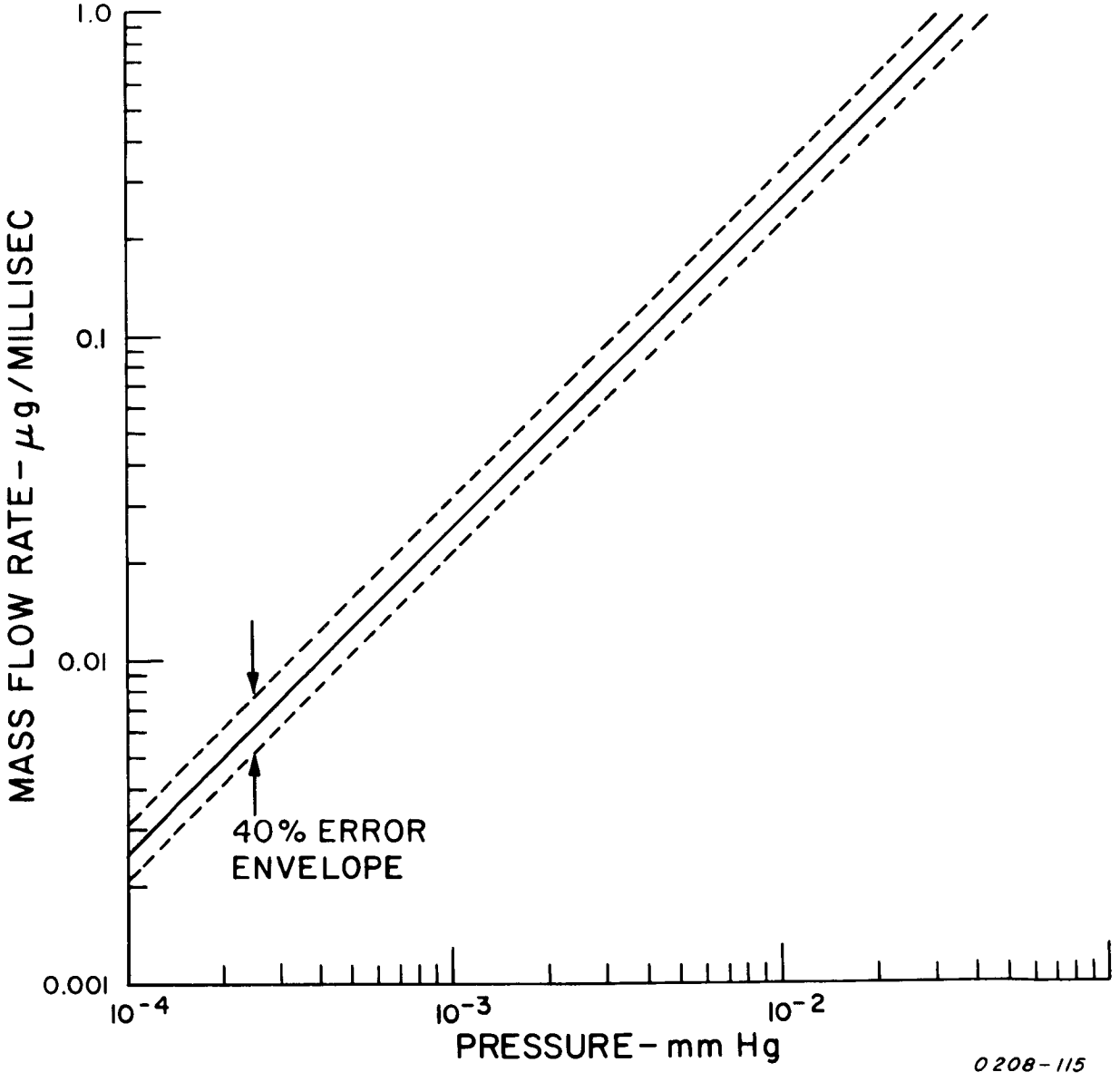

Figure 4.2.13 Mass Flow Rate (μg/millisec) vs. Pressure - mm Hg.

DC Coil Current:	450 Amps
Regulator Pressure to Pulsed Gas Valve:	7.5 lb.
Background Tank Pressure:	3×10^{-6} mm Hg
Approx. Flow Rate:	0.25 milligram sec.
Gas:	Argon

This set was chosen for presentation since these parameters closely correspond to r-f mapping experiment reported in Section 4.2.1. A summary of the results for these conditions is shown in Figure 4.2.14.

The $Te_{//}$ manifests a cooling effect near resonance. The energy transfer at this point is undoubtedly very complicated, however, one might suppose in a simplified model that the electrons undergo random thermal motion about the ions prior to resonance. At resonance, however, the electrons rapidly receive a large amount of energy thereby increasing their magnetic moment, $\vec{M}$. These resonant electrons are then expelled by the large $(\vec{M} \cdot \text{GRAD}) \vec{B}$ force. They may move only so far longitudinally, however, until the coulombic force attracting them to the slowly moving ions establishes an equilibrium in their longitudinal motion. This equilibrium corresponds to the establishment of the space charge. Then, the electrons begin to thermalize and reach a steady-state thermal equilibrium at z = 5.5 cm from the window. The calculation of the thermalization after resonance may be found in Appendix B.

The $Te_{\perp}$ showed an increase at the resonance point. Energy was going into this component of the electron motion, but it should be noted that the extreme temperatures that would be predicted based on the input power and propellant flow rate were not measured. Since the energy did not appear in either $Te_{\perp}$ or $Te_{//}$, it suggests that some dissipative mechanism was present, as for example excitation or higher states of ionization.

A plot of the electron and ion cyclotron radii vs. position is shown in Figure 4.2.14. At the resonance point, the ion cyclotron radius is only ten times the probe radius, thus, an ion saturation current measurement would not constitute a reliable ion density measurement. In addition, since the possibility of multiple ionization at resonance exists, then there could exist a discontinuity at resonance displacing the cyclotron radius downward by a factor of 1/Z (Z is the ionic charge) further increasing the uncertainty associated with inferring ion density values from ion saturation current measurements.

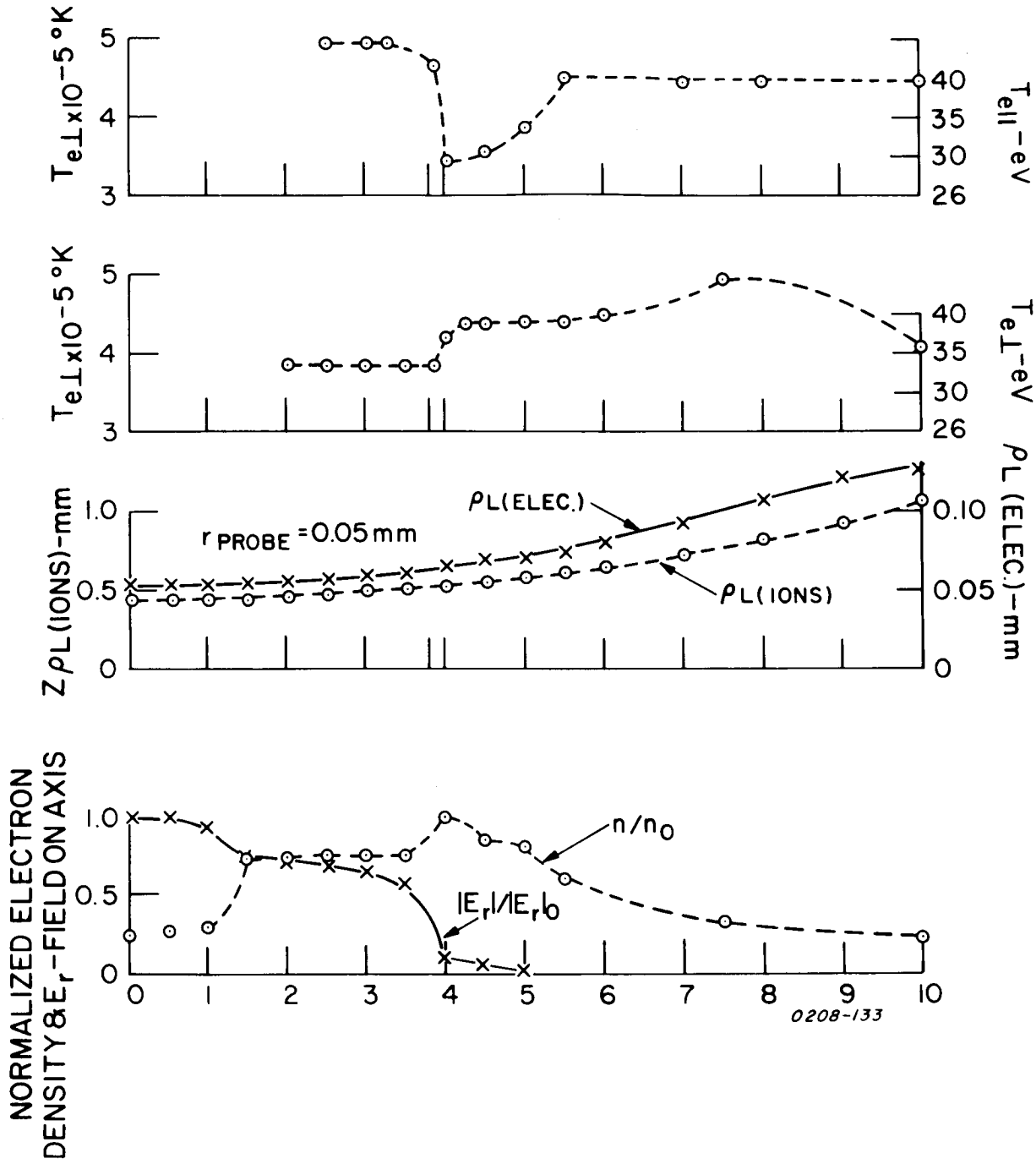

Figure 4.2.14 Summary Mapping of on Axis Langmuir Probe and R-F Results.

The normalized electron density plot shown in Figure 4.2.14 is obtained from the Langmuir probe measurements but should be used only as a qualitative measure since it indicates density values an order of magnitude lower than the r-f and mass flow determined values.

A typical Langmuir probe trace for this data set is shown in Figure 4.2.15. The upper and lower traces are the same curve but displayed at different gains; the upper to show the retarding potential region clearly, and the lower for determining the plasma potential. These regions are indicated on the ideal characteristic trace of Figure 4.2.16.

A summary of the results from all the Langmuir probe measurements for various coil currents is given in Table 4.2.1. A trend indicated by the table is that moving the resonance point up into the engine near the window (I_{coil} = 400 amps) seems to yield the lowest efficiency for energy transfer since R and $Te_{\perp}$ take on minimum values implying a high energy loss. Perhaps the boundaries became important under this condition. Another observable trend is that $Te_{\perp}$ increased monotonically with coil current and surpassed $Te_{//}$ between I_{coil} = 425 A and 450 A. This lead was maintained, indicating higher particle energy for ECR just outside of the engine rather than near the window.

The beam profile one centimeter or less beyond the resonance point was investigated in one data set which was taken using the transverse probe to map a transverse plane. It was seen there that the beam was still sharply confined, quite symmetrical, and throughout the major portion of the beam cross section $Te_{\perp}$ was found to be constant.

4.2.4 Ion Energy Analysis

The gridded stopping potential probe previously described was mounted near axis at the rear of the vacuum tank. Measurements of terminal ion energy were made by recording the current to the plate versus the applied positive repelling voltage on the second grid. The I-V trace was displayed on the scope as an X-Y plot. The derivative of this curve is proportional to the desired energy distribution function. An average ion energy and velocity were computed from the resulting ion energy distribution function. No charge or mass information was obtained from this probe.

The effect of charge exchange became clear in the course of this experiment. It was noticed that 30% higher terminal energies were recorded if the r-f pulse was synchronized to the leading edge of the gas pulse and if the pulse rate was reduced.

Good operating conditions were obtained by the synchronization seen

Scales: Vertical - 5 volts/cm Upper Trace
10 volts/cm Lower Trace

Horizontal - 29.6 volts/cm

Position: Z = 5.5 cm from the Window

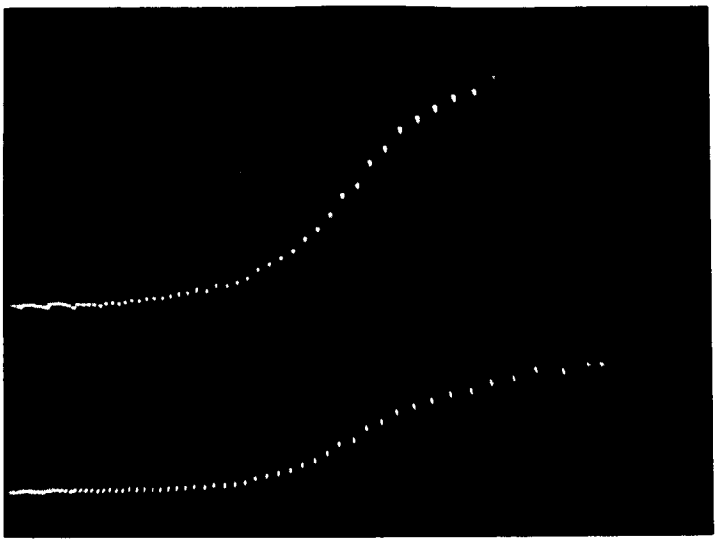

Figure 4.2.15 Langmuir Probe Trace for Data Set for $Te_{//}$.

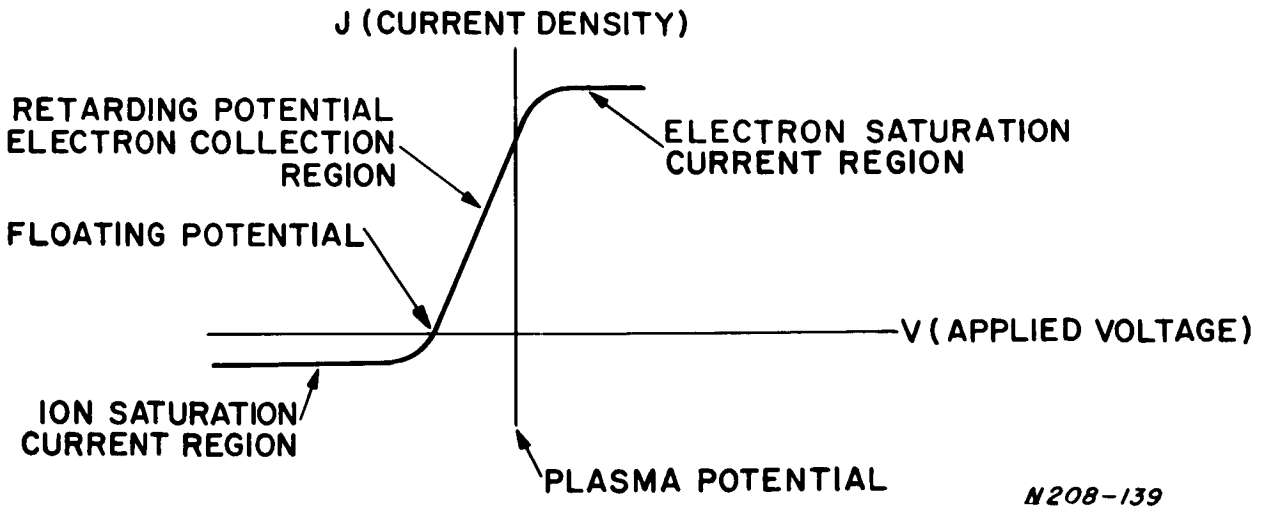

Figure 4.2.16 The Ideal Cylindrical Langmuir Probe Trace.

Table 4.2.1. Summary of Langmuir Probe Results

I_{coil} Amps	ECR Point (cm)	$Te_{\perp}$ @ ECR (ev)	$Te_{//}$ @ ECR (ev)	$Te_{//}$ Avg. (ev)	R
500	5.6	69.8	41.4	64.0	1.6
450	4.0	43.0	29.8	35.6	1.4
425	2.5	30.1	32.8	41.5	1.3
400	1.75	26.4	54.7	59.6	1.1

ECR = Electron Cyclotron Resonance

ECR Point = Location of ECR

R = Ratio of average $Te_{//}$ to $Te_{//}$ at ECR point

in Figure 4.2.17 with the system triggered once every two seconds. The upper trace is the gas trigger pulse (100 volts/cm), the lower trace is the r-f pulse (with coil off and, therefore, no plasma; 50 mv/cm), and the time scale is 5 milliseconds/cm. The relation of this synchronization to the occurrence of the gas pulse may be seen by referring to Figure 4.2.7. Here, the gas valve trigger pulse and gas pulse are presented; and it is easily seen that the synchronization shown in Figure 4.2.17 puts the leading edge of the r-f slightly prior to the gas pulse, so that the plasma ignited as soon as enough propellant built up in the engine. For comparison, Figure 4.2.18, which shows the synchronization used for all previous experiments, is presented. Here, the r-f occurs about 6 milliseconds into the gas pulse (at its peak). For front edge synchronization, the gas pulse had to be made greater in amplitude to get enough propellant in for ignition. And, the gas density varied much more in time during a given pulse than for the 6 millisecond synchronization. To further reduce background pressure, the pulse rate was slowed to one pulse every two seconds in order to more completely clear the vacuum tank between shots.

The results of the charge exchange experiment are shown in Figures 4.2.19 and 4.2.20 which show the I-V curves for front-end-synchronization and 6 millisecond synchronization respectively. These traces were made by use of the fast sweep circuit which for these data means 0 to +250 volts in 100 μsecs. In each case, five or more traces were superimposed to determine the average characteristic per plasma pulse. The base-lines were drawn with the r-f off, showing the line capacitance effects. In the latter case, there was a precursor of neutrals through which the ions were accelerated and experienced charge exchange. The net result was a decrease in terminal energy of 27% and a 12% decrease in the number of ions.

Once this effect had been determined, the running conditions were chosen to minimize charge exchange. An experiment was then performed to determine the change in terminal energy versus input power.

A computer program was written to reduce this data, i.e. take the derivative of the curves to generate the energy distribution function and perform the normalized moment integrals to obtain average energy and velocity. Tables 4.2.2 and 4.2.3 give the results for two data sets which used the sampling and fast sweep techniques respectively. The sweep range was 0 to 400 volts in a time of 60 μsec for the fast sweep technique. An important unknown here is the charge on the ion species. If the average ions were of charge Z, the average energies would be increased by a factor of Z and the average velocities by $Z^{1/2}$.

These results are plotted in Figure 4.2.21, where the relations $T \sim \overline{u}^{1/2}$ and $T \sim \overline{v}$ have been used, where T is thrust. The ordinate scales are relative. The linear relation between thrust and r-f power indicated by

Scale:

Upper trace	=	100 v/cm
Lower trace	=	50 mv/cm
Time	=	5 milliseconds/cm

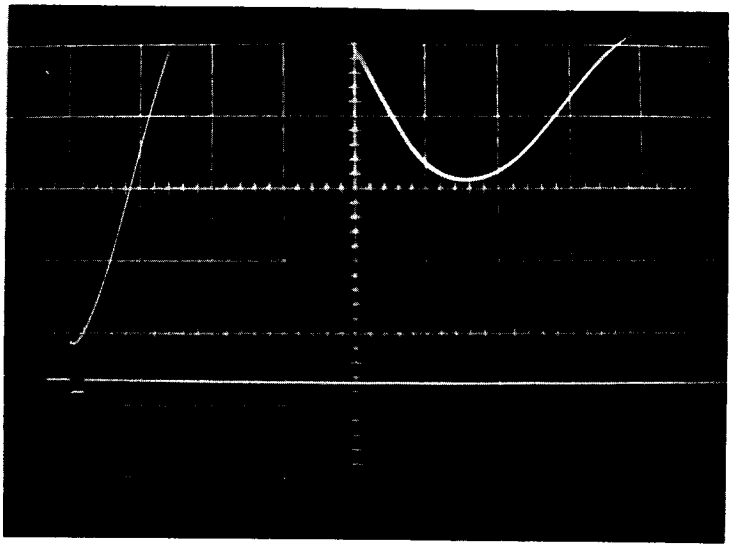

Figure 4.2.17 - Front Edge Synchronization, Scale Above

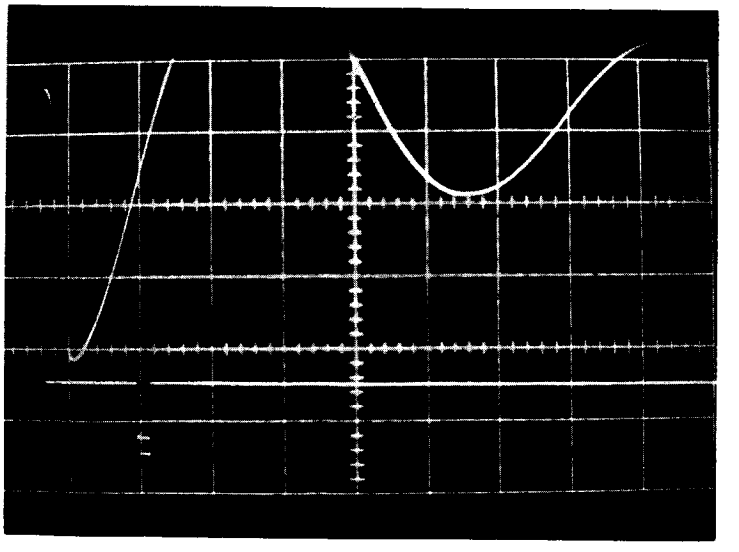

Figure 4.2.18 - 6-Millisecond Synchronization, Scale Above

Scale:

Vertical	=	40 mv km
Horizontal	=	17.2
r[illegible]	=	3 kw
I [illegible]	=	450 amps

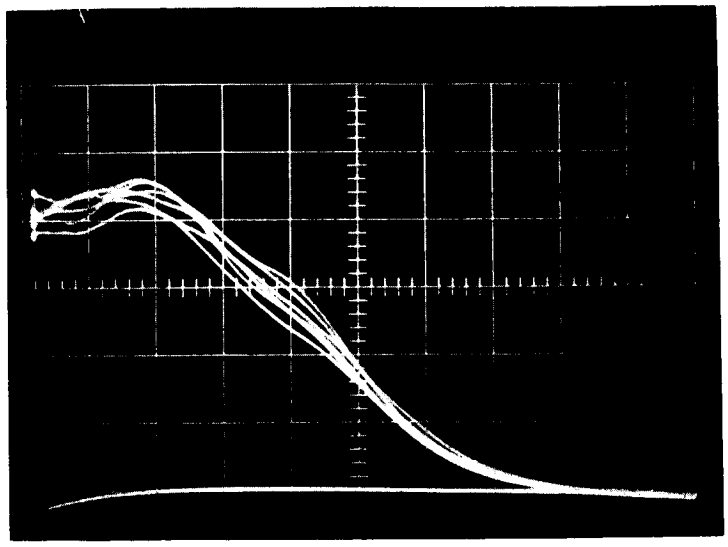

Figure 4.2.19 - I-V Trace for Front Edge Synchronization
Average Energy = 70.8 eV
Average Velocity = 1.8×10^4 m/sec.
Scale Above

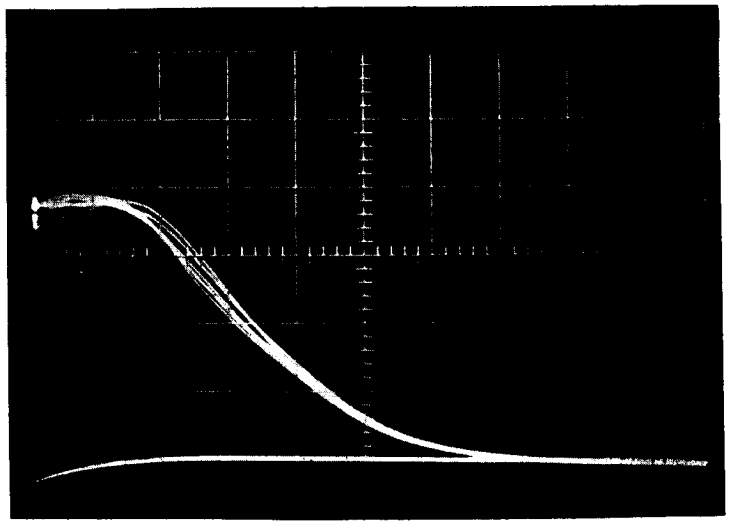

Figure 4.2.20 - I-V Trace for 6-Millisecond Synchronization
Average Energy = 51.8 eV
Average Velocity = 1.5×10^4 m/sec.
Scale Above

Table 4.2.2 - Terminal Ion Energy - Sampling Technique

I_{coil} (Amps)	r-f (kw)	$\bar{v}$ m/sec. x 10^{-4}	$\bar{u}$ e V
450	1.3	1.7	61.7
450	2.0	2.0	86.5
450	3.0	2.1	93.4
450	4.0	2.3	110.2

Table 4.2.3 - Terminal Ion Energy - Fast Sweep Technique

I_{coil} (Amps)	r-f (kw)	$\bar{u}$ e v
450	1.5	70.0
450	2.0	82.4
450	2.5	96.0
450	3.0	101.0
450	3.5	108.0
450	4.0	116.0
450	4.5	120.0

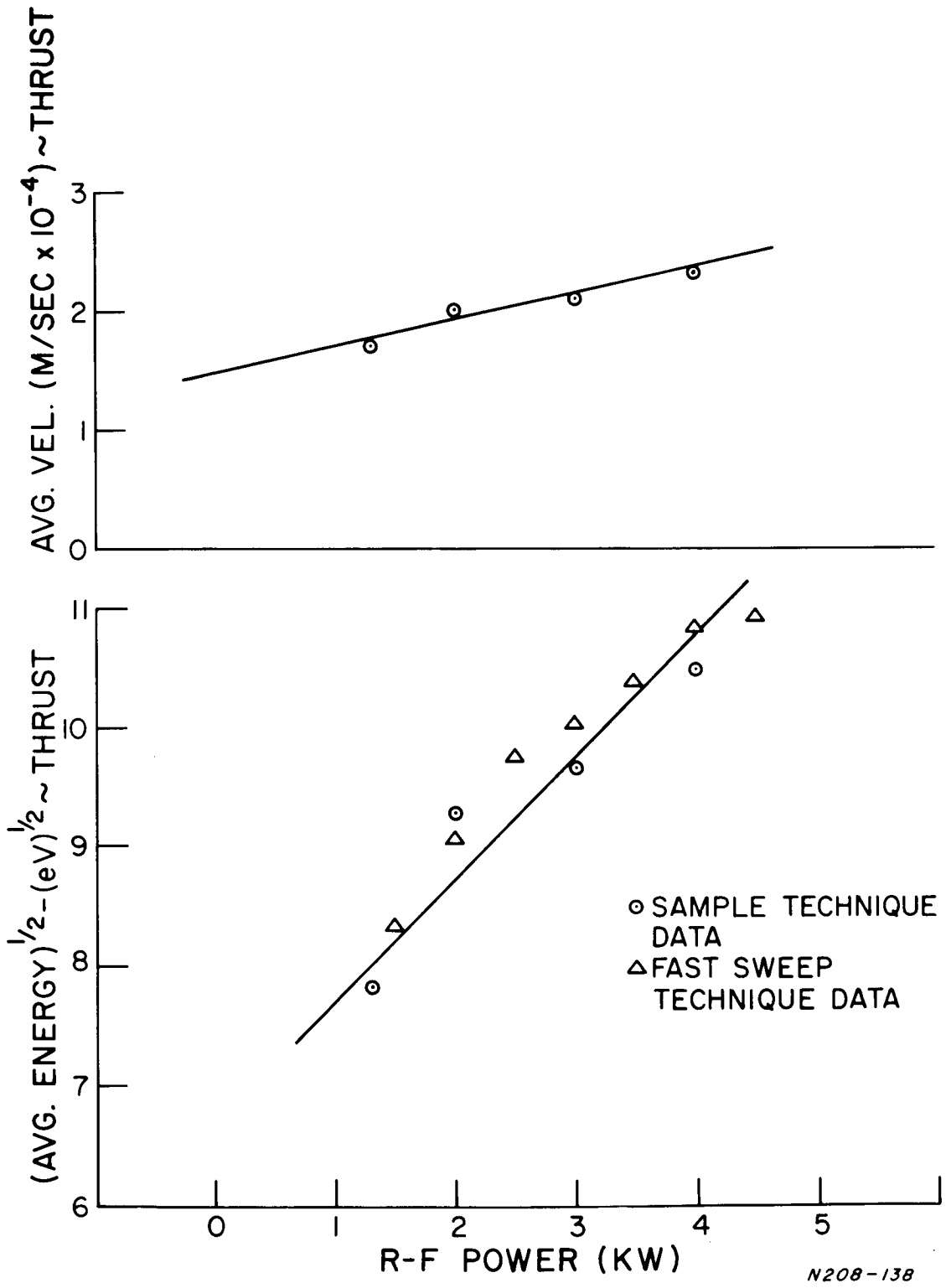

Figure 4.2.21 Thrust vs. input r-f power.

these plots is consistent with results of measured thrusts versus r-f power in the C. W. Program.

A data set for terminal energy versus coil current was taken for an r-f power of 3 kw. Interpretation was clouded by the effect of the dc coil on the mass flow due to gas-valve solenoid-coil interaction. Higher flow rates existed for higher coil currents but not more than a factor of two was involved from the lowest to the highest coil currents. At I coil = 350 A smooth I-V traces were observed. For I coil = 375 and 400 A, the results indicated instability of some kind and yielded the lowest terminal energies of the series (recall the Langmuir probe data for this condition - $T_{e//}$ at a minimum). At I coil = 425 A the traces were very stable with average energy increasing. The largest terminal energies were noted for I coil = 450 and 475 A, with a measurable decrease for I coil = 500. These data indicated that the best engine operation is obtained when the experimental resonance point (including the temperature effect) is located just outside of the engine.

4.2.5 Measurement of Diamagnetism at Resonance

The coil probe described in Section 3.2 was mounted such that it symmetrically ringed the engine at the engine exit plane. For coil currents of 450 Amps or more, the resonance occurred on axis from zero to 1 cm from the coil plane. It was shown in Appendix A that a diamagnetic effect of 0.1% of the dc coil field could be detected. However, because of incorrect sizing of the coil relative to the beam diameter (coil 8 inch diameter, beam about 1.5 in. diameter) the return flux associated with the diamagnetic field could return within the 8 inch diameter thus reducing the net flux through the coil. The results of this measurement are, therefore, inconclusive.

5. SUMMARY AND CONCLUSIONS

The performance of a microwave driven plasma accelerator has been investigated using a variety of inert gases and mercury. Thust and power transfer efficiency measurements were made using the inert gases while only thrust measurements were made with mercury. Over-all efficiencies ($T^2/2\dot{m}_o P$) where m_o is the input propellant feed rate, were found to be generally less than 10% (including the 65% polarizer efficiency) for all tests in which engine outgassing was not suspected. Because of the limited pumping speed of the vacuum system, entrainment occurred when Ar, Kr, or Xe were used as propellants. By making ion energy analyses, the actual accelerated mass due to entrainment was found to be as high as 10 times the input mass in some cases. The total efficiencies based on the actual accelerated mass would therefore be less than the value based on the input mass flow rate of the inert gases. For mercury, however, it is believed entrainment effects were not present since the background pressure was held to less than 1.5×10^{-6} mm Hg for all tests.

Power transfer efficiencies, determined for the inert gases yielded values up to 65% which is the maximum possible efficiency based on the performance of the circular polarizer. This suggested that 100% of the available power in the right hand component of the circular polarized microwave was transferred to the gas and was recovered by the calorimeter. Less than 15% of the power available in the right hand component resulted, however, in the development of thrust. It is hypothesized that the remaining 85% of the power was lost in excitation, ionization, heat transfer to the engine walls, and electron energy which cannot be transferred to the ions because of electron thermalization. Support of this hypothesis came from the results of the beam diagnostics performed in the Pulsed Program. It was found, using argon, that the transverse electron energy increased rapidly in the vicinity of resonance but maximum electron energies ranged only between 25 and 70 ev. This range of electron energy fell well below the anticipated value of about 1000 volts for the input power and mass flow rate utilized. Further, mappings of the longitudinal electron energy immediately beyond the resonance point indicated that the longitudinal electron energy rapidly increased with distance to approximately the value of the transverse electron energy at each point. This effect cannot be explained by invoking the adiabatic invariance of the magnetic moment since the longitudinal energy had not increased at the expense of the transverse energy. But rather this effect is explained by thermalization since the two energy components had become equal. As shown in Appendix B, thermalization by electron-electron impact is a highly probable process for the conditions that existed in this system. Because of thermalization about 1/3 of the energy given to the electrons is lost for propulsive purposes.

The low value of the transverse electron energy measured near resonance represents an upper limit to the energy which can be transferred

to the ion. For example if the transverse electron energy were measured to be 50 ev, then the maximum possible ion energy would be 50 ev which represents a velocity of 1.7×10^5 m/sec. The resulting thrust for 0.5 mg/sec feed rate of argon would be 8.5 mn and the stream power would be only 72 watts. If the input power were 1000 watt, the over-all efficiency would be 7.2%, a typical value of measured over-all efficiency. Assuming the ion to be doubly ionized would increase the over-all efficiency to 14.4%.

The low over-all efficiency is therefore traceable to the low values of the transverse electron energy occurring at the point of resonance and the mechanisms which limit the electron energy therefore limit the engine performance. It is hypothesized that ionization and excitation are the limiting mechanisms. For argon the maximum value of the cross section for single ionization occurs at 50 volts and the threshold for double ionization is 43 volts. Thus for measured average ion energies of 50 to 60 volts all the atoms are at least singly ionized. Now if one calculates the actual path length of an electron as its guiding center moves 0.5 cm (the distance over which the resonant absorption takes place) it is found that a 50 ev electron in cyclotron motion travels a distance of 50 meters. If the cross section for inelastic collisions with the singly charged ion is 10×10^{-16} cm^2 then the 50 meter path length represents 50 mean free paths.

Another plausability argument is to calculate the number of collisions per second that an ion receives. For an assumed collision cross section of 10×10^{-16} cm^2, an electron number density of 10^{13} electrons per cm^3, and an assumed total electron energy of 50 ev, the ion receives 4×10^6 impacts per sec. If an electron losses on the average 20 ev/collision then the loss rate is 80×10^6 ev/sec. In the time required for the guiding center to move 0.5 cm at 400 m/sec, the energy expense per ion becomes 1000 ev/ion. It is a loss of just this order of magnitude that is required to account for the low values of measured transverse electron energy and measured over-all efficiency based on thrust measurements.

In summary, the poor performance of the cyclotron resonance microwave plasma accelerator as determined by thrust measurements is supported by the results of beam diagnostic studies. Because the electrons appear to be limited in the amount of kinetic energy that can be given to them, due to inelastic collisions resulting in both radiation and multiple ionization, the ions are also limited in the amount of energy that they can acquire. The limiting electron energy and, thus, limiting ion energy, appears to be associated with the threshold energy for second ionization in the vicinity of 1 KW to 3 KW power input and mass flow rates for argon of 0.3 to 0.5 mg/sec.

If the above conclusions are indeed correct it appears that the logical course to pursue is to investigate the use of propellants having high second ionization potentials at low input power. The light alkali metals appear to

be most suitable for this application because of their relatively few levels for excitation and their high second ionization potential. For example using sodium, by limiting the input power to less than 200 watt for a mass flow rate of 1 mg/sec, the maximum electron energy would be expected to be less than that of the second ionization potential thus avoiding multiple ionization losses. If electron thermalization were present then possibly an over-all efficiency of about 27% would be achieved at a maximum specific impulse of approximately 1660 sec. If higher specific impulses are required then lithium would provide approximately 3600 sec. at 33% over-all efficiency for a power input under 700 watt at 1 mg/sec feed rate.

These performance predictions using the alkali metals interestingly compare directly with reported MPD arc performance characteristics. Using sodium[19] over-all efficiencies between 30 and 40% are reported at I_{sp} values between 1600 and 2000 sec with the over-all efficiency leveling off about 2000 sec specific impulse. This leveling off is interpreted in terms of our model as the result of increased inelastic losses, excitation and ionization of the sodium ion, associated with the increased electron energy necessary to achieve higher specific impulse.

MPD arc performance using argon is also reported in Ref. 19. Over-all efficiencies less than 11 per cent for I_{sp} values between 1000 and 4000 sec are reported. This performance is essentially identical with that of cyclops using argon.

Other reported MPD arc performance characteristics[20] using lithium further compare directly with the prediction of our model. The reported results of Ref. 20 are somewhat uncertain because of uncertainties associated with the lithium feed system, however, over-all efficiencies between 15 and 55 per cent for I_{sp} values between 2000 and 5500 sec are reported. Our model in comparison predicts 33 per cent over-all efficiency at 3600 sec specific impulse.

The proposed model based on the results of thrust measurements, power transfer measurements, and beam diagnostics which yielded electron and ion energy measurements explains the ion acceleration process in terms of an energy exchange between the electrons and ions. The electrons receive energy directly from the applied electric fields and then transfer their energy to the ion. The electron to ion energy transfer mechanism is via the charge separation induced electric field resulting from the $(\vec{\mu} \cdot \text{grad})\ B$ force acting on the electrons which are gyrating due to the presence of the magnetic field. (In the MPD arc the energy transfer process is probably a combination of $(\vec{\mu} \cdot \text{grad})\ \vec{B}$ and collision processes). The maximum ion energy is related to the maximum kinetic energy that an electron can have in the presence of the ion with the maximum electron kinetic energy determined by the onset of second ionization and/or inelastic processes leading to radiation. For heavy

atoms with relatively low values of second ionization potential and many levels of possible excitation through inelastic collision, the losses encountered when attempting to maintain the electron at relatively high values of kinetic energy (50 to 100 ev for argon) are such as to yield over-all efficiencies of less than 10 per cent. On the other hand, for smaller less complex atoms having relatively high second ionization potentials, the losses are less and higher over-all efficiencies are anticipated. This description curiously appears to apply to MPD arcs as well as to Cyclops and, thus, suggests that similar loss mechanisms and possibly similar acceleration mechanisms occur in both devices.

Recommended future work should be in two areas. First, the measurement of the radiation characteristics, both in intensity and wave length, occurring when using argon propellant should be accomplished. Second, measurements of the thruster performance using sodium should be made.

6. REFERENCES

1. D. B. Miller, et al, "Investigation of Plasma Accelerator," Final Report of Contract NAS 3-6266, NASA CR-54746, November, 1965.

2. F. F. Chen, Plasma Diagnostics and Techniques, edited by R. H. Huddlestone and S. L. Leonard, Academic Press, New York, 1965, p. 184.

3. B. Gorowitz, et al, "Performance Study of a Repetitively Pulsed Two Stage Plasma Propulsion Engine," Final Report of Contract NAS 3-2502, November 20, 1963.

4. E. A. Valsamakis, "Hot Cathode Fast Miniature Ionization Gauge," Grumman Research Department, Memorandum R. M. -268, February 1965; also, T. Karras, B. Gorowitz and P. Gloersen, "Neutral Mass Density Measurements in a Repetitively Pulsed Coaxial Plasma Accelerator," AIAA J., 4, 1366, (1966).

5. B. Gorowitz, et al, "Study of Parametric Performance of a Two-Stage Repetitively Pulsed Plasma Engine," Final Report of Contract NAS w-1044, NASA CR-54846, March 1966.

6. M. A. Heald and C. B. Wharton, Plasma Diagnostics with Microwaves, John Wiley and Sons, Inc., New York, 1965, p. 8, 76, 108, 113, 383.

7. T. Dote and H. Amemiya, "Negative Characteristic of a Cylindrical Probe," Journal of the Physical Society of Japan, Oct. 1964, Vol. 19, No. 10, pp. 1915-24 (see pc-3 for a critique of this work).

8. T. Dote, H. Amemiya, and T. Ochimiya, "Effect of a Magnetic Field Upon the Saturation Electron Current of an Electrostatic Probe," Japanese Journal of Applied Physics, Dec. 1964, Vol. 3, No. 12, pp. 789-796.

9. J. B. French, "Langmuir Probes in a Flowing Low Density Plasma," Institute of Aerophysics, University of Toronto, UTIA Report No. 79, Aug. 1961.

10. B. B. Meckel, "Analysis and Application of Langmuir Probe Characteristics in a Moving Plasma," Sci. Rept. No. 2, AFCRL Contract No. AF 19(604)-554, II-165, December 1959.

11. B. B. Meckel, "Experimental Study of the Interaction of a Moving Body with a Plasma," Rarefied Gas Dynamics, L. Talbot (ed.), Academic Press, 1961, pp. 701-714.

12. L. Spitzer, Jr., Physics of Fully Ionized Gases, Interscience Publishers, New York, 1962, p. 133, 149.

13. T. H. Stix, The Theory of Plasma Waves, McGraw-Hill, New York, 1962.

14. G. L. Ragan, Microwave Transmission Circuits, McGraw-Hill Book Co., Inc., New York, 1948, p. 369.

15. S. Ramo, J. R. Whinnery, and T. Von Duzer, Fields and Waves in Communication Electronics, John Wiley and Sons, Inc., 1965.

16. S. C. Brown, Basic Data of Plasma Physics, M. I. T. Press and John Wiley and Sons, Inc., 1959, Chap. 5. (For simplicity in the computation of Appendix B, air data was used. This gives the absoluted upper bound to the required breakdown fields for argon since (1) air requires larger field strengths for breakdown then argon and (2) the magnetic field increases the effective electric field strength in the engine for this diffusion-controlled breakdown.)

17. E. W. McDaniel, Collision Phenomena in Ionized Gases, John Wiley and Sons, Inc., New York, 1964, Chap. 13.

18. S. C. Lin, "On The Limiting Velocity for a Rotating Plasma," AVCO Research Report 101, for AF Contract AF 19(604)-7458, April 1961.

19. G. L. Cann, et al, "Hall Current Accelerator," NASA CR-54705 Final Report of Contract NAS 3-5909, Feb. 4, 1966.

20. G. L. Cann, et al., "High Specific Impulse Arc Jet Thrustor Technology," Technical Documentary Report No. ASD-TR-64, Contract No. AF 33(615)-1579, December 1964.

21. R. Gajewski and J. L. Hirshfield, "Influence of Coulomb Interactions on the Cyclotron Radiation of Electrons Moving on a Single Orbit," The Physics of Fluids, Vol. 4, No. 6, June 1961, pp. 736-739. (Note: this formula had to be corrected to the form of E-2.)

APPENDIX A

DETECTION OF THE DIAMAGNETIC EFFECT

A. C. Eckert and G. F. Crimi

Consider an electrostatically shielded coil of N turns encircling the plasma stream. The net flux through the coil is the flux due to the field coil minus that due to the diamagnetic property of the plasma. If the net flux through the coil changes in time due to the build up or decay of the plasma then an emf will be induced in the coil, the magnitude of which is given by the Faraday equation:

$$\text{emf} = - N\frac{\Delta\Phi}{\Delta t}$$

where $\Delta\Phi$ is the net change of flux which occurred in the interval Δt. Now if the change in flux is due to the build up in number and energy of gyrating electrons and there are n electrons per unit volume, then the magnetization per unit volume is

$$M = n\mu,$$

where μ is the final magnetic moment of each gyrating electron. The induced magnetic field B is therefore;

$$B' = \mu_o M.$$

If A is the beam cross section then the induced flux is

$$\Delta\Phi = AB'.$$

Relating the magnetic moment to the electron transverse energy and the steady state magnetic field B, the induced emf becomes

$$\text{emf} = - \frac{\mu_o NA}{B}\left(\frac{nE}{\Delta t}\right)$$

where n electrons per unit volume are pumped up to energy E in the time Δt.

For $n = 10^{19}\ m^{-3}$, $E = 50$ ev, $\Delta t = 10\ \mu$sec , $B = 0.3$ web/m^2, $N = 7$, and $A = 7 \times 10^{-4}\ m^2$,

$$\left|\text{emf}\right| = 0.14 \text{ volts},$$

an easily measurable quantity. The value of Δt was arrived at as a typical plasma relaxation time based on electrostatic probe current vs. time data. The rise time of the probe current from zero to some constant average value upon the initiation of the plasma was found to be approximately 10 to 20 μsec. This leading edge of the plasma pulse was then assumed to be representative of the energy transfer time. The probe response time was found to be at least an order of magnitude less.

The expected voltage trace is shown in Figure A-1.

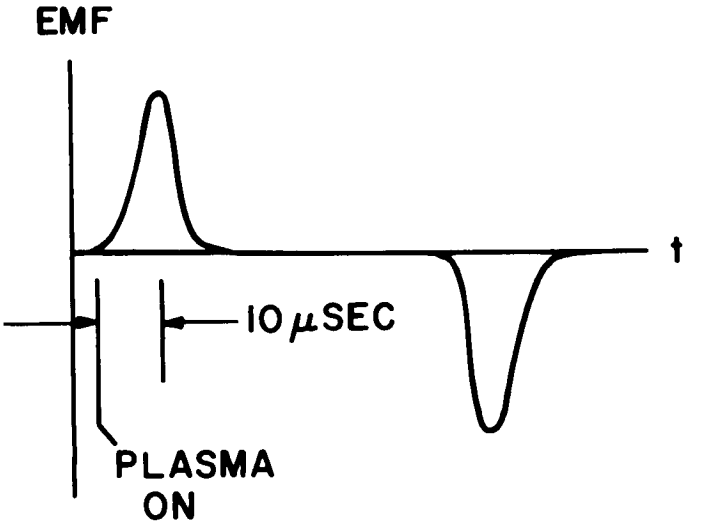

Figure A-1.

APPENDIX B

R-F WAVE PROPAGATION IN CYCLOPS

G. F. Crimi

Several simplifications may be applied to the propagation of the r-f wave in the cyclops engine. The wave propagates in the TE_{11} mode in a guide of dimensions chosen to suppress any higher order transverse modes. Once the plasma is developed, however, the change in the dielectric constant of the medium would certainly allow other modes to exist. In view of the total absorption and reflection properties of the plasma, however, specific additional modes may be neglected with only the gross electric field properties being considered. Furthermore, since the transverse electric field component of the wave is the dominant force field combining with the axially directed dc coil field to produce the electron cyclotron resonance, we may neglect both the cylindrical geometry and the boundary effects and assume a plane wave. This assumption is corroborated by the fact that in the engine, the magnitude of the dc coil field is large enough to allow consideration of most of the plasma enclosed by the guide and still remain several cyclotron radii from the boundaries (see Figure 4.2.14). Thus, boundary conditions may be generally neglected in the wave-plasma interactions and in the particle motions, and need only be included as a net energy loss term due to wall heating.

Existing theories for waves in plasmas contain the assumption of thermal equilibrium and experimental evidence that thermal equilibrium in fact did exist for the plasmas generated here is found in the linear ln I versus V portion of the obtained Langmuir characteristic traces. The particular small region of electron cyclotron resonance is probably the exception to this assumption.

From the plot of the field strength vs. axial distance from the window (Figure 4.2.14) there is an indication of thermalization over a distance of 1.5 cm after the resonance point. The possibility of thermalization is supported by the following calculation:

From Spitzer[12], the self-collision time for electrons is

$$t_{e-e} = \frac{.266\, T^{3/2}}{n_e \ln \Lambda}$$

where $\Lambda = \frac{3}{2ZZ_f e^3} \left(\frac{k^3 T^3}{\pi n_e} \right)^{1/2}$

For this calculation (in e. s. u.), given

$$e = 4.8 \times 10^{-10} \quad \text{e. s. u.}$$

$$k = 1.38 \times 10^{-16} \quad \frac{\text{erg}}{\text{Deg. Kelvin}}$$

Assume, $Z \approx Z_f = 1$ (Z and Z_f are the charge of the "test particle" and the "field or target particle," respectively.)

$$T_e \approx 4 \times 10^5 \, ^oK$$

$$n_e \approx 10^{12} \, cm^{-3}$$

then $\ln \Lambda \approx 15$ and

$$t_{e-e} = 4.44 \times 10^{-6} \text{ sec.}$$

Now the electrons spiral in transverse orbits with high velocity but move longitudinally only as fast as the ions, say 400 m/sec. Therefore a distance of 1. 5 cm takes about T = 37 microseconds allowing

$$\text{No. of collisions} = \nu_{e-e} T = \frac{1}{t_{e-e}} T$$

$$= 8.$$

Therefore, thermalization is easily attained in this distance.

We may conclude from the above that existing theories for plane waves in Maxwellian magneto-plasmas are applicable in the analysis of wave propagation in the Cyclops engine. An especially lucid first order treatment of this problem is given by Wharton[6]. He expands the effective dielectric tensor which appears in Stix[13], derived from the first-order Vlasov equations, assuming a Maxwellian zero order particle distribution. The main point to be brought out here is that in the resultant dispersion relation the temperature dependence of the wave propagation becomes clear. The resulting index of refraction for 1st order temperature effects is

$$\mu^2_{\ell,\, r} \approx \left\{ 1 - \frac{\left(\frac{\omega_p}{\omega}\right)^2}{1 \pm \frac{\omega_b}{\omega} - j\frac{\nu}{\omega}} \right\} \Bigg/ \left\{ 1 + \frac{\left(\frac{\omega_p}{\omega}\right)^2}{\left(1 \pm \frac{\omega_b}{\omega} - j\frac{\nu}{\omega}\right)^3} \frac{kT}{mc^2} \right\}$$

where $\omega_p^2 = \frac{n_e e^2}{\epsilon_o m_e}$

$$\omega_b = \frac{eB}{m_e}$$

$$\nu = \langle \nu_{ei} \rangle \approx 5 \times 10^5 \text{ sec}^{-1} \text{ (Ref. 6)}$$

$$\omega = 8.35 \text{ GHZ.}$$

The upper sign refers to the left-handed (ordinary) circularly polarized wave; the lower to the right-handed (extraordinary) wave. As a simplification, we will neglect the small collision term, and then note that the plasma temperature has the effect of producing the resonance phenomena at either a lower frequency or, correspondingly, at higher field strength. At resonance, $\mu_r^2 \rightarrow \infty$, therefore,

$$\omega_b = \omega \left\{ 1 + \left[\left(\frac{\omega_p}{\omega} \right)^2 \frac{kT}{mc^2} \right]^{1/3} \right\}$$

or $$B_{res}' = B_{res} + \Delta B_{res} \qquad \text{Web/m}^2.$$

For a sample calculation, given

$$mc^2 = 0.55 \times 10^6 \text{ ev}$$

$$e = 1.6 \times 10^{-19} \text{ coul}$$

$$\omega = 5.2 \times 10^{10} \text{ rad/sec}$$

then, $$B_{res}' = 0.2970 + 2.65 \times 10^{-10} [\omega_p^2 \, kT \text{ (ev)}]^{1/3}$$

Assume typically

$$n_e = 10^{12} \text{ cm}^{-3}$$

$$\omega_p = 8 \times 10^{10} \text{ rad/sec}$$

$$kT = 40 \text{ ev}$$

$$B_{res}' = 0.2970 + 0.0165 \quad \text{Web/m}^2$$

$$= 3135 \text{ Gauss.}$$

For a dc coil current of 450 A, the above temperature correction shifts the resonance point toward the window by 0.5 to 0.6 cm. This was the exact experimental result noted in the r-f field mapping section of this report.

Wharton points out that the finite temperature effect dominates over any collision effects if

$$\frac{\omega}{\omega_b - \omega} \frac{[kT(ev)]^4}{n[cm^{-3}]} > 10^{-13}$$

For the Cyclops engine, this implies the temperature effect dominates whenever $8.1 \times 10^6 > \omega_b/\omega$ which is always the case.

The resonance shift is explained quite well by the theories which ascribe the damping mechanism of the wave energy to a phase mixing or phase trapping of wave energy by particles synchronous with the wave due to their doppler-shifted frequency. The high temperature here allows the doppler shift to be measurable, and the Landau damping arguments are consistent with the large absorption obtained in the relatively small resonance region.

The circular polarizer plot may be used to determine the degree of polarization achieved. It may be shown[14] that the ratio of powers in the plane and circular components of the polarizer output may be expressed as

$$\frac{P_p}{P_c} = \frac{1 - \sin 2(\cot^{-1} r)}{\sin^2 2(\cot^{-1} r)}$$

where $r = \dfrac{\text{maximum field}}{\text{minimum field}}$

For the pulsed experiment, $r = 8.8/1.6 = 5.5$; this then gives $P_p/P_c = 5.23$. Now, the plane power component may be evenly divided into right-hand and left-hand circular components. Therefore, the ratio of total right-hand component to total power input is

$$\frac{P_{rt}}{P_T} = \frac{0.5 + P_c/P_p}{1 + P_c/P_p} = 58\%.$$

The result marks this commercial circular polarizer as rather ineffective.

Furthermore, one may calculate the free-space E-field strength in

terms of the input power. Given the components of a transverse electric field $TE_{n\ell}$ in cylindrical coordinates

$$H_z = A J_n(k_c r) \cos n\varphi$$

$$E_r = j\frac{n\eta f}{k_c r f_e} A J_n(k_c r) \sin n\varphi$$

where $k_c = P'_{n\ell}/A$

$P'_{n\ell} = \ell$th root of $J'_n(x) = 0$

A = radians of waveguide

f_c = waveguide cutoff frequency

$\eta = \sqrt{\mu/\epsilon} \approx 377$ ohms for free-space

the amplitudes may then be calculated. Using the Poynting vector and the two dimensional divergence theorem the total power may be written as[15]

$$W_T = \frac{\eta^2 (f/f_c)^2}{2 Z_{TE}} \int_{c.s.} H_z^2 ds$$

$$= \frac{\eta}{2}\left(\frac{f}{f_c}\right)^2 \sqrt{1 - \left(\frac{f_c}{f}\right)^2} \int_0^{2\pi} \int_0^a A^2 J_n^2(k_c r) \cos^2(n\varphi)\, r\, dr\, d\varphi$$

where

$$Z_{TE} = \eta \left[1 - \left(\frac{f_c}{f}\right)^2 \right]^{-1/2}$$

Given, the input power, this expression may be solved for the amplitude

$$A = \left\{ \frac{W_T}{0.0125} \right\}^{1/2} \text{ amps/m.}$$

For 3000 watts, A = 489 amps/m. The radial electric field strength, which is

$$\left| E_r \right| = \frac{n\eta f}{k_c r f_c} A J_n(k_c r) \sin n\varphi,$$

becomes in this case, on axis,

$$|E_r| = 1.3 \times 10^5 \text{ volts/m.}$$

This calculation is presented to illustrate that the magnitude of the field strength exceeds that required for breakdown. Very roughly, this is[16]

$$|E_B| = 3 \times 10^3 P \left[1 + \left(\frac{\omega}{\nu}\right)^2\right]^{1/2} \text{ volts/m,}$$

where, again roughly,

$$\nu = 5.3 \times 10^9 P$$

$P \equiv$ pressure in torr.

In front of the engine, $P \approx 10^{-2}$ torr. Therefore,

$$\nu = 5.3 \times 10^7$$

and $$|E_B| = 3 \times 10^4 \text{ volts/m.}$$

So, a large amount of ionization may occur before the resonance point. With this in mind, we may again examine the experimental r-f mapping. It is seen that near one centimeter from the window, a large portion of the electric field vanishes. The power remaining at z = 1.5 cm is found from Figure 4.2.14 to be

$$\frac{P_{rt}}{P_T} = \left(\frac{.75}{1.0}\right)^2 = 56\%.$$

We have then concluded that all of the left-hand wave has been reflected and the portion of right-hand wave, not dissipated in ionization continues to propagate. This corresponds well to the percentage of right-hand component power available. Furthermore, it is seen from the dispersion relation that the plasma temperature, to this order of approximation, does not influence the reflection, so that for the collisionless case, reflection occurs for $\mu^2_\ell \to 0$, or

$$\left(\frac{\omega_p}{\omega}\right)^2 = 1 + \frac{\omega_b}{\omega} .$$

At z = 1 cm, $\omega_b/\omega = 1.25$ and $(\omega_p/\omega)^2 = n/nc$

where $n \equiv$ local electron density

and $n_c \equiv$ critical density, where $\omega = \omega_p$.

Now, $$n_c = \frac{f_p^2}{(8.98 \times 10^3)^2} = \left(\frac{8.35}{8.98}\right)^2 \times 10^{12}$$

$$= 8.6 \times 10^{11} \text{ cm}^{-3}$$

Therefore, reflection of the left-hand wave occurs where

$$n = 2.25\, n_c$$

$$= 1.93 \times 10^{12} \text{ cm}^{-3}.$$

Under the conditions for the r-f mapping experiment, the average particle density would be

$$n = \frac{\dot{m}}{VAM}$$

$$\approx 2 \times 10^{13} \text{ cm}^{-3}.$$

where $\dot{m}$ = mass flow rate
V = velocity
A = area
M = mass per particle

Therefore, this gives an experimental determination of the minimum density at z = 1.0 cm from the window. At least 10% of the total gas is already ionized at this point. One might then use this to determine the absolute density profile from the relative densities provided by the Langmuir probe experiments. (The plasma conditions disallowed an absolute measure of density by the Langmuir probe. As verification, density values computed from this data were consistently an order of magnitude lower than values obtained by other methods.)

Another point of interest is the penetration depth for a reflecting wave. Including the magnetic field, the penetration depth is given approximately by,

$$\delta = \frac{c}{\omega_p} \left(1 + \frac{\omega_b}{\omega}\right)^{1/2} \left\{1 - \left[1 + \left(\frac{\omega_b}{\omega}\right)\right]\left(\frac{\omega}{\omega_p}\right)^2\right\}^{-1/2}$$

Using the parameters from above, this gives $\delta = 0.46$ cm. This penetration depth corresponds well to that measured (0.5 cm) in the r-f mapping experiment.

APPENDIX C

LANGMUIR PROBE IN A MAGNETIC FIELD

G. F. Crimi

No attempt will be made here to present a complete theory of the use of an electrostatic probe in a magnetic field. For a recent treatment of this subject, and also for probe theory in flowing plasmas, the reader is referred to References 5 thru 11.

The analysis presented here is from a treatment of cylindrical probe theory in a magnetic field[7]. Consider a probe aligned parallel to the magnetic field. From the equations of motion for a particle in an electrostatic probe sheath it has been shown, that for a particle having positive radial velocity at $r = r_p$ to reach the probe, then

$$u^2 - (q^2 - 1)(v - \frac{1}{2}\omega r_f)^2 \geq - \frac{2eV_p}{m} - \frac{1}{4}\omega^2 r_p^2 (q^2 - 1)$$

where u, v, w = initial velocity components of an electron at the sheath edge in local Cartesian space
r_p = probe radius
r_f = sheath radius
$q = r_f / r_p$
$\omega = e B/m$, cyclotron frequency
m = electronic mass
e = electronic charge
V_p = potential difference between the probe and the plasma.

From this result it is seen that in the retarding electron collection region, where there is essentially no sheath ($q \approx 1$), the effect of the magnetic field disappears and the inequality simply requires particle energies greater than the applied (negative with respect to the plasma) probe potentials. Therefore, the electron and ion saturation currents may well be affected by the magnetic field, but if the retarding field region is clearly visible in the characteristic I-V trace, then the electron temperature may be computed. The solution of the probe current density in the retarding electron collection region is

$$J = J_o \exp\left(\frac{eV_p}{kTe}\right)$$

having assumed a Maxwellian velocity distribution function,

$$f(u, v, w) = \left(\frac{m}{2\pi kTe}\right)^{3/2} \exp\left[-\frac{m}{2kTe}\left(u^2 + v^2 + w^2\right)\right],$$

for the electrons, where

k = Boltzmann constant
and Te = Electron Temperature.

It is easily seen then that in this region, a plot of ln J versus V_p will be a straight line whose slope is inversely related to the electron energy. The experimental results show this linear relation, implying thermal equilibrium in the Cyclops plasma.

Examination of the cyclotron radii for the plasma species shows that at no time are they much greater than the probe radius. As mentioned in the text, multiple ionic charge may further decrease the ionic gyroradius. Also, the exact probe areas may not be precisely known, due to spot-welding, insulating paints, and wearing when heated for cleaning. Therefore, it is quite safe to assume that the ion saturation current measured is smaller than that which would be measured in no magnetic field, with more certain probe dimensions. This then precludes the possibility of particle density measurements from the saturation current portions of the characteristic I-V trace. Indeed, based on the experimental data, particle densities were computed to be an order of magnitude below those predicted from mass flow and r-f mapping data. These results are in direct contradiction to the conclusions reached in Reference 7. The results there, however, would imply that no effect is noted in the ion saturation region for field strengths up to $3.3\ A^{1/2}$ kilogauss where A is the atomic weight in grams. The computation is in error, however, and the result should read $33\ A^{1/2}$ kilogauss. Using this criteria in our case implies that the critical field strength is 700 kilogauss which is unreasonable. Thus, no plausible criterion has yet been established to concisely determine the usefulness of the electrostatic probes in the measurement of plasma density in large magnetic fields.

APPENDIX D

ION ENERGY ANALYSIS

G. F. Crimi

Some of the interesting results which evolved from the ion energy experiment will be presented in this appendix.

The four-gridded probe was introduced in this experiment with the hope that the first grid (see Figure 3.2.10) could be biased so that secondary electrons due to ion bombardment emitted from the collecting plate could be repelled back to the plate and, therefore, would not be interpreted as an increase in ion current. The real situation turned out to be much more complex. It was noted instead that for large positive potentials on screen 2 a negative (electron) current was measured at the plate. This current became larger when either screen three was biased highly negative (say -500 v instead of the -200 v indicated) or if screen one was biased more than several volts negative. The condition of a false ion current was certainly being masked by this other unexpected phenomenon.

The effect of the presence of a plasma generated from neutrals inside the probe was first examined. The pertinent results based on the maximum probe current measured, the probe dimensions, etc., were as follows:

Particle density (within probe)	$= 10^{11}$ cm^{-3}
Pressure (within probe)	$= 2 \times 10^{-5}$ mm Hg
Ionization rate (within probe)	$= 10^{6}$ sec^{-1}
Plasma residence time (between 2 grids)	= 0.5 microseconds
Current due to plasma in the probe	$= 10^{-14}$ amps

Thus, the intra-probe plasma could not account for the observed phenomenon.

Further examination revealed secondary emission from the screens could account for the observed effects. Screens 1 and 4 were 200 mesh at 78% transmissivity; screens 2 and 3 were 500 mesh at only 50% transmissivity. With high positive potentials on screen 2, the high energy ions were repelled, bombarding screen 3, causing secondary electrons. The electrons were then rapidly accelerated through screen 2 toward the plate. It was found for copper that the peak number of electrons produced per incident electron is 1.3 and occurs at an incident energy of 600 ev[17]. Only one secondary for one incident electron occurs for bombarding electrons of 200 ev. The third screen was therefore fixed at -200 volts, high enough to keep out the plasma, but such that the secondary emission ratio at the plate was known. Then if

too high a negative potential were applied to screen one, all of the secondaries at the plate would be repelled causing a net electron current to the plate. Now the energy of the secondaries at the plate would be approximately 4 ev and thus the number of escaping secondaries from the plate could be then regulated by applying a small negative bias (-1 1/2 to -4 volts) to the first grid, depending upon the plasma conditions, so that the influx of high energy secondaries to the plate just cancelled the efflux of low energy secondaries from the plate. This resulted in zero electron current measured at the plate for high positive potentials on screen two, which was the desired effect.

High energy ion bombardment of the plate would also produce secondaries. Data for tungsten (which is apparently very close to copper with regard to secondary emission properties) indicate the number of electrons per incident ion is fairly insensitive to incident ion energy[17]. For incident ions of various charges the following percentages occur:

Electrons Per Ion	Charge on Argon Ion
0.1	+1
0.4	+2
1.1	+3

The emitted secondaries have a peak energy in the range of 3 ev. Therefore, by proper regulation of the bias on the first grid, we were able to simultaneously control the spurrious currents caused by both types of secondary emission. For most cases, with -200 volts on screen three, acceptable operation of the probe was obtained with -2 volts on screen one.

As mentioned in the text, a computer program was employed to reduce the ion energy data. First, the energy distribution function f(u) was computed by a numerical differentiation of data points taken from the I-V trace. A numerical integration was then used to find the average energy.

$$\bar{u} = \frac{\int u\, f(u)\, du}{\int f(u)\, du}$$

and the average velocity,

$$\bar{v} = \frac{\sqrt{2e/M_+} \int u^{1/2} f(u)\, du}{\int f(u)\, du}$$

where it is seen that singly charged ions are assumed. For ions of charge Z, the average energy would be increased by a factor of Z and the average velocity by $Z^{1/2}$.

APPENDIX E

RADIATION

G. F. Crimi

In an effort to determine the energy loss mechanism of the Cyclops plasma, several types of particle radiation were considered. This study was severely limited, however, because little work has been done with multiply ionized particles. The results presented in this Appendix, were based on data available for argon, the propellant used exclusively in the pulsed experiment.

When the electron encounters a heavy ion, light quantum may be emitted. If the electron remains free, with its energy decreased, the transition is called free-free and the radiation is called bremsstruhlung. For a Maxwellian distribution of electron velocities, the total amount of power per unit volume radiated in this manner is [12]

$$P_b = \left(\frac{2\pi k T_e}{3m_e}\right)^{1/2} \frac{2^5 \pi e^6}{3hm_e c^3} Z^2 n_e n_i \qquad \text{(E-1)}$$

$$= 1.42 \times 10^{-27} Z^3 n_i^2 T_e^{1/2} \quad \frac{\text{ergs}}{\text{cm}^3 \text{ sec}}$$

for $n_e = Z n_i$.

Assume: $T_e = 4.5 \times 10^5 \ ^oK$

$n_i = 10^{13} \text{ cm}^{-3}$

then, $P_b = 10^{-5} Z^3 \text{ watts/cm}^3$

assuming a beam diameter slightly greater than the engine diameter, then

$$P_b = 10^{-4} Z^3 \text{ watts/cm.}$$

This then represents a very small radiation contribution.

Electrons in cyclotron motion radiatiate. This radiation is given by [21]

$$P_c = 6 \times 10^{-22} n_e B^2 E \text{ watts} \qquad \text{(E-2)}$$

where B is in gauss, and E is in MeV. Near resonance Te = $4.5 \times 10^5 \ ^oK$, B = 3000 gauss, E = 40 ev, and ne = $Z \times 10^{13} \text{ cm}^{-3}$; then,

$$P_c = 2.16 \times 10^{-6} Z \text{ watts/cm}^3$$

or, assuming the area used above,

$$P_c = 2.16 \times 10^{-5} \; Z \text{ watts/cm},$$

which is smaller than the Bremsstruhlung result.

A recent study of all of the radiation mechanisms in a high temperature plasma was done by Lin[19]. The total radiated power is given as the sum of the free-free, free-bound, and bound-bound or line radiation,

$$P_r = P_{ff} + P_{fb} + P_{r\ell},$$

which is developed to the form

$$P_r = P^* \theta_e^{1/2} \epsilon^{-1/\theta_e} q_i(\theta_e) \{\alpha^2 G_f(\theta_e) + \alpha(1 - \alpha) \eta_{r\ell} G_{r\ell}(\theta_e)\} \qquad \text{(E-3)}$$

where

$$P^* \alpha^2 = V n_e^2 \pi a_o^2 \left(\frac{8 W_1}{\pi m_e} \right)^{1/2} W_1$$

$W_1 \equiv$ 1st ionization energy for argon,
$= 2.4 \times 10^{-11}$ ergs

$a_o = 5.29 \times 10^{-9}$ cm

$n_e = 10^{13}$ cm^{-3}

$m_e = 9.1 \times 10^{-28}$ gm

$V \equiv$ volume of radiator

$\alpha \equiv$ percent of ionization

giving $P^* \alpha^2 = 5.5 \times 10^7 \; V$

The first term in (E-3) gives the sum of the free-bound and free-free radiation. In this expression,

$\theta_e \equiv$ normalized electron temperature
$= kT_e / W_1 = 2.4$

$q_i(\theta_e) \equiv$ normalized integrated electron-impact ionization cross section
$= 5.46$

$G_f(\theta_e) \equiv$ normalized radiative heat loss term
$= 2 \times 10^{-5}$

Using these values in the first term of (E-3) gives

$$\frac{P_{ff} + P_{fb}}{V} = 6.2 \times 10^{-4} \text{ watts/cm}^3.$$

Using the results of E-1, for singly ionized argon,

$$P_{fb} \approx 6.1 \times 10^{-3} \text{ watts/cm.}$$

for the free-bound radiation contribution. The line radiation is given from the second term of E-3, where

$\eta_{r\ell}$ = escape factor

= 1

$G_{r\ell}(\theta_e) \equiv$ normalized radiative heat loss term due to resonance line radiation

= 0.8

In terms of the percentage of ionization for the first level, the line radiation is

$$P_{r\ell} = 246 \frac{(1 - \alpha)}{\alpha} \text{ watts/cm.}$$

Should the species be completely singly ionized this contribution is zero, but the contributions from the ionized particles must then be summed. Unfortunately, this data is not available at this time. It is seen from the above, however, that the resonant line radiation is a major loss mechanism. Apparently, this mechanism plus that of losses in higher ionizations severely limits the usefulness of certain elements as propellants.